Mémoire

Auteur : De Clerck, Victor
Promoteur(s) : Tychon, Bernard
Faculté : Faculté des Sciences
Diplôme : Master en sciences géographiques, orientation global change, à finalité approfondie
Année académique : 2023-2024
URI/URL : http://hdl.handle.net/2268.2/22192

Faculty of Sciences
Geography department

Modeling the precipitation-runoff relationship based on observations and HEC-HMS simulations:

A case study in the Nyarutovu subbasin of the Mukungwa watershed, NW Rwanda

Master thesis presented by: **Victor DE CLERCK**

for obtaining the title of

Master in geographic sciences, global change orientation, geomorphology and natural hazards finality

Academic year: **2023-2024**
Defense date: **September 5-6, 2024**

Jury president: Pr. **Xavier FETTWEIS**
Promotor: Pr. **Bernard TYCHON**
Reading juries: Pr. **Aurélia HUBERT**
Pr. **Geoffrey HOUBRECHTS**
Ir. **Déogratias NAHAYO**

Acknowledgments

I would first like to thank my promotor, Bernard Tychon, for his confidence, his involvement, his time, and his precious advice. I would also like to thank Déogratias Nahayo who gave up his time for me, especially when I was in Rwanda and who was my main contact person.

I would like to thank Thomas Dethinne (PhD student at ULg) who kindly agreed to help me create a script for the QGIS Python console to automate certain tasks. I would also like to thank Jean Van Campenhout and Geoffrey Houbrechts for their invaluable help in establishing the rating curve and calculating water levels. Finally, I would like to thank Christophe Dessers, PhD student at ULg, for his invaluable help and advice on hydrologic modeling.

Many thanks also to INES-Ruhengeri and all its staff for welcoming me to Musanze, and for putting everything in place for my field mission to run smoothly. Special thanks to Noel, David, and Valens. I am also grateful to all the students I have met and shared good times with.

I would also like to thank Elisabeth, Josiane, Coco, Jean Pierre, Eric, and all the staff from Isange Paradise Resort, where I stayed for two months, for their warm welcome. My warmest thanks go to my two friends Frank and Alain, with whom I had such a great time.

Finally, I would like to thank my mother, my father, my partner, and my friends for their unwavering support during these five years of study.

The trip undertaken as part of this master thesis was made possible thanks to the financial support of the “Académie de recherche et d'enseignement supérieur de la Fédération Wallonie-Bruxelles”, Belgium, as part of its development cooperation policy. Many thanks to them and the community in general for giving students such opportunities.

Summary

Floods are one of the most significant natural hazards. Flood events are common in Rwanda, particularly in the northwest region where the Nyarutovu watershed, the focus of this study, is located. This region frequently experiences flash floods, as was the case in May 2023 when over 130 people lost their lives. There is an urgent need for the development of flash flood forecasting techniques, given the increasing risk of such events.

The objective of this study was to model the dynamics influencing the relationship between precipitation and runoff in the Nyarutovu watershed.

To achieve this, rigorous cleaning and preparation of precipitation and discharge data were performed, resulting in a time series from January 1, 2023, to May 3, 2023. Thirteen hydrologic events were selected for modeling, involving the separation of baseflow and differentiation between individual events. Then, the hydrologic modeling software HEC-HMS was employed, employing various methods to simulate the runoff in the watershed.

The results obtained from the hydrologic modeling, both before and after calibration, were fairly poor and do not allow for any flood forecasting for the Nyarutovu watershed.

The main reason for these poor outcomes was attributed to uncertainties in the data, which probably significantly affected the accuracy of the modeling more than the chosen methods. Particularly, precipitation data, critical for hydrologic modeling, seem to lack accuracy due to its spatial variability across the watershed and uncertainties associated with interpolation from punctual observations. Additionally, the discharge data were approximate and prone to errors, which also propagated in the hydrologic modeling process.

Looking forward, it would be interesting to explore whether remote sensing precipitation data such as satellite or microwaves links from cellular communication networks observations could be used to monitor flash floods in the studied area.

Résumé

Les inondations représentent l'un des risques naturels les plus importants. Elles sont fréquentes au Rwanda, et en particulier au nord-ouest, où se situe le bassin versant de Nyarutovu, sujet de cette étude. Cette région est souvent affectée par des crues éclair, comme celle survenue en mai 2023 qui a entraîné la mort de plus de 130 personnes. Il est crucial de développer des techniques de prévision des crues éclair, lesquelles sont amenées à se multiplier.

L'objectif de cette étude était d'analyser et de modéliser les interactions entre les précipitations et le ruissellement dans le bassin versant de Nyarutovu. Pour cela, des données de précipitations et de débits ont été, le plus rigoureusement possible, nettoyées et préparées résultant en une série temporelle de précipitation et de débit allant du 1 janvier 2023 au 3 mai 2023. Treize événements ont été sélectionnés pour la modélisation hydrologique, impliquant la séparation du débit de base et la distinction entre les événements individuels. Le logiciel de modélisation hydrologique HEC-HMS a été utilisé, employant différentes méthodes pour simuler le ruissellement dans le bassin versant.

Les résultats obtenus de la modélisation hydrologique, tant avant qu'après la calibration sont insatisfaisants et ne permettent aucune prédiction des crues pour le bassin versant de Nyarutovu.

Ces mauvais résultats sont principalement dus aux incertitudes entourant les données, lesquelles ont probablement eu un impact plus significatif sur la précision de la modélisation que les méthodes sélectionnées. En particulier, les données de précipitations, cruciales pour la modélisation hydrologique, semblent ne pas être assez précises en raison de leur variabilité spatiale dans le bassin versant et des incertitudes liées à l'interpolation à partir d'observations ponctuelles. De plus, les données de débits étaient également entachées d'erreurs se propageant lors de la modélisation hydrologique

À l'avenir, il serait intéressant d'examiner si les données de précipitations obtenues par télédétection, telles que les données satellitaires ou les observations faites via liaisons micro-ondes des réseaux de communication cellulaires pourraient être utilisées pour le suivi des crues éclaires dans la zone d'étude.

Table of contents

1. Introduction

1.1. Context of the study

This master thesis is part of a broader project titled "Landslide and Flood Hazards and Vulnerability in NW Rwanda: towards applicable land management and disaster risk reduction (LAFHAZAV)," funded by ARES. The goal of this project is to study the effects of Land Use and Land cover (LULC) changes on the magnitude and frequency of landslides and floods. Within this framework, I collaborated with Déogratias NAHAYO, a Rwandan partner from INES Ruhengeri (The Institute of Applied Science of Musanze), who is pursuing his doctoral thesis as part of the aforementioned project. A two-month field trip to NW Rwanda was conducted to gain a deeper understanding of the ground reality, measurement methods, and the situation of people affected by these natural hazards. The primary objective of this work, therefore, is to contribute to the goals of the project, particularly aiding the doctoral research of Déogratias. It is not intended to provide definitive conclusions and solutions to the problem of flooding in the study area but rather to serve as a valuable resource for the project.

1.2. Flooding

Floods are one of the most major natural hazards. It is described as the inundation of land that is normally dry (Seneviratne *et al*., 2021). Floods have a range of complex impacts which can be: (1) social: loss of life, health issues, psychological trauma, disruption of activities such as education and sports, and harm to cultural institutions. (2) economic: direct and indirect financial losses, damage to homes and farms, damage to important assets, disruption of public services, and expenses for insurance coverage. (3) environmental: pollution of flooded areas, changes in water quality, sedimentation in reservoirs, impacts on biodiversity, and increased risk of landslides (Beilicci & Beilicci, 2015).

Flooding disasters accounted for 44% of the disaster events that occurred between 2000 and 2019 with 1.65 billion people affected and 104,614 deaths (CRED & UNDRR, 2020). According to the last IPCC report, the current global warming of the Earth is leading to an increase in the magnitude of floods. Furthermore, flooding events are projected to become more frequent in most parts of the world, including Asia, sub-Saharan Africa, western Europe, Central and South America, and eastern North America (Caretta *et al*., 2023).

The main causes and affecting factors of floods are the quantity and intensity of precipitation, the characteristics of the watershed that drive the capacity of precipitation to infiltrate into the ground — mainly the LULC and the slope — the morphology of the river and the watershed and potential engineering structures designed to store water (Beilicci & Beilicci, 2015; Seneviratne *et al*., 2021).

There are several types of floods; we will focus on river floods and flash floods. These two types of floods are due to runoff, which is generated according to the following equation:

$$R = P - (E + I + \Delta R)$$

Where R represents the runoff, P is the precipitation, E is the actual evapotranspiration (including interception), I is the infiltration into the soil or in the aquifers and ΔR represents the changes in storages (i.e. accumulation in surface depressions) (Seneviratne *et al*., 2021).

River floods occur when water levels rise above river banks due to excessive rainfall over a prolonged period, resulting in soil water saturation. River flooding can extend far beyond the areas experiencing rainfall (USGS, s.d.).

On the contrary, flash floods are characterized by a rapid rise in water levels on small spatial scales. They typically occur in subtropical, tropical, and subequatorial zones, and their frequency and intensity are increasing in regions where they were previously uncommon. Their sudden onset is attributed to locally intense precipitation that exceeds the infiltration rate of the soil, which is influenced by the LULC, leading to significant runoff. Relief also plays a role, especially in mountainous regions where flash floods are exacerbated by the rapid concentration of runoff in river channels (Kusina & Golosov, 2020; USGS, s.d.).

According to Kuksina & Golosov (2020), flash floods in small catchments are particularly destructive due to the rapid formation of flood waves. They illustrate this with an example: a basin of 0.65 km² may experience a 40-minute lag time[1], while a basin of 165 km² could have a lag time of up to 5 hours. Other significant factors contributing to flash floods magnitude include antecedent moisture conditions (AMC) (Kuksina & Golosov, 2020) and anthropogenic

[1] The lag time is the time interval between the center of mass of the excess precipitation and the peak discharge (Fang *et al*., 2005; USDA, 2010). This concept will be discussed below.

factors such as massive deforestation, unsustainable exploitation of sloping lands and LULC changes (Beilicci & Beilicci, 2015).

Generally, flash floods result in a higher loss of life due to the limited time available for warning individuals about the imminent danger (Jonkman, 2005). Urgent attention is needed for the development of flash flood forecasting techniques, as the risk of flash floods continues to increase. However, forecasting flash floods remains a challenging task due to the complex nature of precipitation forecasting, given the limited spatial and temporal scales of flash flood events (Kuksina & Golosov, 2020).

2. Description of the study area

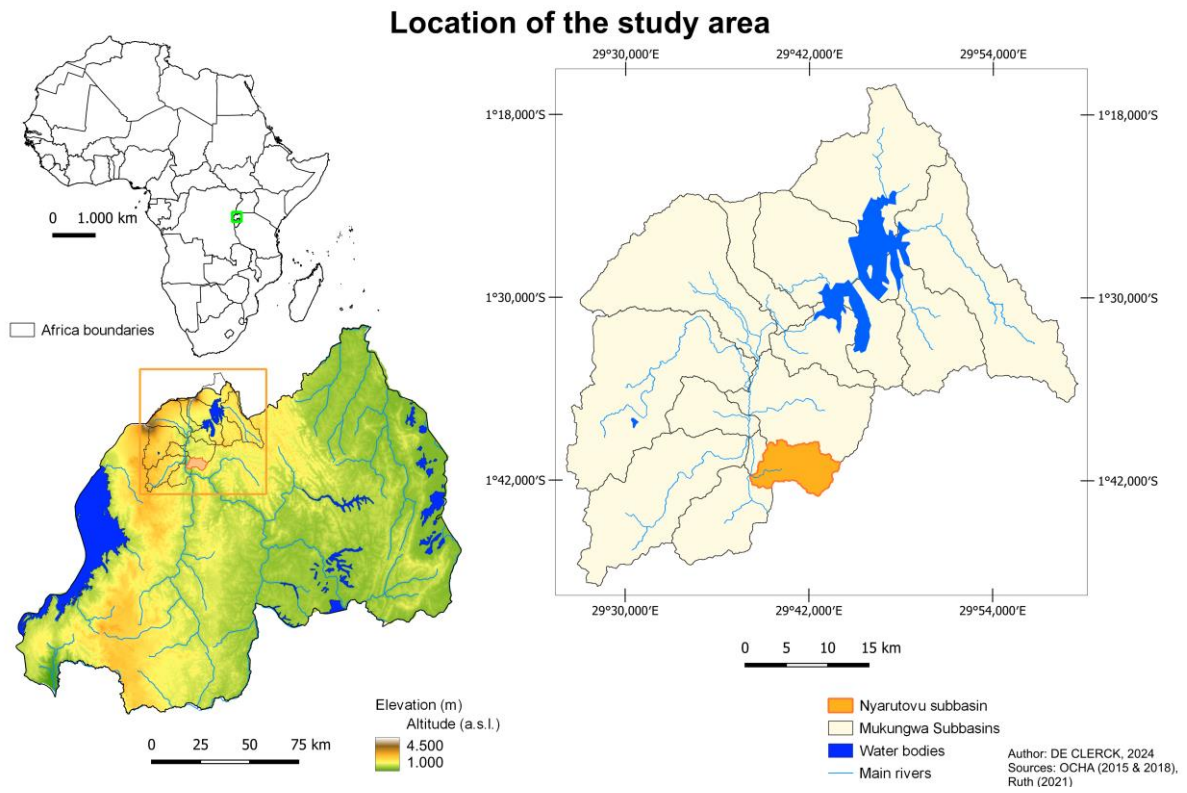

Figure 1. Location of Nyarutovu subbasin in Mukungwa watershed, of Mukungwa watershed in Rwanda (orange frame), and of Rwanda in Africa (green frame).

Rwanda, situated in East Africa and landlocked, covers an area of 26,338 km², with approximately 25,364 km² constituting land surfaces (Karamage *et al.*, 2017). As of 2022, its estimated population stands at 13,776,698, with 17.4% residing in urban areas. This developing nation exhibits an impressive growth rate of 2.3% and is projected to reach a population of 21,886,077 by 2050, with 29.6% living in urban areas. However, poverty remains in this country where, in 2016, 52% of the population lived with less than 2.15 USD per day (United Nations Population Division, 2018; World Bank, 2017).

The "Land of a Thousand Hills" aptly describes Rwanda, given its altitudes ranging from 915 m to 4486 m and a mean steep slope of 22% (Karamage *et al.*, 2017). This notable topography is a consequence of the geological context of the region: Rwanda lies within the western branch of the East African Rift system. This rift system currently divides Africa into two parts, forming graben structures and giving rise to volcanic activity, such as the Virunga volcanic chain, five of whose volcanoes are partially located in Rwanda (Chorowicz, 2005).

Rwanda is located just below the equator and enjoys a tropical temperate climate due to its high elevation. Seasonal fluctuations are driven by the Intertropical Convergence Zone (ITCZ) and are characterized by two rainy seasons: (1) the long rainy season from March to May and (2) the short rainy season from October to December (Figure 2). Rainfall is unevenly distributed across the country: the western part experiences more rainfall than the eastern part (Figure 3). High rainfall amounts are found in high-altitude regions and are caused by forced convection (Ntwali *et al.*, 2016). Long-term averages range between 805 mm and 1725 mm (Karamage *et al.*, 2017).

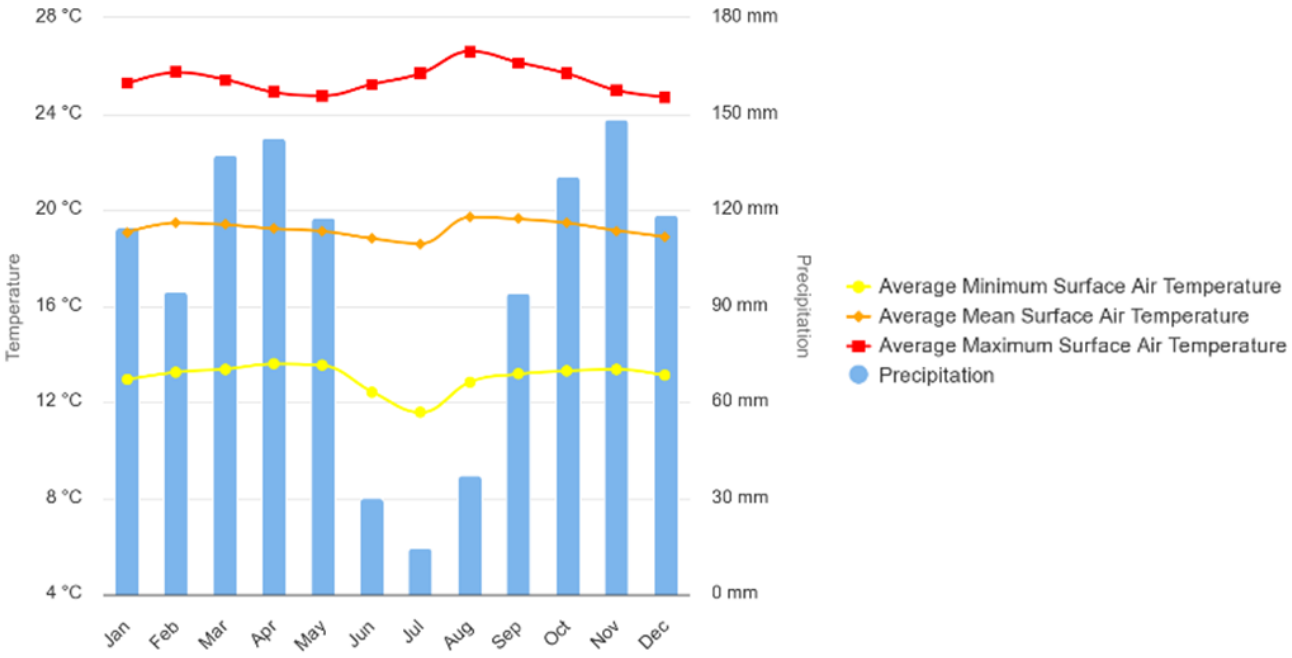

Figure 2. Climate diagram showing monthly rainfall and temperatures in Rwanda (World Bank, 2021).

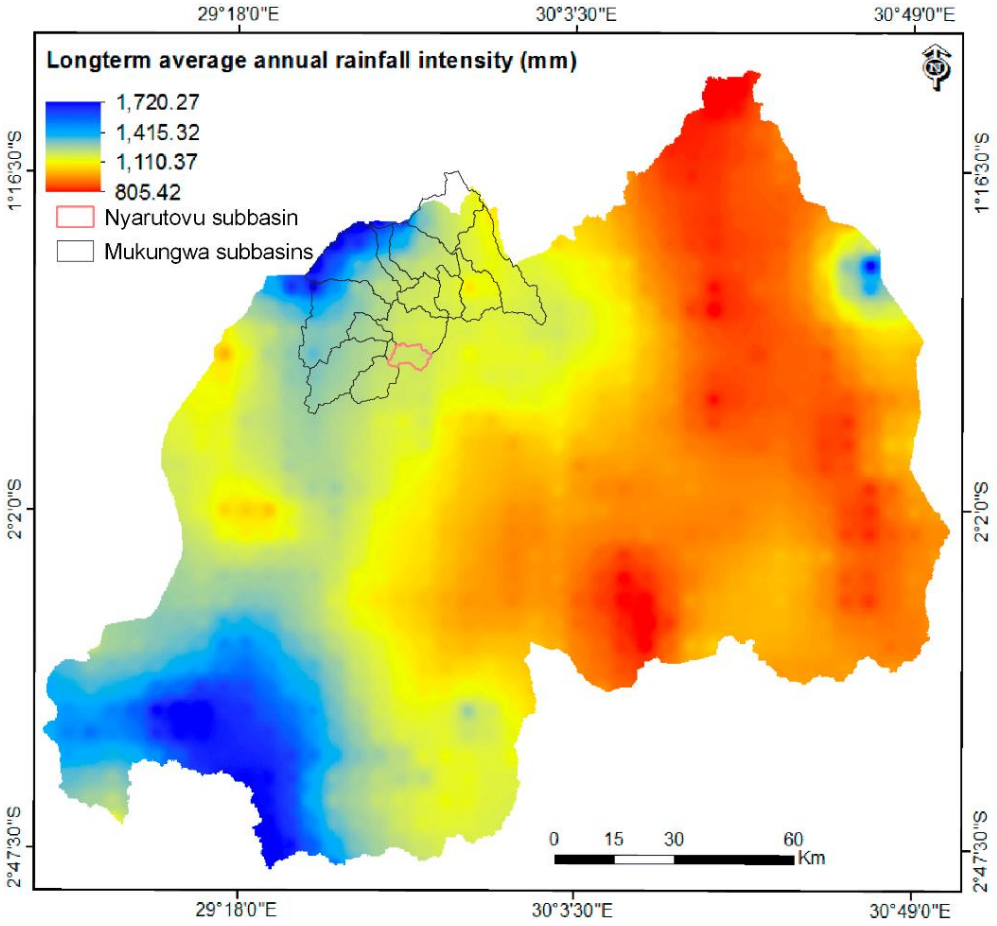

Figure 3. Long-term average annual precipitation in Rwanda and location of Nyarutovu and Mukungwa subbasins (Karamage *et al*., 2017; modified).

Mukungwa watershed is located in the western part of the country, covering an area of 1888,9 km². The topography of the Mukungwa watershed is very hilly as altitude ranges from more than 4400 m to 1400 m. Mukungwa River flows southwards into the Nyabarongo River and eventually flows into the Kagera River before reaching Lake Victoria and forming the White Nile. This study focuses on the Nyarutovu subbasin of the Mukungwa watershed (See Figure 1, and Table 1). The Nyarutovu subbasin has an area (A) of 45.15 km² and a perimeter (P) of approximately 42.95 km. Its Gravelius coefficient $(\mathrm{K_G})$ can be calculated as follows:

$$\mathrm{K_G} = 0.28\,\frac{\mathrm{P}}{\sqrt{\mathrm{A}}} = 0.28\,\frac{42.95}{\sqrt{45.03}} = 1.79.$$

Altitude in Nyarutovu subbasin varies between 1416 and 2379 m. A hypsometric curve is depicted below (Figure 4) to provide a clearer visualization of the relief of the Nyarutovu subbasin.

Subbasin	Area (km^2)	Perimeter (m)	Gravelius coef.	Longest flowpath length (km)	Longest flowpath slope (M/M)	Average basin slope (M/M)	Basin relief (M)	Drainage density (km/km^2)
Nyarutovu	45.15	42.95	1.79	15.04	0.062	0.41	962	0.497

Table 1. Key parameters and metrics of the Nyarutovu subbasin.

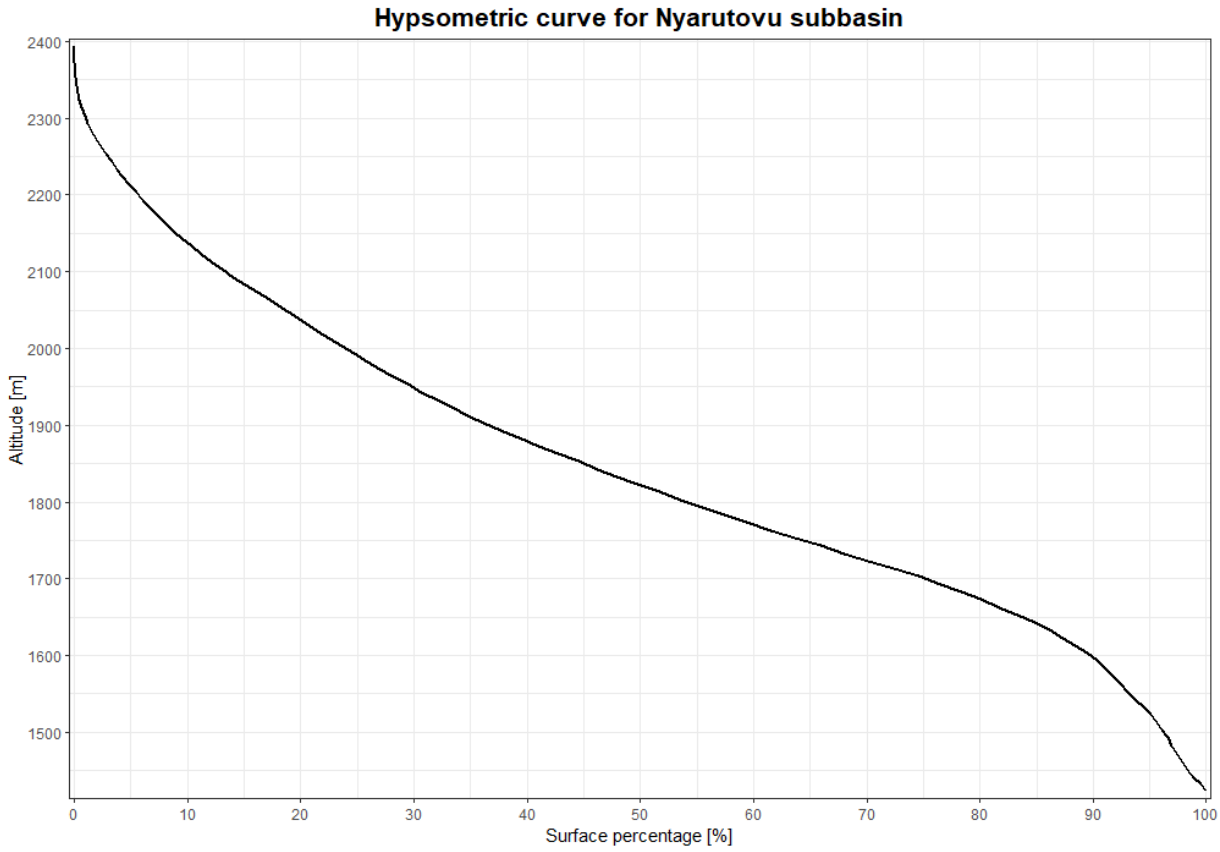

Figure 4. Hypsometric curve of Nyarutovu subbasin.

The main rivers[2] and their corresponding longitudinal profiles are displayed in Figure 5.

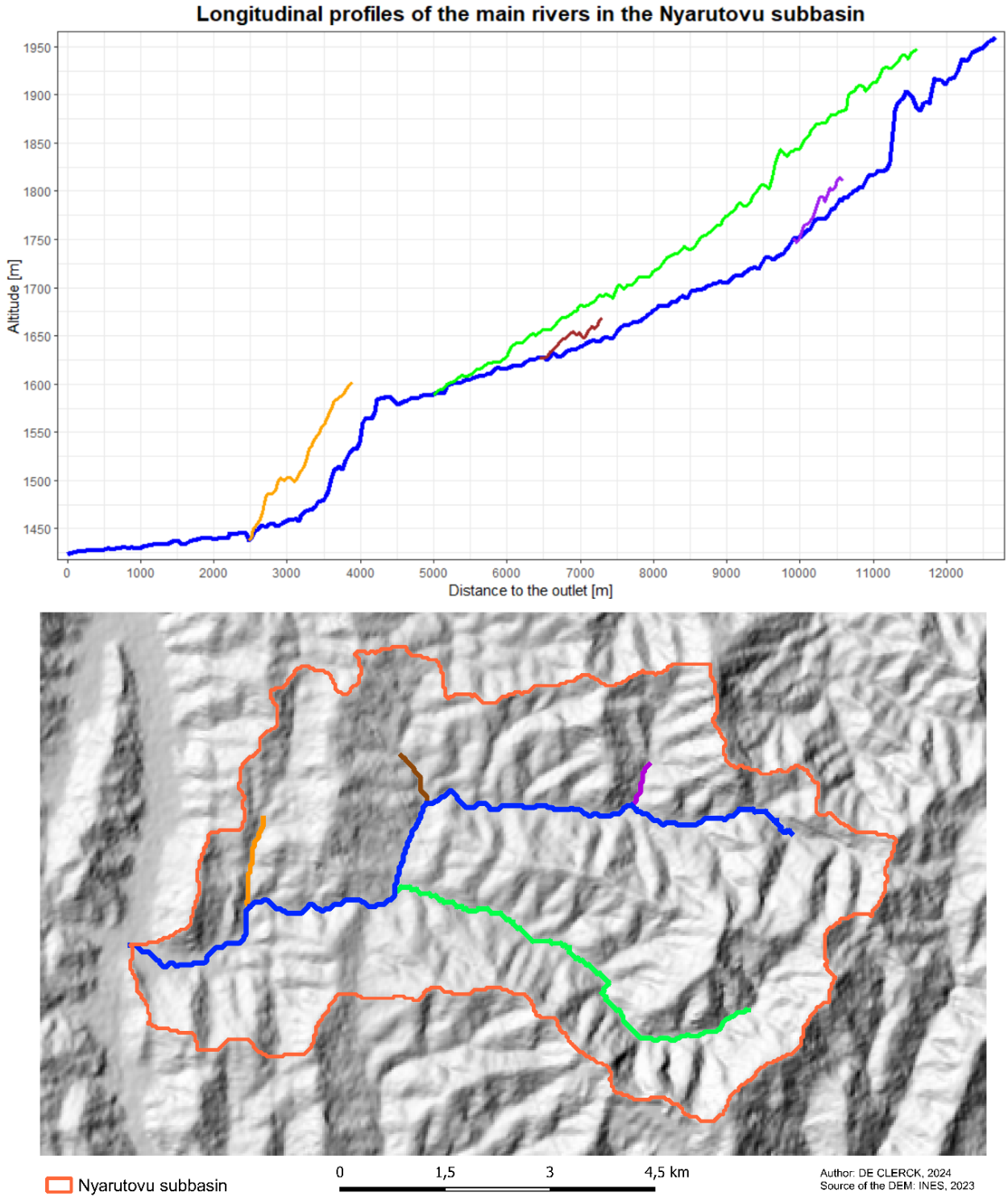

Figure 5. Longitudinal profiles of the main rivers in Nyarutovu subbasin (above) and a map depicting their respective locations (below). Note that the colors employed in both representations correspond to identical rivers.

[2] The methodology used to find the main rivers in the Nyarutovu subbasin and their corresponding longitudinal profiles will be explained later in the material and methods section.

The LULC[3] of the Nyarutovu subbasin is shown in Figure 6 and described in Table 2. The hills are intensively cultivated, often in terraces, with remnants of scattered forests (Figure 7).

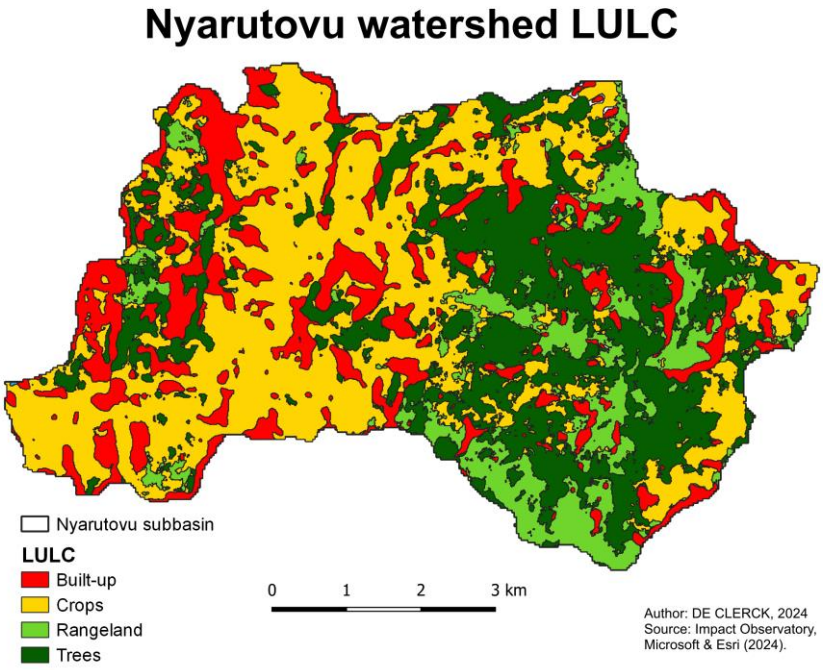

LULC	Part (%)
Crops	40.06
Built-up	18.79
Rangeland	12.69
Trees	28.46

Table 2. Description of the LULC in Nyarutovu watershed

Figure 6. Land Use Land Cover (LULC) map of Nyarutovu subbasins.

Figure 7. Picture of a typical slope and its LULC in the Nyarutovu subbasin (Picture by Victor De Clerck, 2023)

[3] The methodology used to find the LULC in the Nyarutovu subbasin will be explained later in the material and methods section.

3. Flooding in Rwanda

Flood events are common in Rwanda, particularly in the northern and western regions, where the study area is located (FloodList, 2024; Nsengiyumva, 2012). A database compiled by Li & Mind'je (2023) for the period 1988-2020 reveals that during this time, 159,191 people were affected by floods in Rwanda, with the North and West provinces accounting for 95% of these incidents (See Appendix 1 for a map of the provinces and districts of Rwanda). The devastated cropland covered an area of 116,353 hectares (98.5% in the North and West Provinces), and livestock losses totaled 7,719, with 98.1% occurring in the North and West provinces. Lastly, the number of ruined buildings reached 75,018, with 99.4% located in the North and West provinces.

The perception of Rwandans regarding flood hazards (See Appendix 2) is crucial in the disaster risk reduction process. A survey of 50 individuals from 11 districts — Nyabihu, Rubavu, Rusizi, Karongi, Rutsiro, Ngororero in the Western province; Musanze and Gakenke in the Northern province; Nyaruguru in the Southern province; Gatsibo in the Eastern province; and Gasabo in Kigali city (totaling 550 people) — reveals that 76% of respondents have experienced flooding in their area, and 74% believe their homes are at risk of flooding (Li & Mind'je, 2023).

Recently, flash floods (and landslides) occurred in May 2023 in Rwanda, resulting in the loss of more than 130 lives and the destruction of approximately 6,000 houses (Al Jazeera and News Agencies, 2023; ReliefWeb, 2023). The Mukungwa catchment area was also affected on May 3, 2023, with a significant number of houses destroyed (See Figure 8) and several casualties. This heavy toll is due to the suddenness of the flooding and the fact that it occurred during the night. Many other houses have been declared uninhabitable (see Figure 9), and their residents are awaiting expropriation, but they are uncertain about where or when they will be relocated.

Figure 8. Picture taken on 3 May 2023 of a house destroyed just beside the Nyamutera River, a tributary of the Mukungwa, where 11 people lost their lives (Picture by Déogratias Nahayo, 2023).

Figure 9. Picture of a maternity hospital affected by the May 2023 floods in Mukungwa watershed marked with a cross meaning that it will be expropriated. Note the mark left by the water, indicating the height reached by the flood (Picture by Victor De Clerck, 2023).

Flooding issues in Rwanda are accentuated by the large LULC changes that have taken place in recent years. Indeed, since the 2000's and the end of conflicts in the country, agriculture is developing and stable with about 80% of the Rwandan population depending on subsistence agriculture to live. From 1990 to 2016, 7090.02 km² (64.5%) of forests and 1715.26 km² (32.1%) of grasslands were lost while croplands increased by 9586.32 km² (+135.3%) and built-up areas by 355.02 km² (+304.3%). Deforestation and the conversion of natural grasslands for urban expansion and agricultural intensification are leading to an increase in runoff and its consequences, as built-up areas and croplands have a much lower infiltration capacity than forests and grasslands. As a consequence, the runoff depth (the total runoff of a watershed divided by its area) increased all over Rwanda, but especially in the districts that include Mukungwa watershed: Burera, Gakenke, Musanze, Ngororero and Nyabihu. It is also in these districts that intense LULC conversion occurred with a reduction of 1435.03 km² (73.9%) of the forests and an increase of 845 km² (+149.3%) of croplands during the period 1990-2016 as shown in Figure 10 (Karamage *et al*., 2017).

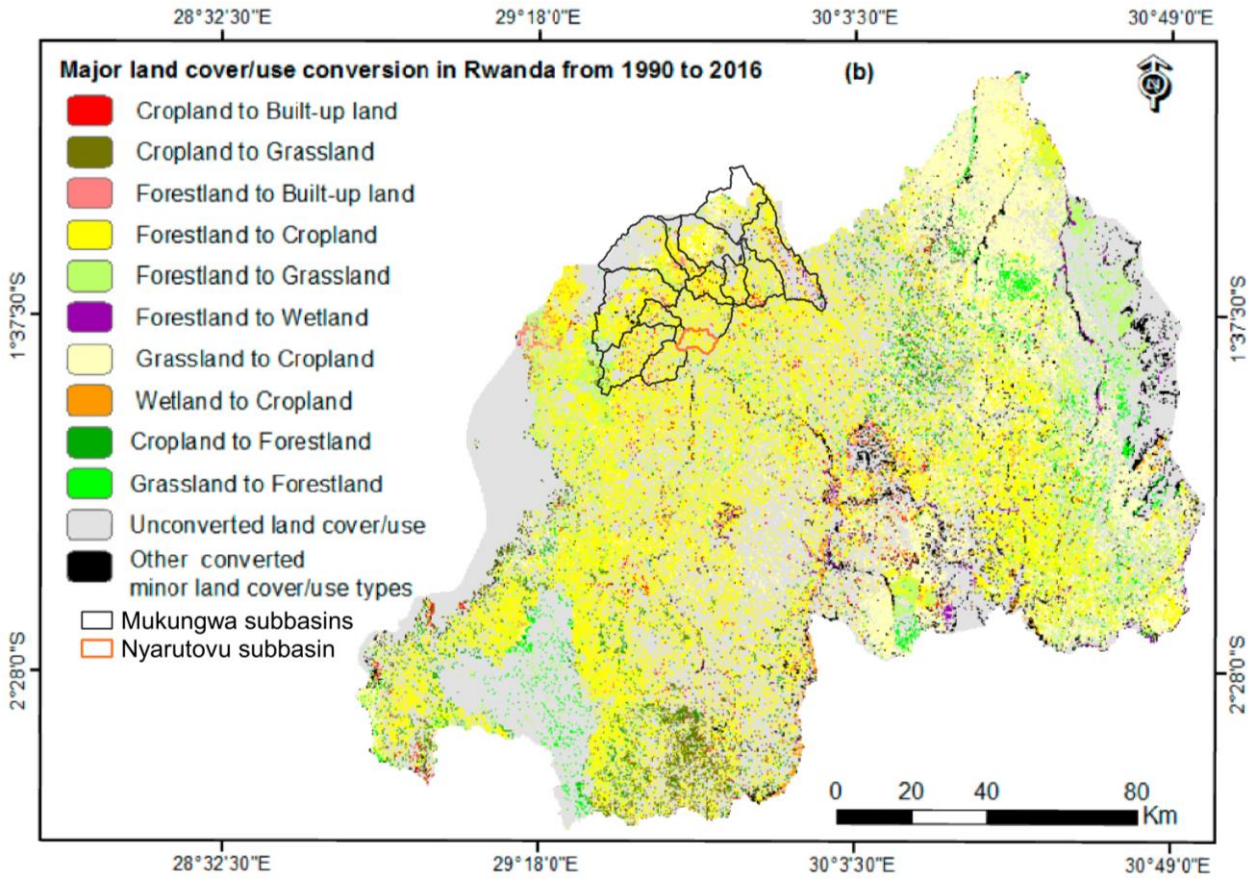

Figure 10. Major LULC conversion in Rwanda from 1990 to 2016 (Karamage *et al*., 2017; modified).

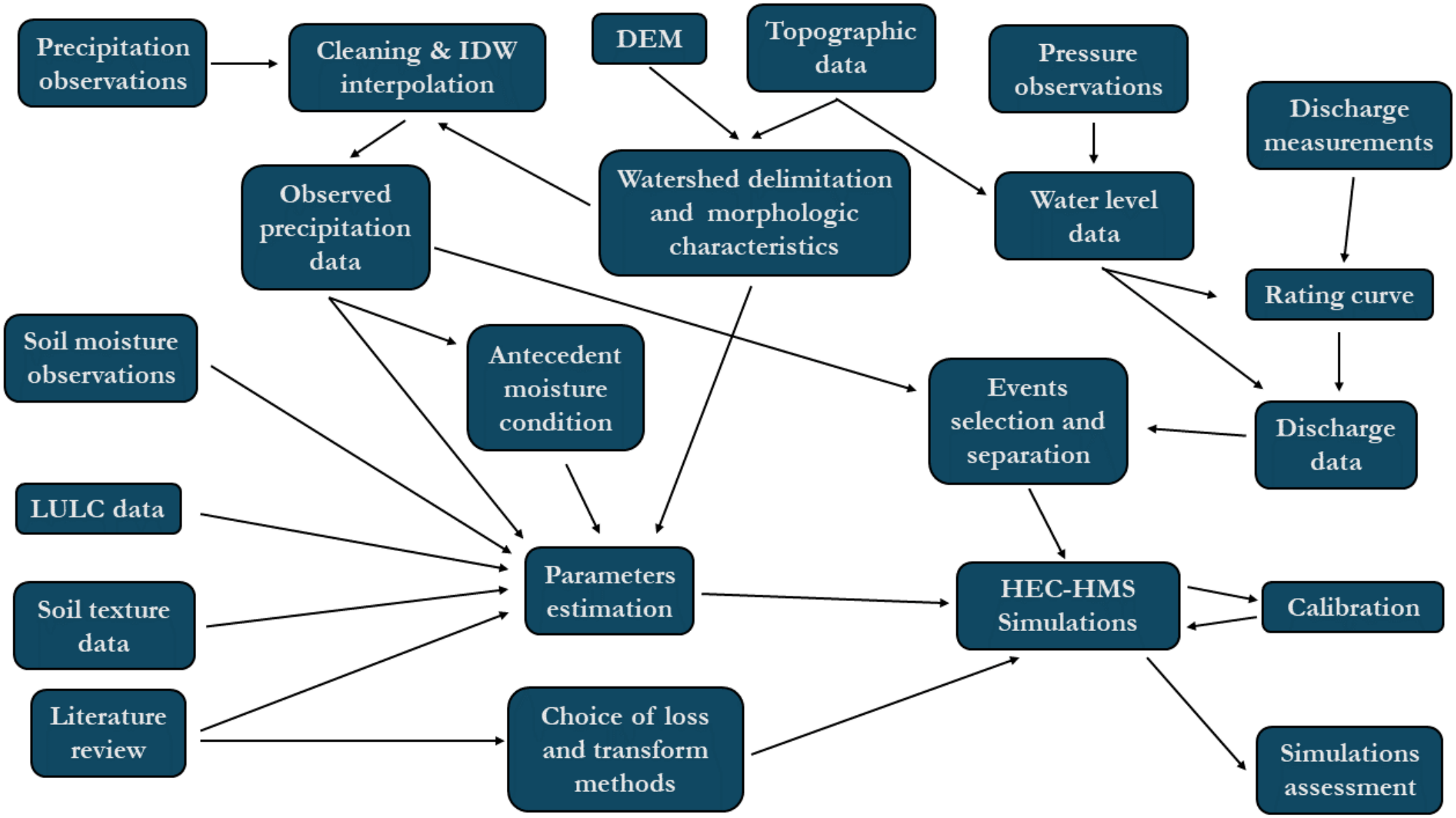

Figure 11. Methodology flowchart.

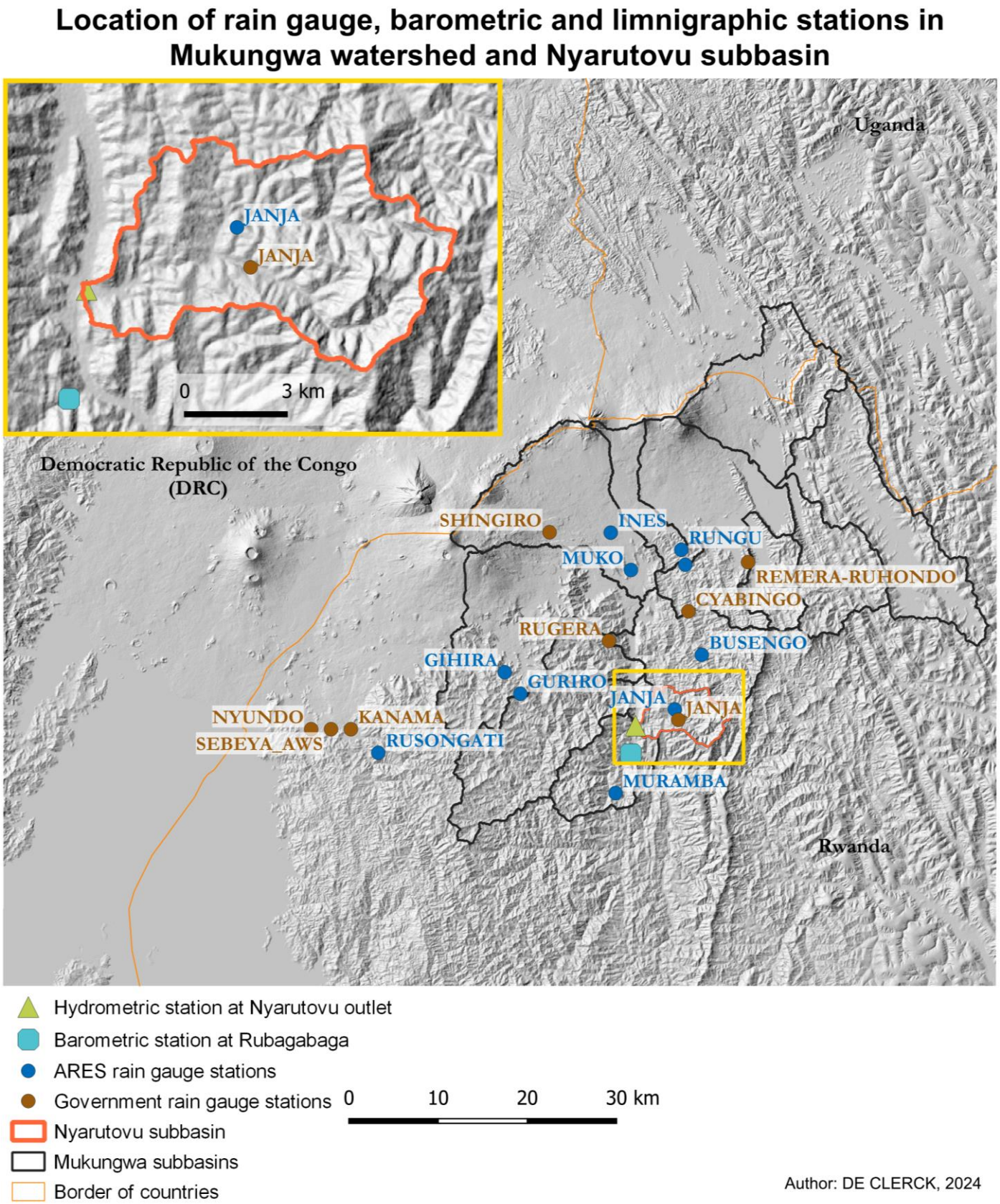

Figure 12. Map of the location of rain gauge, barometric and limnigraphic stations in Mukungwa watershed and Nyarutovu subbasin with a hillshade of the relief as the map background.

4.1. Topographic data acquisition

A field measurement campaign was carried out, with the great help of Noel from INES-Ruhengeri, to obtain precise data on the cross section (Figure 13) and the slope (Figure 14) of the Nyarutovu river close to the site of the hydrometric station (approximately 5 meters downstream). The instruments used were a Trimble R6 Model 2 GNSS receiver and a Leica R500 total station. Thanks to these measurements, we know that the banks height is just over 2.75 m. The data will also be used to calculate hydraulic radius for various water levels. The average slope of this section is 0.06%. Other GNSS measurements had also been made by Déogratias to determine the altitude of pressure probes, the use of which will be described later.

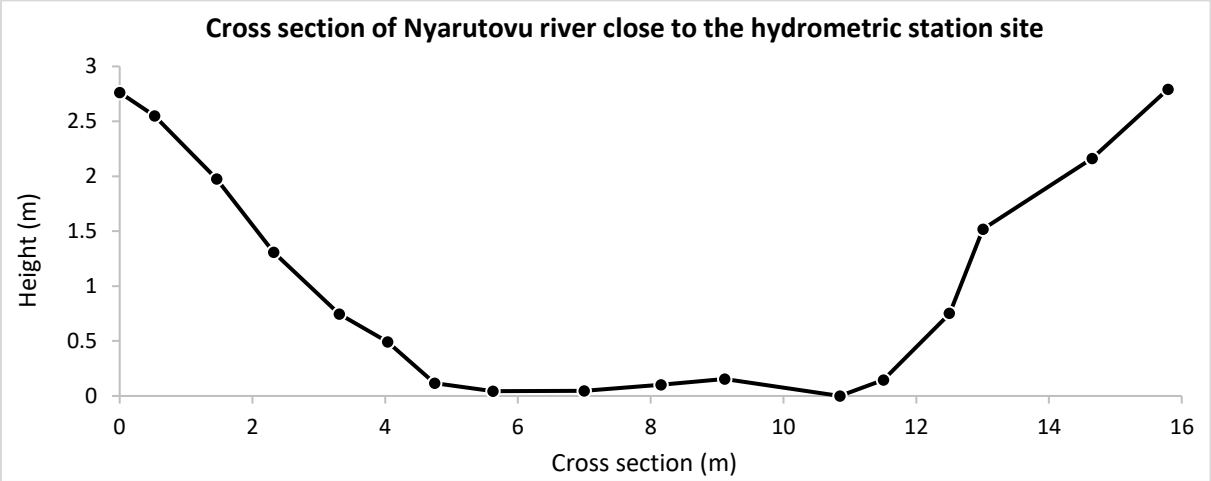

Figure 13. Measured cross section at Nyarutovu river at the hydrometric station site.

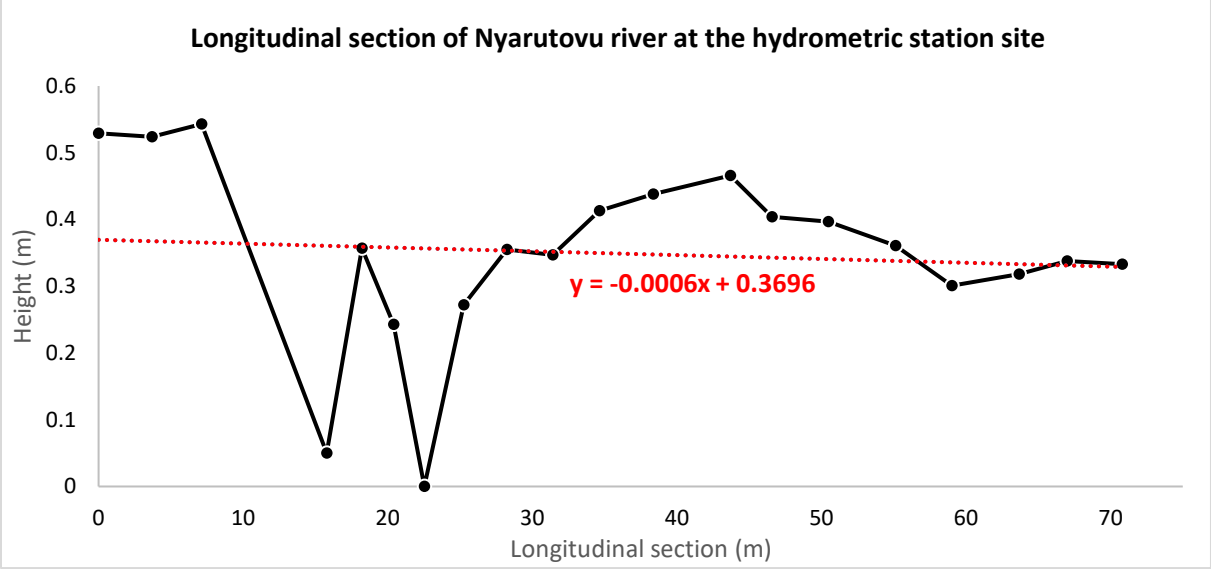

Figure 14. Measured longitudinal section of Nyarutovu river at the hydrometric station site.

4.2. Digital Elevation Model (DEM) data

In this study, A DEM (Digital Elevation Model) produced by INES (2023) based on the ALOS PALSAR Radiometric Terrain Correction (RTC) products released by Alaska Satellite Facility Distribution Active Archive Center (ASF DAAC, 2014) were used. This DEM were used to delineate Mukungwa watershed and its subbasins and to find the Nyarutovu subbasin (Figure 12). The DEM has a spatial resolution of around 30 m. The extent of the DEM is not limited to Rwanda, but straddle the Democratic Republic of Congo (DRC) and Uganda, as does the Mukungwa watershed, which does not stop at administrative borders. A hillshade of the topography of the study based on this DEM can be seen in Figure 12.

4.3. Delimitation of watersheds, subbasins and streams

The delimitation of watersheds, subbasins and identified streams was carried out in HEC-HMS[4]. This involved the following steps: (1) creation of the terrain model and the basin model, (2) linking the terrain with the basin model, (3) preprocessing of sinks, (4) preprocessing of drainage, (5) identification of streams, (6) creation of a break point and (7) delineation of the subbasins and potential merging of some subbasins.

4.4. Calculation of hypsometric curve and longitudinal profiles

The calculation of the hypsometric curve for Nyarutovu was performed in QGIS using the "hypsometric curves" algorithm from raster terrain analysis. Longitudinal profiles were also produced in QGIS using the "Profile Tool" extension proposed by Jurgiel *et al*. (2023).

4.5. Land Use Land Cover (LULC) data

The LULC data used was produced by Impact Observatory, Microsoft and Esri (2024). They produce each year a global map of LULC derived from ESA Sentinel-2 Level-2A imagery at 10 m resolution using a deep learning AI land classification model trained using billions of human-labeled image pixels from the National Geographic Society. A total of 11 LULC classes are described by the map. The map for 2023 contains 0.176% missing data (classified as clouds) for the Nyarutovu watershed, which is minimal and quite acceptable and preferable to

[4] HEC-HMS is a hydrologic modeling software that will be presented and described later.

another data source that would have information everywhere but much less precise and perhaps less recent.

4.6. Soil texture data

Soil texture data for the study area was derived from Li & Mind'je (2023) and Karamage *et al*., 2017). Both studies derived their soil texture map for Rwanda from the Africa Soil Information Service (AfSIS) that provide soil layers of clay, silt and sand fractions with a spatial resolution of 250m (Hengl *et al*., 2015). The soil textures were then derived from the soil texture triangle classification system developed by the USDA (see Figure 15). According to these studies the soil texture in Nyarutovu watershed is almost exclusively composed of clay loam (see Appendices 3 & 4) which correspond to a sand fraction between 20 and 45, a silt fraction between 15 and 53, and a clay fraction between 27 and 40 %.

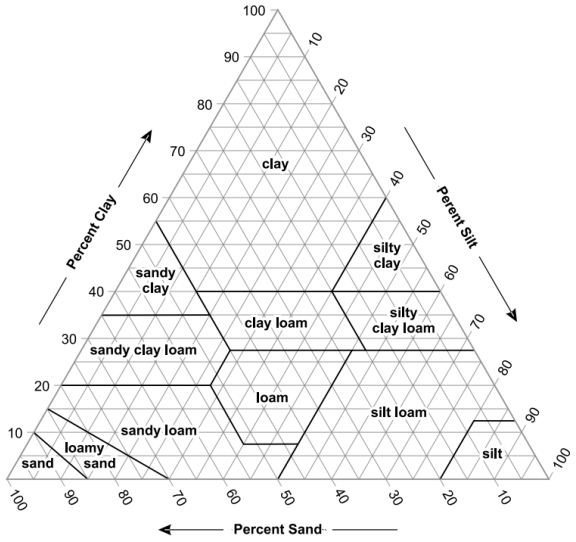

Figure 15. USDA soil texture triangle classification system (USDA, 2017)

4.7. Precipitation data

4.7.1. Data acquisition

Precipitation data was collected by the project team using 10 iMetos rain gauge stations (see Table 3) from Pessl Instruments. The iMetos ECO D3 and iMetos 3.3 were used. The main difference between these devices is that the 3.3 is a more comprehensive meteorological station, also measuring wind speed, relative humidity, dew point, soil water content, and more. However, all these rain gauge stations are equipped with the same double tipping bucket rain gauge, which has a surface area of 200 cm² (see Figure 16).These instruments have

a sensitivity of one tip per 0.2 mm and an accuracy of 5%. The maximum rain intensity that can be measured is 12 mm/minute (Pessl Instruments, 2024a). Measurements are sent and collected on "FieldClimate", a platform developed by Pessl Instruments specifically for data transfer, display and collection. Observations of precipitation at 15-minute time steps from November 2021 to September 2023 were available. Other rainfall data from the Rwandan government (24-hour time step), forwarded by Déogratias Nahayo, were also used. Project stations with 15-minute time steps will hereafter be referred to as "ARES stations" to distinguish them from "government stations".

Station name	Device type
BUSENGO	iMetos ECO D3
GIHIRA	iMetos ECO D3
GURIRO	iMetos ECO D3
INES	iMetos 3.3
JANJA	iMetos ECO D3
KARAMA	iMetos ECO D3
MUKO	iMetos ECO D3
MURAMBA	iMetos 3.3
RUNGU	iMetos ECO D3
RUSONGATI	iMetos ECO D3

Table 3. List of the 10 ARES rain gauge stations and their respective device types.

Figure 16. Picture of an ARES rain gauge station used for this study (Picture by Victor De Clerck, 2023)

4.7.2. Data cleaning

The first step in exploiting this data was to clean outliers. To do this, the data were manually sifted station by station, month by month, and up to the day when the outliers were identified. Comparisons with monthly averages for Rwanda, other ARES stations and nearby government stations were made to determine whether the data were valid or considered outliers. This resulted in the following summary table (Figure 17) of data from the 10 ARES rain gauge stations. This methodology involves an element of subjectivity. This is why, when data have been removed from the dataset, comments have been made in the Excel sheet to justify the removal of the data and to try to be as objective as possible. These comments are available online on the following Excel sheet: Summary_table_rain_gauge_stations.xlsx.

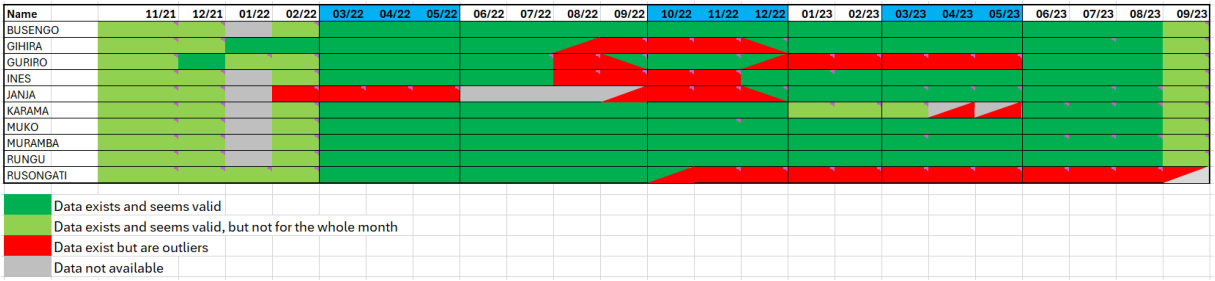

Figure 17. Table summarizing the existence, validity, and comments on the data from the 10 ARES rain gauge stations. The months highlighted in blue correspond to the rainy seasons.

4.7.3. Spatial interpolation

In order to move from point data to continuous data and calculate precipitation in the Nyarutovu subbasin, spatial interpolations were carried out between rain gauge stations. Given the large number of interpolations required (one interpolation every 15 minutes for just under two years of data), geostatistical approaches such as kriging were ruled out. Two methods readily applicable to the data were available: (1) the Thiessen polygon method (THI) and (2) the Inverse Distance Weighting method (IDW).

The THI method is also known as the neareast neighbor method. In this method, the estimated values are equal to the value of the nearest station. This method requires the construction of a Thiessen polygon network. This network was created in QGIS to determine the weight of stations to calculate the Nyarutovu mean precipitation. It is therefore possible to assign a weight to each station, which is in fact the proportion of the Nyarutovu watershed for which it is the closest station, and which will therefore have the same value as the station in question. When the Janja station is available the weights are 0.996 and 0.004 for Janja and Busengo stations respectively. When Janja station is not available, the weights are 0.884 and 0.116 for Busengo and Muramba stations respectively.

The IDW method is a little more complex, as it will take all the rain gauge stations into account but their weights decrease with increasing distance from the point that we try to simulate. Each predicted point of the interpolation is calculated using the following formula:

$$\hat{Z}(s_0) = \frac{\sum_{i=1}^{n} w(s_i) Z(s_i)}{\sum_{i=1}^{n} w(s_i)} \qquad w(s_i) = \frac{1}{d(s_0, s_i)^p}$$

- $\hat{Z}(s_0)$ is the predicted value at location s_0
- $w(s_i)$ is the weight of measured point i
- $Z(s_i)$ is the value of measured point i
- $w(s_i)$ is the weight of measured point i
- $d(s_0, s_i)$ is the distance between predicted point s_0 and measured point s_i

Figure 18. Inverse Distance Weighting (IDW) spatial interpolation method formula (Jonard, 2023)

Where the exponent p must be chosen. This parameter is generally assumed to be equal to 2 and this value of 2 has been chosen as it is suitable for mountainous regions (Gilewski, 2021). To implement this method, the Python console of QGIS was used. A script was built, with the invaluable help of Thomas Dethinne (PhD student from ULiège). This script performs an IDW interpolation of precipitation measured at the rain gauge stations and then spatially averages it over the Nyarutovu subbasin, for each time step entered.

A comparison of the daily precipitation at Nyarutovu subbasin calculated via THI and IDW methods for the period January to May 2023 (Figure 19) shows that the two methods produce very similar results (R^2 = 0.936). The reason for choosing the January-May period will be explained later in this section.

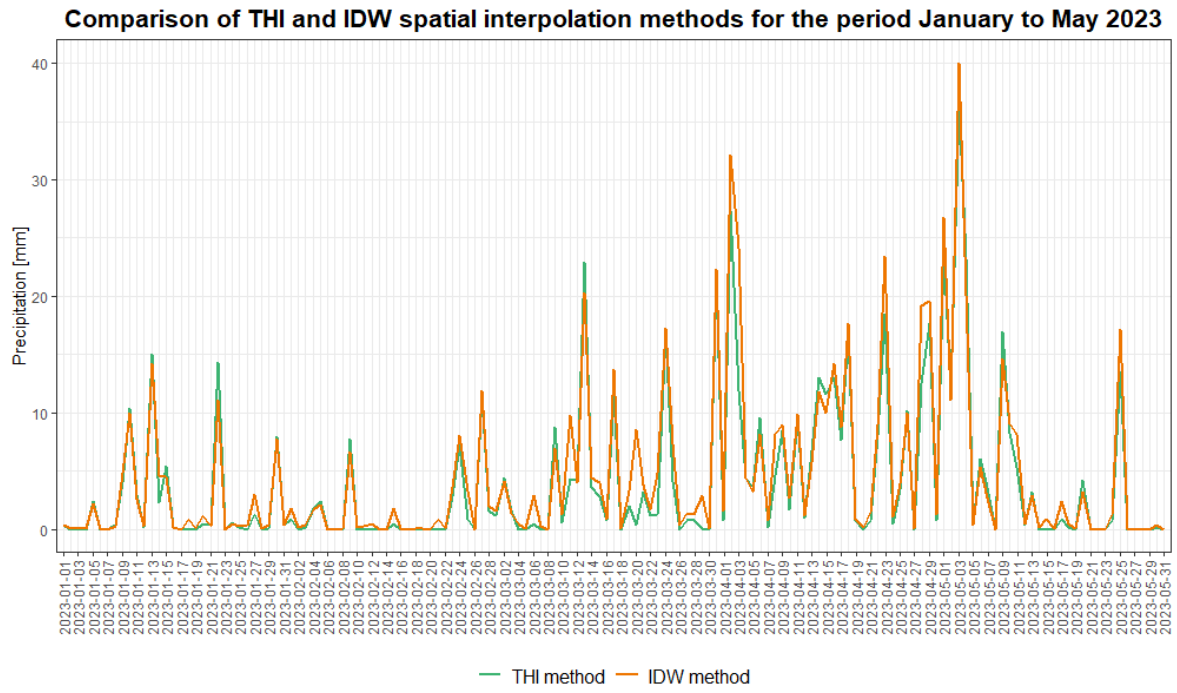

Figure 19. Comparison of daily precipitation at Nyarutovu subbasin calculated from THI and IDW spatial interpolation methods for the period January to May 2023

To determine which method is best suited to our study area (mountainous and tropical), a litterature review was performed. Maires & Fares (2011) found in their study of a mountainous region of a tropical island that: "the largest RMSE is produced by the Thiessen polygon method that ignores secondary information", Ly *et al*. (2013) state that the Thiessen polygon method is "not suitable for mountainous regions, because of the orographic influence of rain". In contrast, Jalili Pirani & Modarres (2020) found that "the Thiessen polygon method produced better results in a low density network" but our region cannot be considered as low density network. Consequently,the IDW method was chosen.

4.7.4. Number of stations for IDW interpolation

Next, a comparison was made between the IDW method with all 10 ARES stations and only the 3 stations closest to Nyarutovu namely Busengo, Janja and Muramba stations (Figure 20). The results show that taking only into account the 3 nearest stations does not change Nyarutovu precipitation average in most cases (R^2 = 0.997). On certain days, such as May 15, 2023, the differences are more marked. This is due to heavy rainfall: 17.6 and 24.8 mm at the Ines and Muko stations respectively. In this context, it seems preferable to consider only the 3 closest stations, so as not to take into account heavy storms that affected distant rain gauge

stations, even if their influences on the interpolation is greatly reduced by their long distances from the Nyarutovu subbasin.

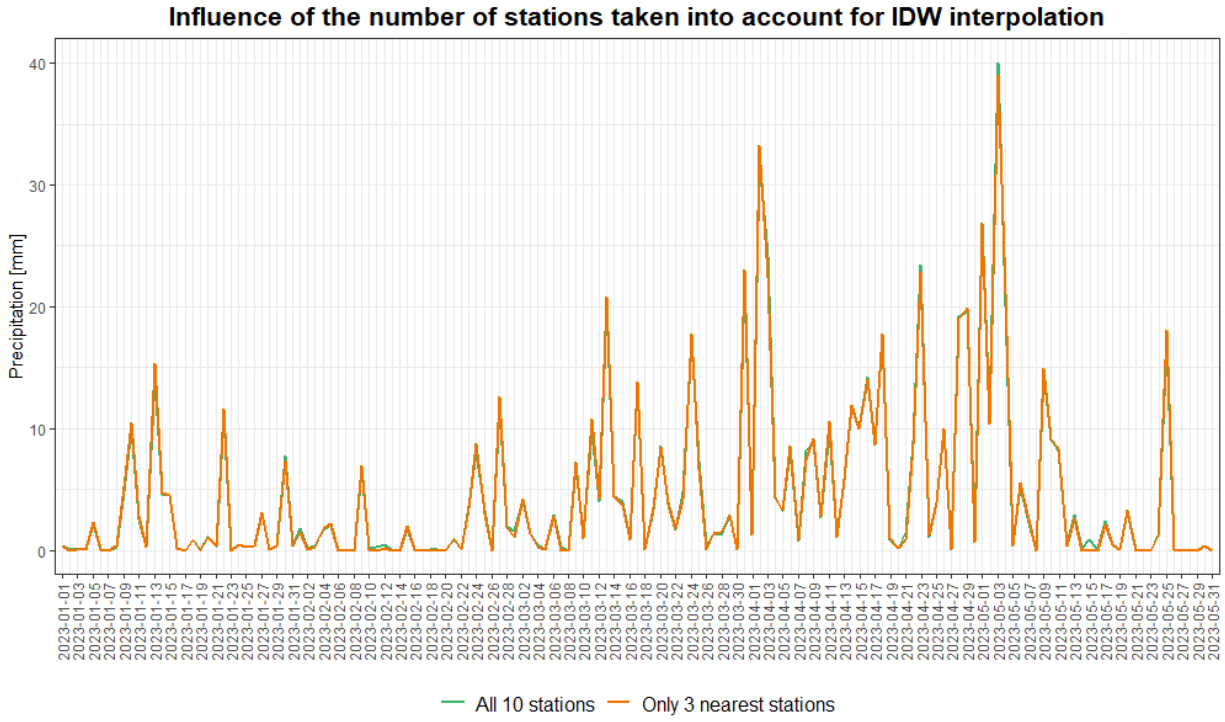

Figure 20. Comparison of daily precipitation calculated with IDW interpolation considering only the 3 nearest and all 10 ARES rain gauge stations.

4.7.5. Cross validation at Janja station

As the Janja station, which is the closest station to Nyarutovu subbasin (it lies within the basin), is only available from January to October 2023, with interesting months (with recorded precipitation) between January and May 2023 (Figure 17), a cross validation was carried out to determine whether it was possible to work on the months when the Janja station is not available. In other words, the value estimated by the IDW interpolation carried out without the Janja station was compared with the value observed at Janja. The estimated values were found in the QGIS Python console with the above-mentioned script, which was adapted to calculate the estimated value for the Janja station instead of the average for the Nyarotuvu subbasin. The results show that estimated values at the Janja station deviate significantly from measured values (R^2 = 0.51 & RMSE = 8.63 mm) (see Figure 21).

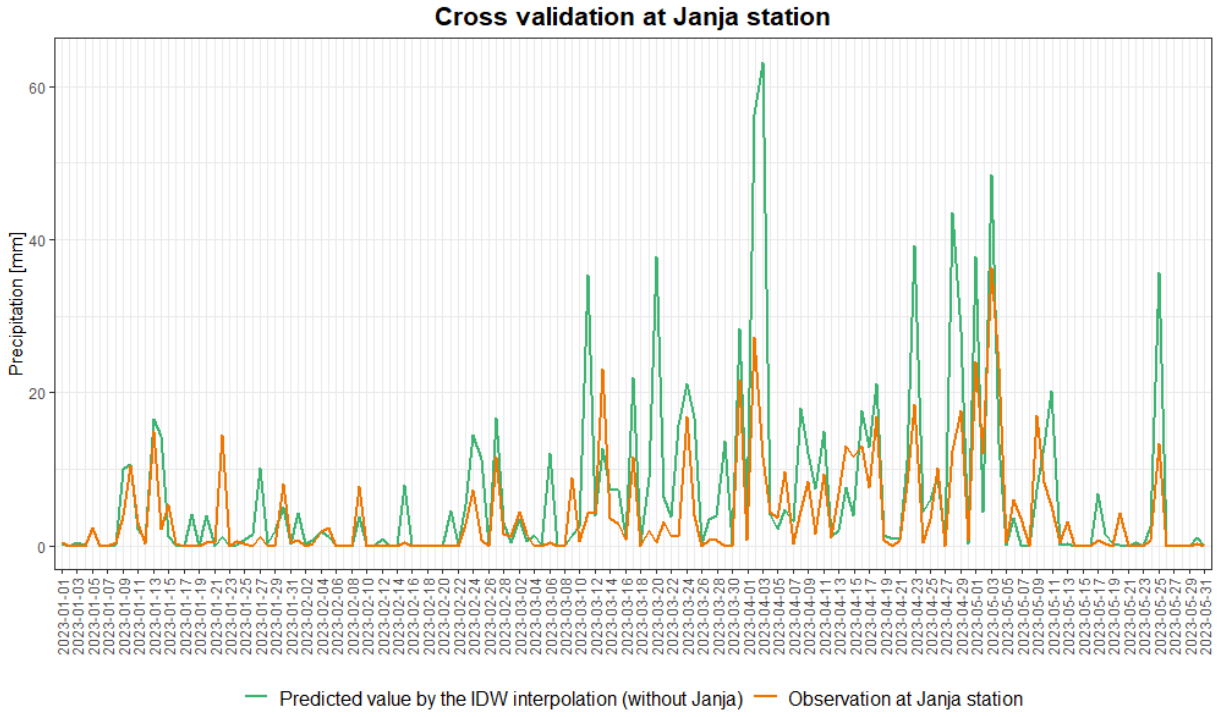

Figure 21. Comparison between predicted precipitation values at the Janja station by IDW interpolation (without considering the Janja station) and observed values at the Janja station for daily precipitation data.

Differences are even more pronounced when time steps are reduced, as shown in Figure 22, where 3-hour time steps were used and an arbitrary period was chosen for illustration. We observe that predicted values can be up to almost ten times greater than observed values, and vice versa.

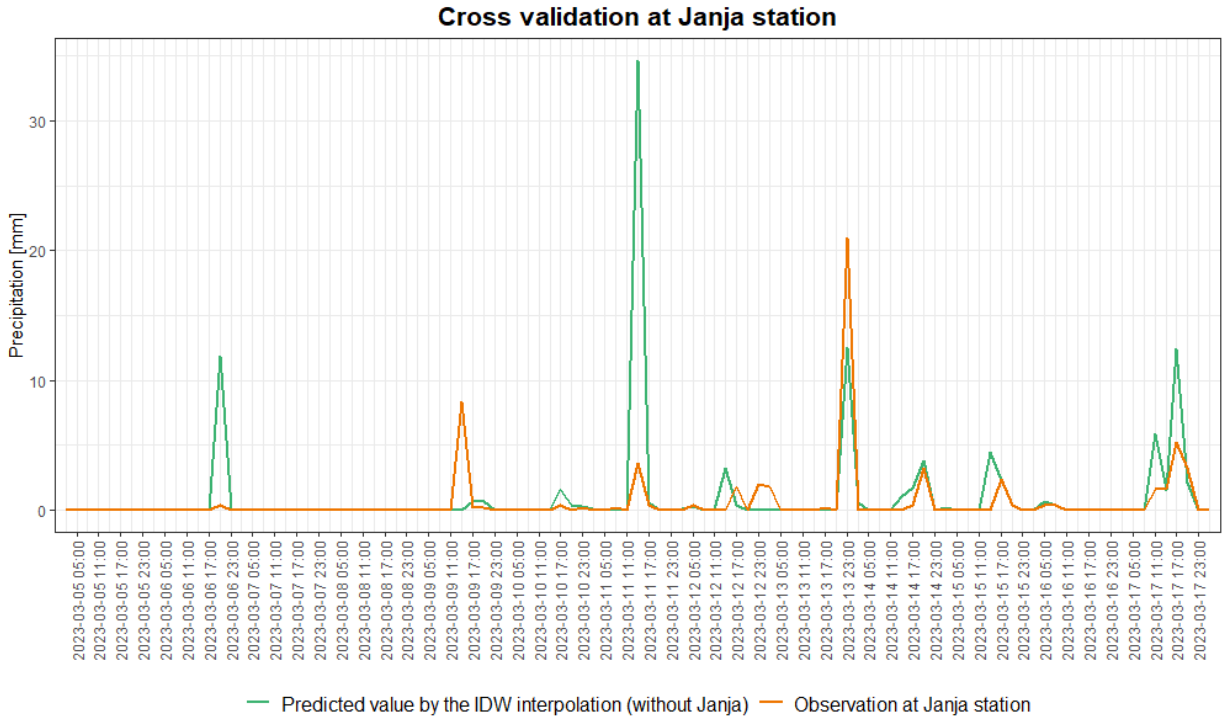

Figure 22. Comparison between predicted precipitation values at the Janja station by IDW interpolation (without considering the Janja station) and observed values at the Janja station for 3-hour time steps precipitation data.

Therefore, it seems wise to work only on the period when Janja station data is available, i.e. from January to May 2023.

4.7.6. Comparison of ARES and government Janja stations

In order to validate and rely on the data from the ARES Janja rain gauge station, a comparison was made with the daily data from the government Janja station. The two stations are just over 1.2 km apart. Unfortunately, after requests were made to the Rwandan government, uncertainty remains as to the time interval used in the daily government data (whether it is counted from 00:00 to 00:00 or from 06:00 to 06:00, for example). This is why a moving average over 3 days is presented in Figure 23 instead of the daily values. The results show that the two stations measured fairly similar precipitation (R^2 = 0.884 & RMSE = 1.97 mm).

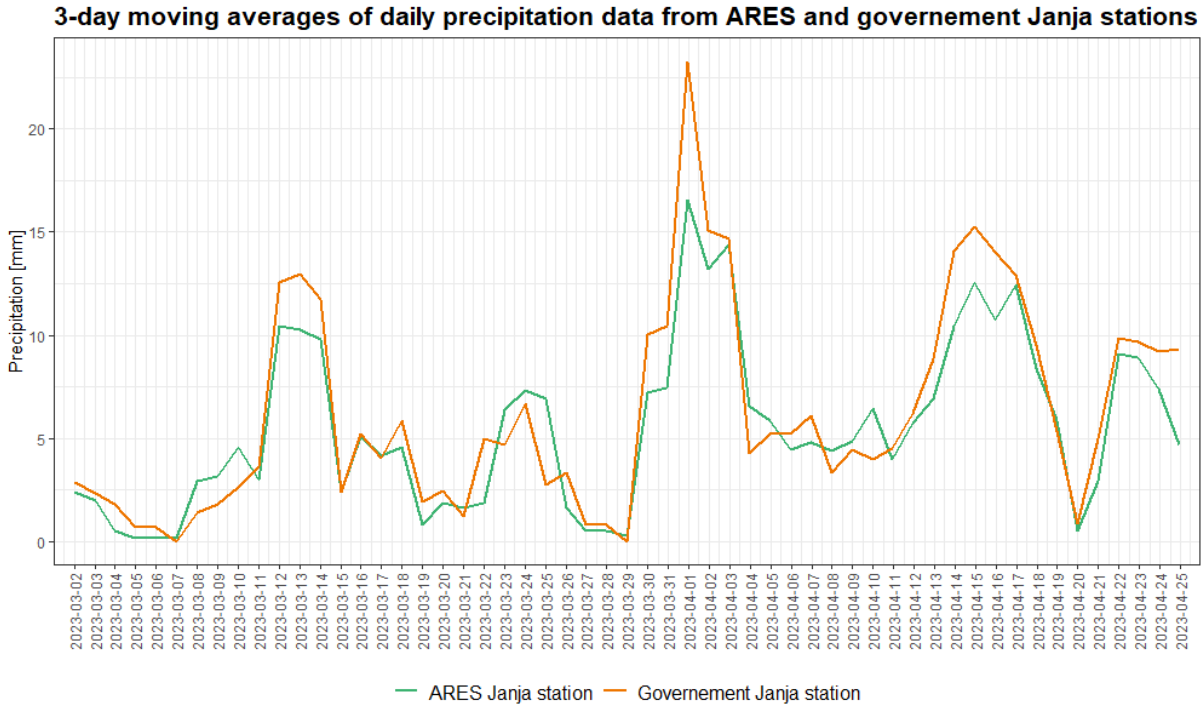

Figure 23. Comparison of moving averages over 3 days of daily precipitation data from ARES and government Janja rain gauge stations.

Finally, to summarize this precipitation data section, only data from January to May 2023 will be used, using the IDW spatial interpolation method, in which only the 3 nearest stations are taken into account.

4.8. Discharge data

Obtaining continuous discharge data is challenging because measuring river flow is very difficult. Measuring water level, on the other hand, is easily done with pressure probes. This is why hydrologists usually rely on rating curves. A rating curve, for a specific hydrometric station, represents the relationship between different water levels observed on a staff gauge and the associated discharge (WMO *et al.*, 2007). Thanks to the rating curve, it is possible to convert the continuous water level time series into a continuous discharge time series. The methodology for calculating water levels and establishing the rating curve is described below.

4.8.1. Water level data

The water level can be measured with pressure probes. In this case, we used the widely used Van Essen probes, primarily designed to measure groundwater but also applicable for surface water level measurement (Van Essen Instruments, 2004). The principle involves measuring the

pressure in the water using a probe called Diver, alongside measuring the atmospheric pressure in the open air with a probe called BaroDiver. The pressure attributed to the water column is assumed to be equal to the pressure measured at the Diver minus the pressure measured at the BaroDiver (see Figure 24). However, it is important to note that the water column below the Diver is not measured. Therefore, whenever possible, it is advisable to place the Diver as close to the riverbed bottom as feasible, ensuring adequate water flow around the sensors of the Diver to prevent blockage and ensure accurate measurement of the water height of the river, rather than measuring stagnant water within the monitoring well itself (Van Essen Instruments, 2004). In our case, the Diver is about 20 cm above the maximum depth of the riverbed.

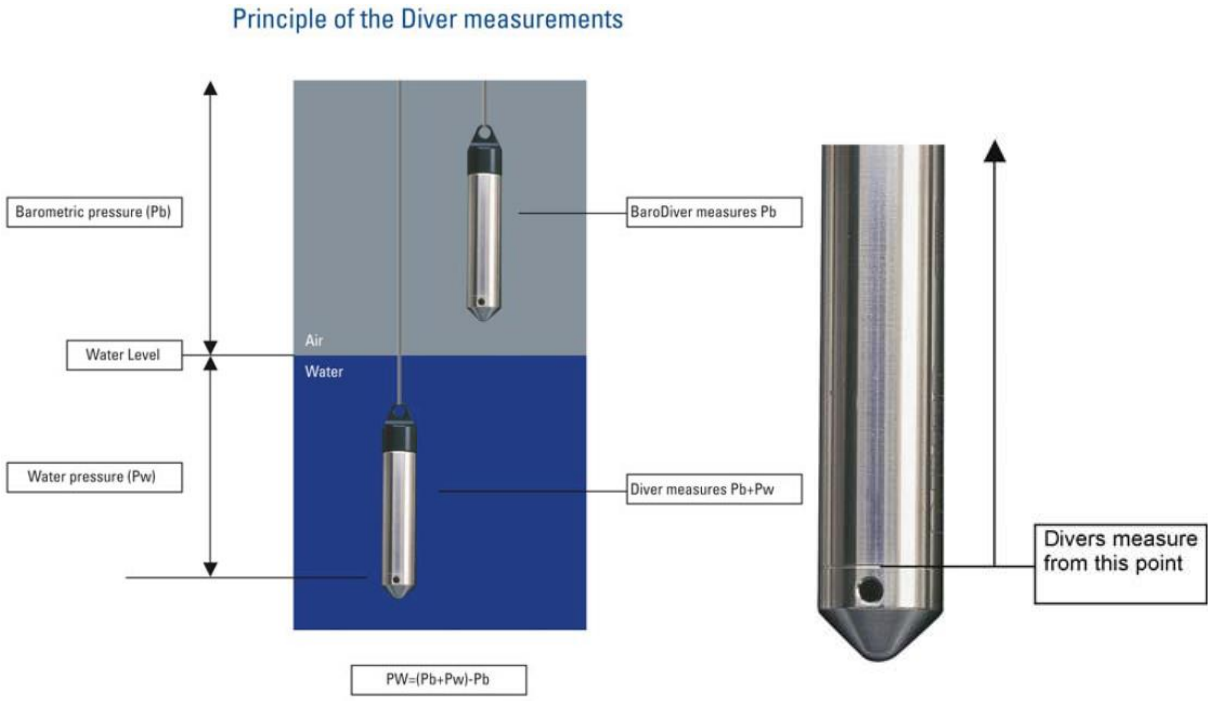

Figure 24. Principle of water level measurements with Diver and BaroDiver (Van Essen Instruments, 2004).

The BaroDiver used is situated slightly over 3 km away from the Nyarutovu hydrometric station, which is sufficiently close to assume that the atmospheric pressure measured at the BaroDiver is likely to be nearly identical to that at the Diver. According to Van Essen Instruments (2004), one BaroDiver is adequate for an area of 15 km², which corresponds to a circle with a radius of approximately 2.185 km.

Figure 25. Picture of the Nyarutovu hydrometric station where the Diver is placed. Note the staff gauge attached to the monitoring well (Picture by Victor De Clerck, 2023).

To ensure accurate readings, both probes should ideally be at the same altitude, as atmospheric pressure decreases exponentially with altitude (Van Essen Instruments, 2004). However, in this case, the two probes are not precisely at the same altitude: the Diver at Nyarutovu is positioned at 1416.488 m, while the BaroDiver is at 1408.735 m. The altitude difference amounts to 7.753 m, which is relatively small and thus acceptable. Nonetheless, a correction was applied to the pressure measured at the BaroDiver in an attempt to compensate for the altitude difference between the two stations. The formula used, as provided by Van Essen Instruments (2004), is as follows:

$$P_h = P_0 * e^{-\frac{(M*g*h)}{(R*T)}}$$

Where:

P_h = atmospheric pressure at elevation height H (in this case, at Diver : 1416.488 m)

P_0 = atmospheric pressure at reference point (in this case, at Baro : 1408.735 m)

M = $28.8 * 10^{-3}$ kg/mol (molecular mass of air)

g = 9.81 m/s² (standard gravity)

h = height between the two stations in meters (in this case, 7.753 m).

R = 8.314 J/mol/K (gas constant)

T = temperature in Kelvin (in this case, the temperature measured at BaroDiver)

Once these pressure data have been corrected from the elevation difference, the water level were calculated using the following formula (Van Essen Instruments, 2016):

$$WL = 9806.65 * \frac{p_{Diver} - P_{BaroDiver}}{\rho * g}$$

Where:

WL is the water level (cm), p is the pressure in cmH_20, g is the acceleration due to gravity (9.80665 m/s²) and ρ is the density of water (1000 kg/m³).

This formula can be simplified to:

$$WL = p_{Diver} - P_{BaroDiver}$$

The BaroDiver measures pressure every hour, while the Diver measures pressure every 15 minutes. To calculate the water level every 15 minutes and ensure a minimum time interval between Diver and BaroDiver measurements, the pressure measured by the Diver at 12:30, 12:45, 13:00 and 13:15 was compared with the pressure measured by the BaroDiver at 13:00 and so forth.

Finally, the water levels have been adjusted. Negative water levels have been set to zero, as they correspond to periods when the Diver is in the open air (river below the Diver) and the measured water level is simply the difference in atmospheric pressures measured by the two probes. While these differences may stem from a genuine disparity in atmospheric pressure between the probe locations, they are primarily attributed to the limited accuracy of the probes. For our case study, negative water levels typically remain above -2 cm. Therefore, water levels below 2 cm have also been adjusted to zero, as it is challenging to ascertain whether these 2 cm represent an actual water column measured at the Diver or are simply the result of measurement inaccuracies.

4.8.2. Rating curve

To establish the rating curve, two types of data were required: (1) the discharges and (2) the corresponding water levels. First, the methodology employed to measure discharge is explained below.

4.8.2.1. Discharge measurements

The discharge data has been collected in the field via two low-cost measurements methods: (1) the flow probe method and (2) the float method. The flow probe method could be assumed to be more accurate than the float method if rigorously implemented. However, the float method is recommended in situations where the use of a flow probe is challenging or impossible due to excessively high or low velocity, excessive turbulence, or other factors.

4.8.2.1.1. Flow probe method

This method employs an instrument known as a flow probe, which is designed to determine the velocity of a stream when placed in it. It works as follows: the flowing water rotates a propeller at a certain speed, which can be measured and converted to ascertain the velocity of the river. In our case, a YSI FP2111 flow probe (Figure 26) was used. According to the FP211 specification sheet (YSI, 2020), the FP211 accuracy is 0.1 ft/s (i.e. 0.03048 m/s).

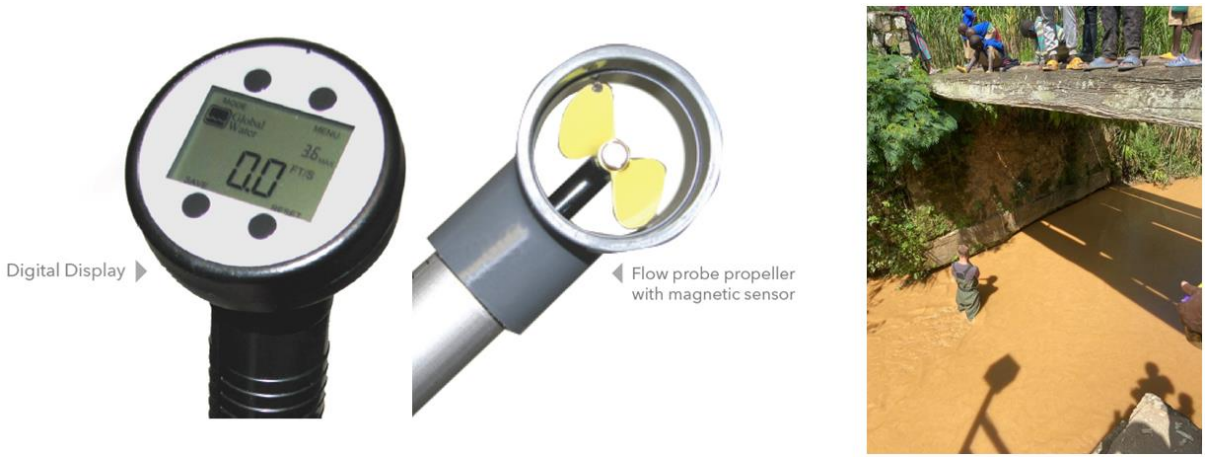

Figure 26. From left to right: 1) pictures of the FP211 flow probe with its digital display, 2) the propeller component (YSI, 2020), and 3) a picture demonstrating the utilization of the FP211 in a river within the Mukungwa watershed (Picture by Déogratias Nahayo, 2023)

The field measurement methodology was previously established by the project team. The river section was measured using 7 depth equidistant measurements, with the first and last measures taken at the river banks. To estimate the velocity of the Nyarutovu river, 6 equidistant flow velocity measurements were conducted to represent the cross-section of the river. These velocity measurements were taken at the midpoint of each of the 6 subsections of the cross section delineated by the depth measurements and at approximately 0.6 depth (as illustrated in Figure 27), as the mean velocity in a vertical profile can be approximated by

the velocity at 0.6 depth in shallow depths (Genç *et al*., 2015). Each velocity measurement is therefore assumed to be representative of the average velocity of the corresponding subsection.

Finally, the data was processed using the trapezoidal method to calculate the surface area of each subsection. The total discharge of Nyarutovu was calculated by summing the flow of each subsection, each flow being calculated as the velocity of the subsection multiplied by its area (See Figure 27).

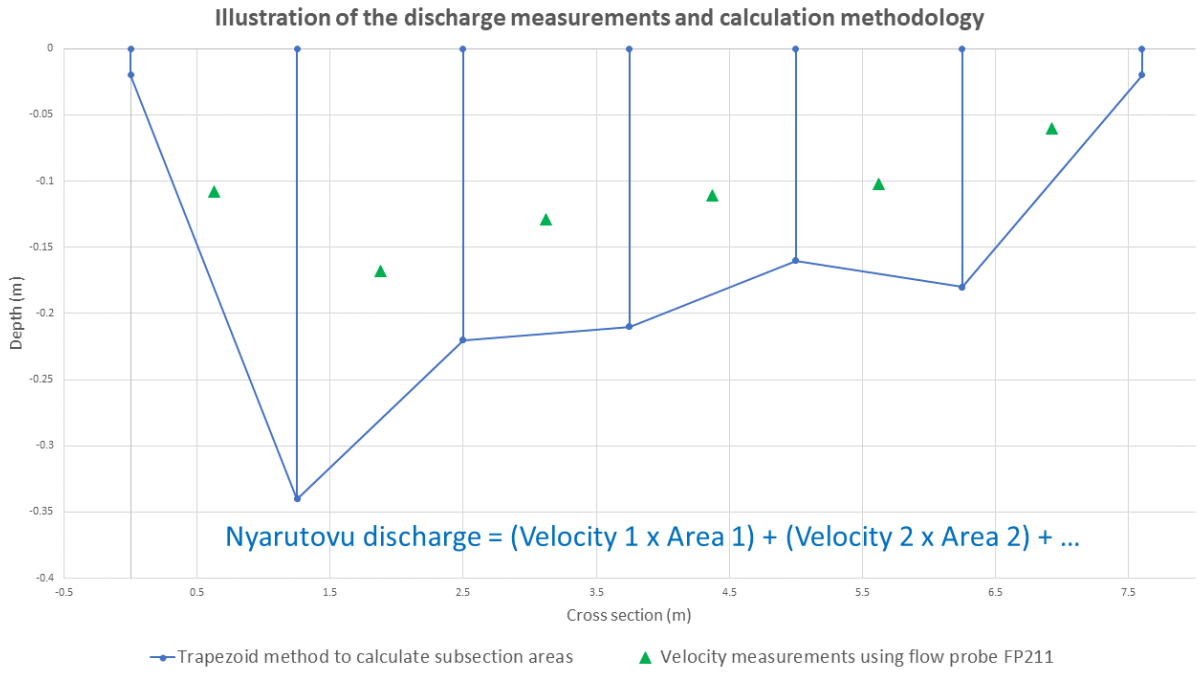

Figure 27. Diagram illustrating the discharge measurements methodology with the flow probe and the calculation of discharge using the trapezoidal method.

4.8.2.1.2. Float method

Float method is performed using a float (often a tennis ball, or a partially-filled water bottle). Firstly, the surface velocity (V_s) is calculated measuring the time (t) it takes the float to cover a certain distance (L) as shown in Figure 28. We thus have V_s = L/t. This process is repeated several times to obtain an average surface velocity. If possible, float velocity measurements are done at several points along the watercourse to try to be as representative as possible of the river as a whole.

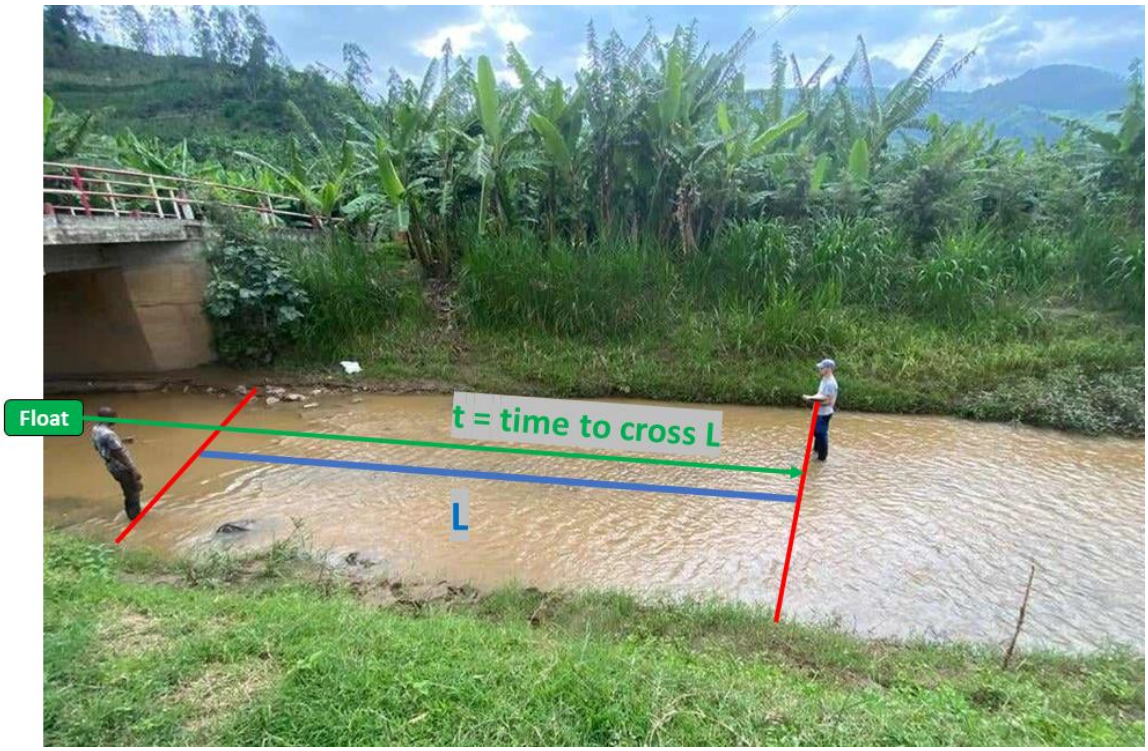

Figure 28. Diagram illustrating the float method for measuring discharge (Picture by Déogratias Nahayo, 2023).

Then, the average stream velocity (V_a) is estimated to be 0.8 times the surface velocity (V_s). The coefficient of 0.8 relating surface velocity to average velocity has been determined to hold true for shallow depths, where the hydraulic radius (Rh) is within the range of 0 to 1 m, after which it increases linearly to 0.9 for a Rh of 5 m (Hauet *et al.*, 2018). In our case, the Rh corresponding to the bankfull discharge is about 1.7 m and to get an idea, when the maximum water depth is 0.95 m, the Rh is 0.7 m. Given that the maximum water depth during float gauging did not exceed 1m, we can confidently use this coefficient of 0.8.

Finally, to calculate the discharge, the average velocity is multiplied by the cross section area which is measured and calculated using the trapezoid method explained above. The difference with the flow probe method is that a single velocity is used for the whole cross section.

4.8.2.2. Establishment of the rating curve

The substrate of the Nyarutovu river is quite fine (clay loam with some coarser gravels, as visible in Figure 29), which can lead to frequent changes in the riverbed morphology. If the riverbed changes, a new rating curve must be established based on discharge observations taken after the modifications. Consequently, discharge measurements conducted after the

flood of May 3, 2023, including those carried out during the study stay in Rwanda, have not been retained to try to work as much as possible on a period when the bed was stable.

Figure 29. Picture of Nyarutovu river just a few meters upstream of the hydrometric station. The river substrate (clay loam with some coarser gravels) is clearly visible (Picture by Victor De Clerck, 2023).

Establishing the rating curve was laborious, as the water level at the staff gauge was not recorded during the discharge measurements. The available data used in attempting to construct a rating curve consisted of: (1) the manual observations of the water level at the staff gauge, and (2) the water level time series calculated from the Diver and BaroDiver measurements.

It should first be noted that the discharge data of April 4, 2023 has been excluded as an outlier. On this date, the overtopping of Mukungwa river stopped the water flow of Nyarutovu river (Déogratias Nahayo, personal communication). As a result, the water level measured was not due to upstream contribution and the velocity was significantly reduced (see Figure 30).

Figure 30. From left to right: 1) Picture showing the overtopping of Mukungwa river at the confluence with Nyarutovu, and 2) a picture showing the effect of the overtopping of Mukungwa on Nyarutovu: a high water level for virtually no flow.

Manual observations of water level on the staff gauge are realized by a local villager, who takes 3 measurements per day (07:00, 12:00 and 17:00). Unfortunately, this data is not very reliable due to several factors. Firstly, the villager does not consistently note the precise time of measurement, sometimes arriving at different times than scheduled (e.g. 14:00 instead of 17:00). Secondly, there is a lack of understanding regarding the measurement process, leading to occasional misinterpretations, such as recording negative values on the gauge. Moreover, he can sometimes "guess the measurement from the weather", or simply does not take the measurement at all. In addition, observations taken at 12:00 on the day of the discharge measurements do not provide suitable data for constructing a rating curve and the May 03, 2023 observation constituting the upper limit of the rating curve is not available (Figure 31). Therefore, the option of using manual observations was also discarded.

Date	Manual observations on staff gauge at 12:00 [m]	Discharge [m³/s]
20-10-21	No data	0.48
21-01-22	-0.5	0.18
01-03-22	0.15	0.66
05-09-22	No data	1.12
17-09-22	No data	0.27
06-10-22	0	3.41
22-11-22	0.53	2.66
29-11-22	0.355	0.89
01-12-22	0.2	0.52
09-12-22	0.22	1.19
26-12-22	0.32	1.03
09-01-23	0.19	0.64
30-01-23	0.09	0.85
10-02-23	0.07	0.68
03-03-23	No data	0.58
10-03-23	No data	0.61
30-03-23	No data	0.49
18-04-23	No data	2.59
03-05-23	No data	7.47

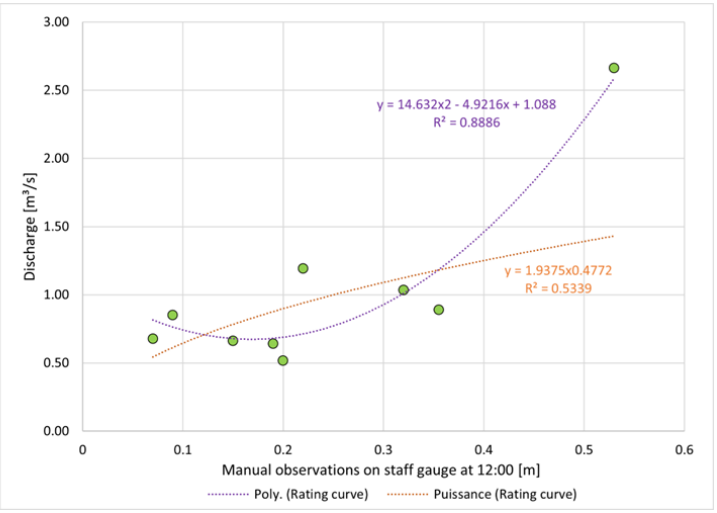

Figure 31. From left to right: 1) data of manual observations on the staff gauge at 12:00 on discharge measurement days and the corresponding discharges, and 2) an attempt to establish a rating curve with available manual observation data. The colors in the table and on the graph correspond to the same data.

Next, the water levels measured at the Diver were considered in an attempt to establish a rating curve. A major uncertainty lies in the time of discharge measurements, which was not provided. Consequently, the water level used was the average water level between 8:00 and 12:00, as discharge measurements typically occurred within this timeframe.

As depicted in Figure 32, for several discharge measurements, no water level was recorded at the Diver. This could be attributed to the discharge being too low to reach the Diver level, causing the water to flow beneath it. However, as an example, on October 6, 2022, no water level was measured at the Diver despite a relatively large discharge being recorded (3.41 m^3/s). This is probably due to an error in encoding the discharge measurement date, which is confirmed by the fact that the manual observer also recorded 0 (at the staff gauge) on October 6, 2022.

As explained above, water levels below 0.02 m have been disregarded as they may be attributed to the inaccuracy of the probes.

The data for November 11, 2022 were also discarded due to their apparent outlier status compared to the rest of the dataset (see Figure 32). Given the working hypotheses (average between 08:00 and 12:00, uncertain dates), it appears prudent to exclude this data point from consideration for the rating curve.

Finally, a rating curve was plotted with the remaining data (see Figure 32). For this data, all discharge measurements were performed using the float method, except for May 3, 2023 when the flow probe method was used.

Fortunately, data for May 3, 2023 are available, providing a fairly high upper limit for the rating curve. However, since this measurement was taken under flood conditions, the discharge measurements taken is probably not very accurate. Additionally, it's important to note that for May 3, 2023, instead of using the average water level between 08:00 and 12:00, the last measurement before the Diver was removed from the water (08:15) was selected. This choice was made because it is the water level most likely to be associated with the discharge measurement taken around the same time.

Date	08:00 - 12:00 average water level at Diver [m]	Discharge [m³/s]
20-10-21	< 0	0.48
21-01-22	< 0.02	0.18
01-03-22	< 0.02	0.66
05-09-22	< 0	1.12
17-09-22	< 0	0.27
06-10-22	< 0	3.41
22-11-22	0.30	2.66
29-11-22	0.11	0.89
01-12-22	0.05	0.52
09-12-22	< 0	1.19
26-12-22	0.071	1.03
09-01-23	< 0	0.64
30-01-23	< 0	0.85
10-02-23	< 0	0.68
03-03-23	< 0	0.58
10-03-23	< 0	0.61
30-03-23	< 0	0.49
18-04-23	0.56	2.59
03-05-23	1.81	7.47

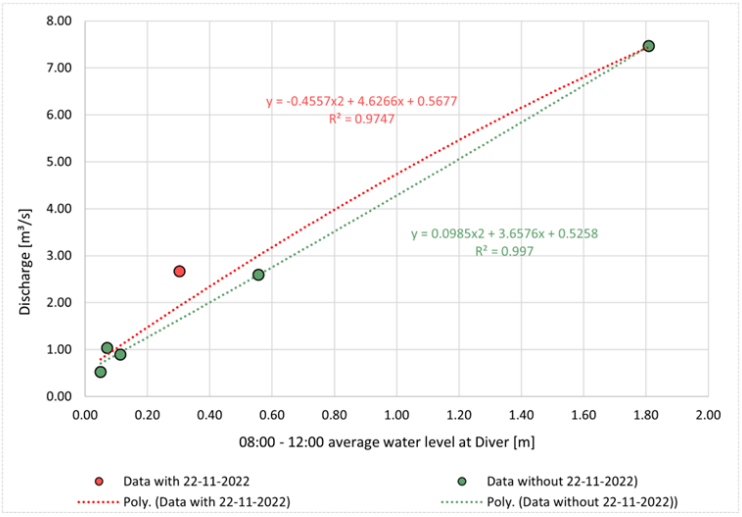

Figure 32. From left to right: 1) data of 08:00 – 12:00 average water level at Diver and the corresponding discharges, and 2) Rating curves established with the November 22, 2022 data (red) and without the November 22, 2022 data (green). The colors in the table and on the graph correspond to the same data.

The final rating curve used has the following equation:

$$\text{Discharge} = 0.0985 * \text{WL}^2 + 3.6576 * \text{WL} + 0.5258$$

This equation means that the estimated discharge when the water level is at the Diver level is 0.5228 m³/s. Below this value, it is uncertain whether the flow is zero or if there is a flow that is simply not measured by the Diver.

As already mentioned, the bed of the Nyarutovu river is likely to change frequently due to its substrate. Nevertheless, it seems reasonable to assume that the average bed level has remained fairly stable over the period when flow measurements have been made (i.e. from October 2022 to May 2023). While the established rating curve is subject to uncertainties, it nonetheless appears to be sufficiently robust for use and represents the best available solution.

4.8.3. Calculation of the discharge time series

The discharge data was calculated from the rating curve equation established.

Extrapolations cannot be dispensed when measured water levels are below or above the limits of the data used to construct the rating curve. As long as the geometry of the river bed does not change with the height considered, it is possible to extend the established rating curve but as soon as the height considered corresponds to an overtopping, such extensions no

longer make much sense (Cosandey & Robinson, 2000). The Diver sits approximately 20 cm above the maximum depth of the river and GNSS measurements reveal that the Nyarutovu bank height is just over 2.7 m. According to these data, water levels exceeding 2.5 m at the Diver correspond to the onset of overtopping, providing a rough estimate of the water level threshold for overtopping. This corresponds a discharge of about 10.28 m^3/s.

The measured water levels exceeding the upper limits of the rating curve all occurred on May 3, 2023 with some water levels exceeding the threshold for overtopping (see Figure 33). Therefore peak flows measured on May 3, 2023 exceeding 10.28 m^3/s (water level of 2.5 m) should not be considered for the hydrologic modeling as they may be distorted.

In addition, discharge data for April 4, 2023 must also be disregarded due to the overtopping of the Mukungwa river situation explained above.

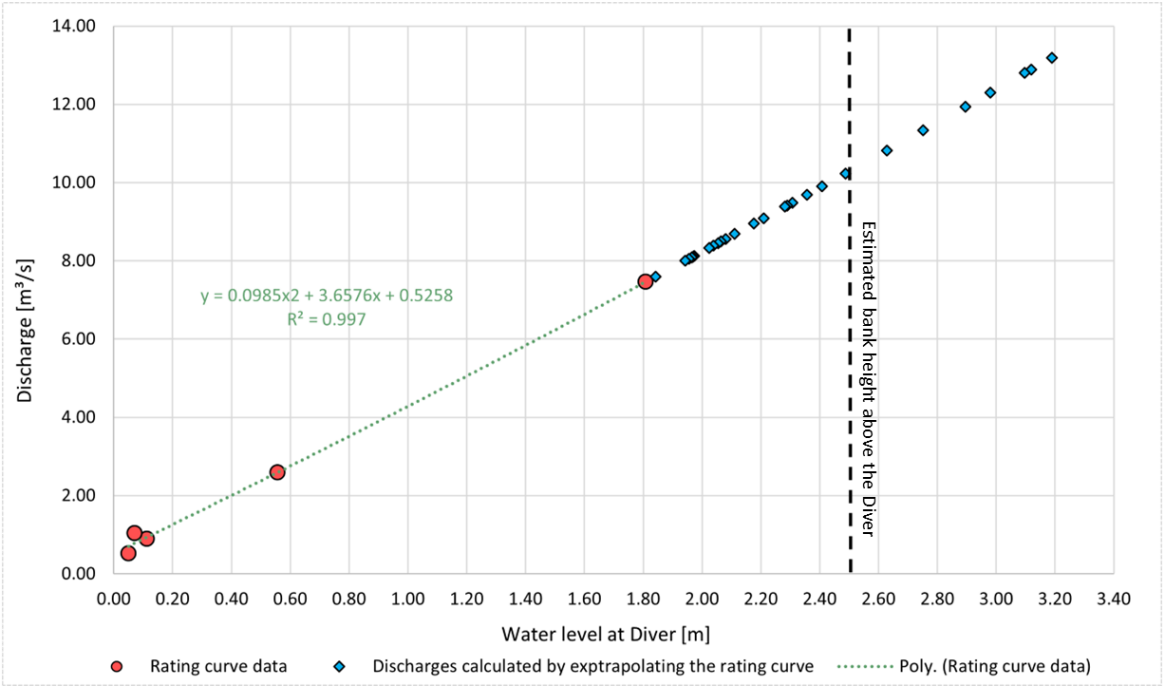

Figure 33. Discharges calculated by extrapolating the rating curve in relation to the threshold for overtopping and the rating curve.

Given that precipitation data are available from January 2023 to May 2023, only discharge data corresponding to this same period are of interest. On May 3, 2023, the Nyarutovu Diver was taken out of the water at 08:00 to download the data and was only placed back into the river on May 20, 2023. And finally, the data from the BaroDiver are no longer available starting from May 11, 2023. In the end, this results in a continuous precipitation and discharge time series extending from January 1, 2023 to May 3, 2023.

4.9. Hydrologic modeling

Hydrologic modeling is used to evaluate the response of an hydrologic unit (watershed) to precipitation. It can be used for plenty of applications such as monitoring of water supply, flood forecasting, demarcation of flood-prone areas, and so on (Athira *et al*., 2023). Hydrologic modeling requires a large set of spatial and temporal data such as precipitation, discharge, LULC, elevation, soil texture data. Two types of modeling exist: (1) event and (2) continuous. An event-based model simulates a single storm which means it can only simulate the response (e.g. quantity of surface runoff, peak discharge, …) of the watershed modeled during and after a precipitation event. On the other hand, continuous models are designed to simulate the behavior of the watershed for longer periods (days to years). Therefore continuous models must be able to simulate the response during but also between rainfall events (Chu & Steinman, 2009; USACE, 2023). For this study, we will focus on event modeling.

4.9.1. Hydrograph components definitions

Before going into the details of hydrologic modeling, it is crucial to establish clears definitions of the hydrograph timing components (Figure 34) as these terms will be used in subsequent discussions.

The **lag time** (L) is the time interval between the center of mass of the excess precipitation and the peak discharge (Fang *et al*., 2005; USDA, 2010)

The **time to peak** (T_p), also called time of rise, is the time interval between the start of the rise and the peak discharge (Fang *et al*., 2005; Langridge *et al*. 2020; USDA, 2010).

The **time of concentration** (T_c) is the time required for runoff to travel from the hydraulically most distant point in the watershed to the outlet. Note that this point is not necessarily the point with the longest flow distance to the outlet (USDA, 2010).

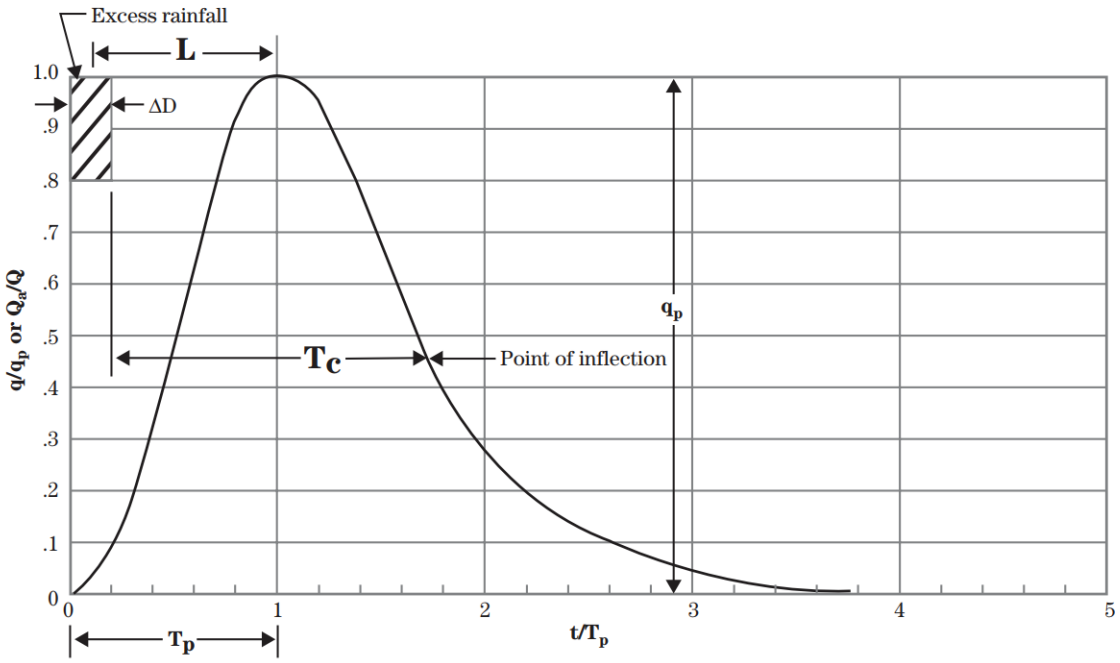

Figure 34. Hydrograph timing components (USDA, 2010)

4.9.2. Events selection and separation

A selection of events was made to retain only floods of more than 1 m^3/s, as this work focuses on understanding flooding in the Nyarutovu watershed. Hydrologic modeling of events requires the separation of the event hydrograph into two components: (1) the baseflow, which is the ground water contribution to the stream and (2) the event flow, which is the direct surface runoff produced by the event (Figure 35) . This process is called “baseflow separation”. There is not standard method and baseflow separation often remains very difficult (Blume *et al*., 2007; Duncan, 2019). Graphical methods exist to separate the baseflow as shown in Figure 36. These methods are based on the simplifying assumption that the increase in flow during an event is just due to the event rainfall running off the catchment (Duncan, 2019). The “constant baseflow” method assumes that the baseflow is equal to the flow measured at the point of rise. This baseflow then remains constant throughout the event (see point 1 in Figure 36). This method was chosen for this study as it is very often used and easy to implement (Raghunath, 2006). Of course, the baseflow is thus approximated, and it is certain that the actual baseflow follows a pattern more like the one illustrated in Figure 35.

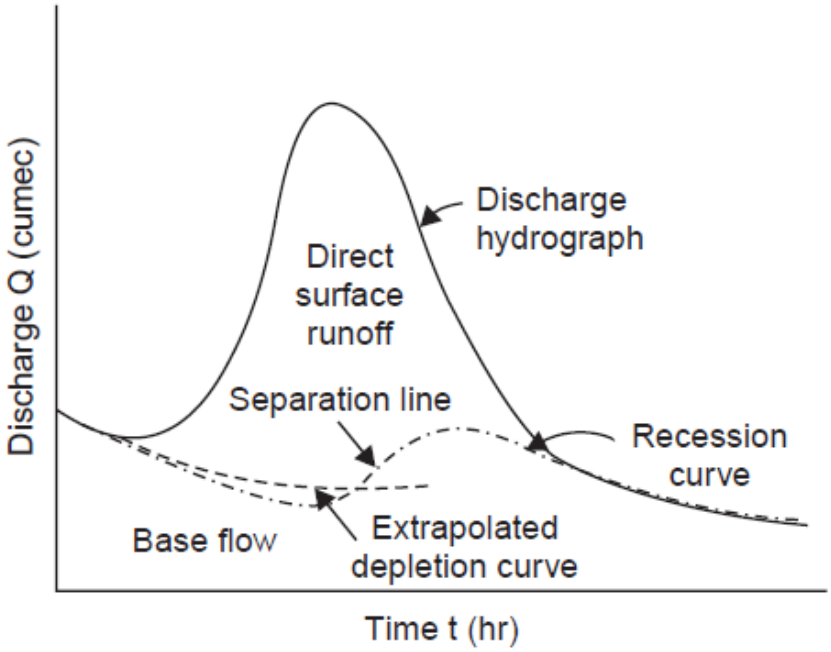

Figure 35. Actual separation between the baseflow and the direct surface runoff in a hydrograph (Raghunath, 2006).

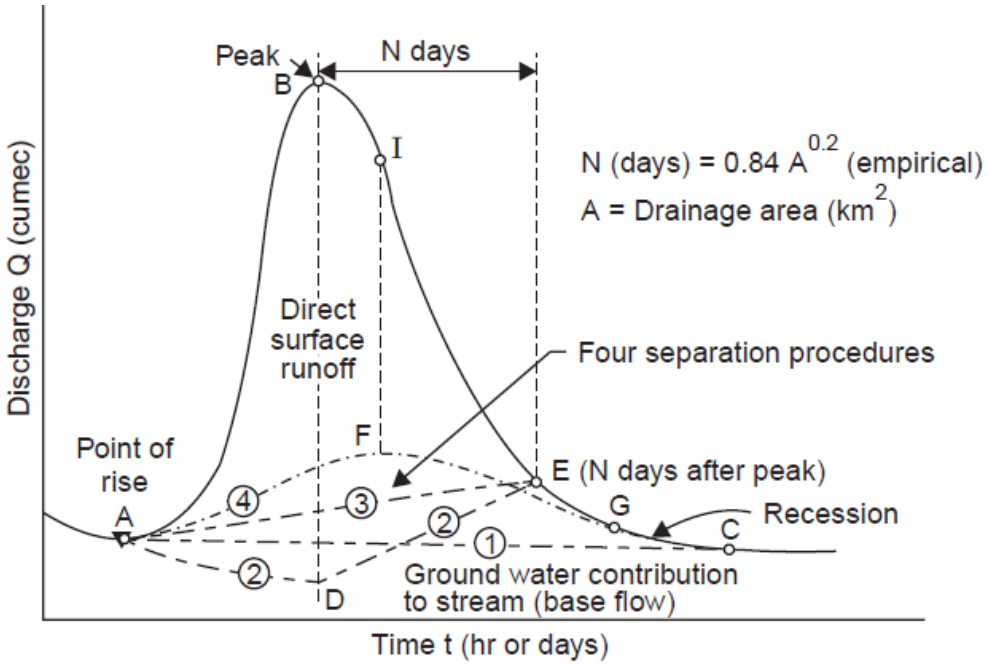

Figure 36. Illustration of 4 graphical baseflow separation methods, including the "constant baseflow" method represented in the figure by the number "1" (Raghunath, 2006).

The events including more than one peak (e.g. complex hydrographs) have been resolved into simple hydrographs by extending the recession curves as shown in Figure 37. Exponential function for the recession curves were found in Excel. The precipitation have also been divided to single events. This treatment was carried out because some of the infiltration methods that

will be used for hydrologic modeling can only be applied for single event simulations (USACE, 2023). In addition, Raghunath (2006) and McEnroe et *al.* (2016) state that for floods analysis, a single peaked hydrograph is preferred.

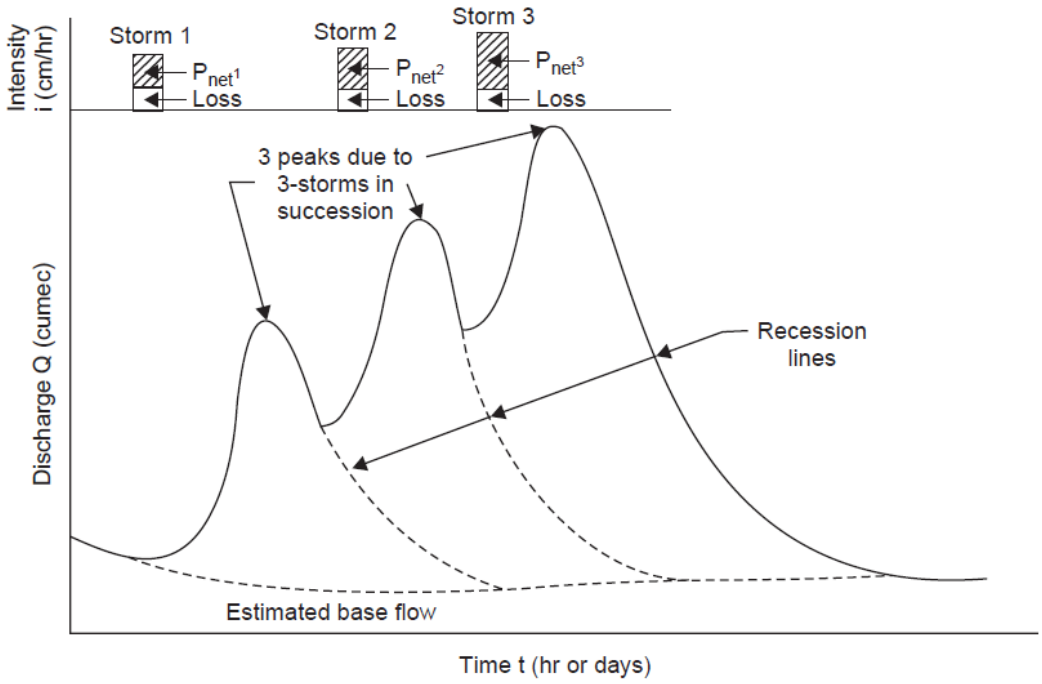

Figure 37. Illustration of the method for converting a complex hydrograph into several single peaked hydrographs by extending recession curves (Raghunath, 2006).

The separation of events is illustrated in Figures 38 to 47, with comments provided on the specific methodology used for each event where necessary.

For the March 31, 2023 event separation, the baseflow was assumed to be equal to the last discharge measured before no more flow is measured between 11:30 and 12:15 (Figure 38). The hypothesis here is that the storm (with precipitation intensity reaching 52.85 mm/h) was accompanied by a significant local depression which, according to the water level calculation methodology explained earlier, could have compensated for the additional water pressure measured at the Diver compared to the BaroDiver and fictitiously masked the water level.

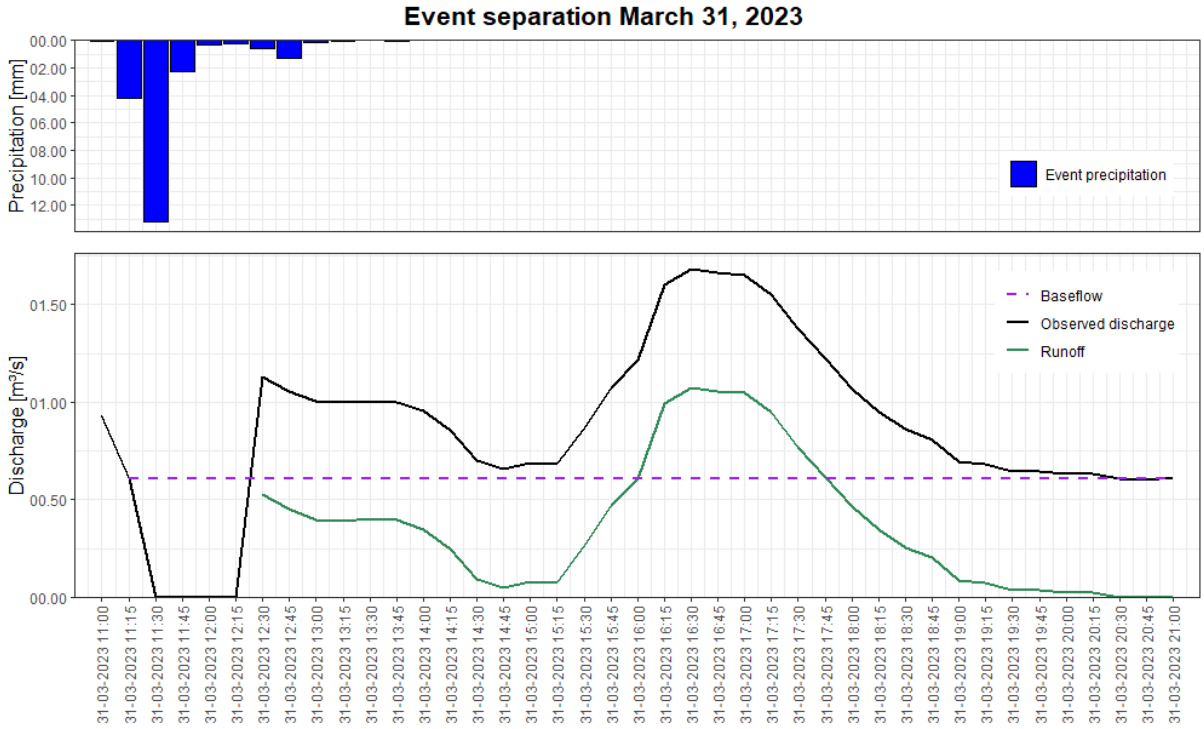

Figure 38. March 31, 2023 event separation.

For the April 02-04, 2023 event separation, the extending of recession curves was applied (Figure 39).

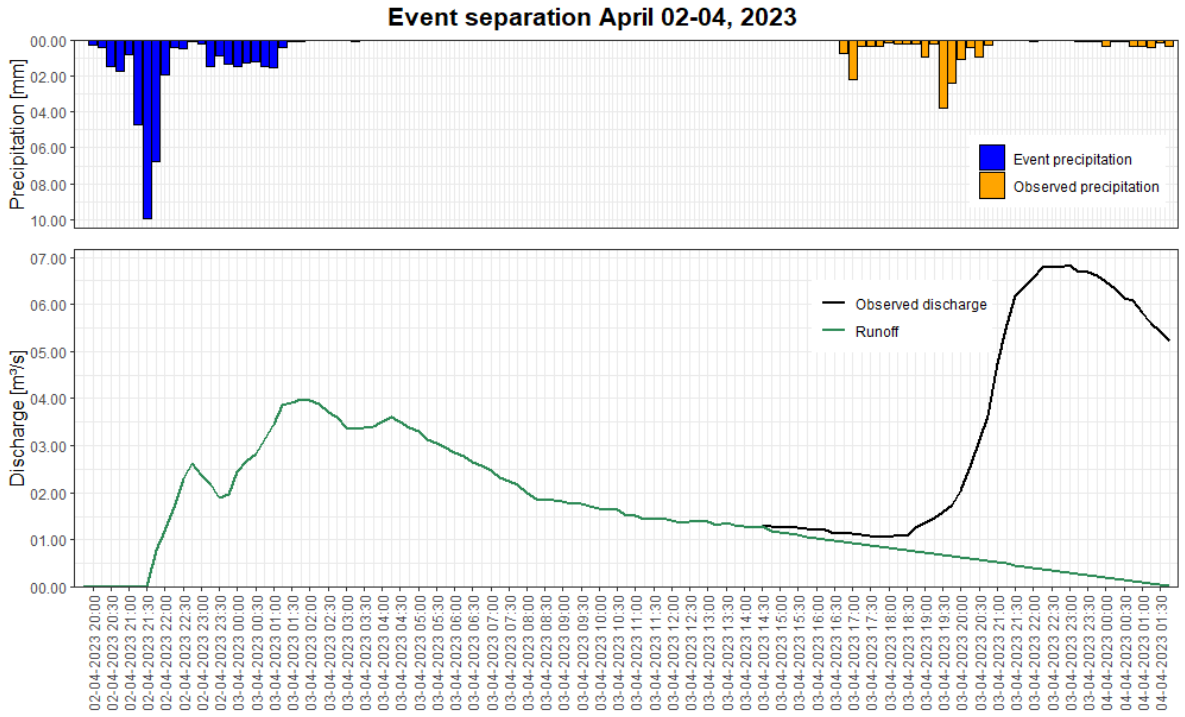

Figure 39. April 02-04, 2023 event separation.

The same consideration as for the separation of the March 31, 2023 event led to considering the last flow before nothing is measured as the baseflow for the April 15-16, 2023 event (Figure 40).

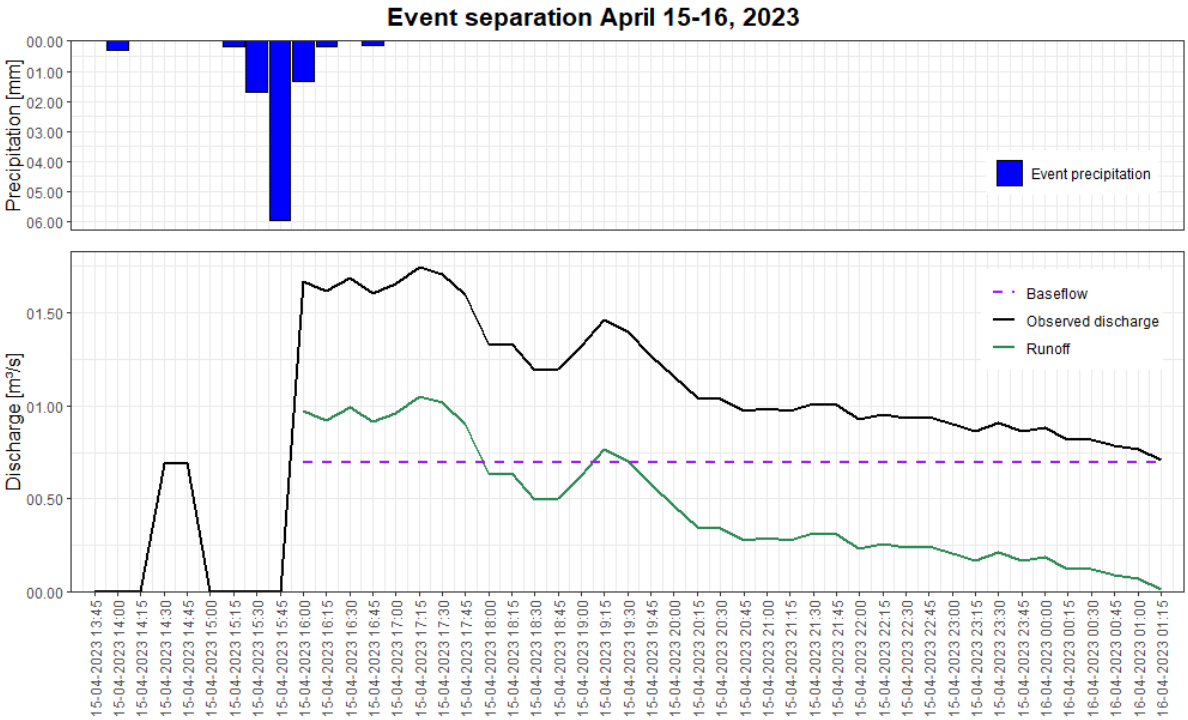

Figure 40. April 15-16, 2023 event separation.

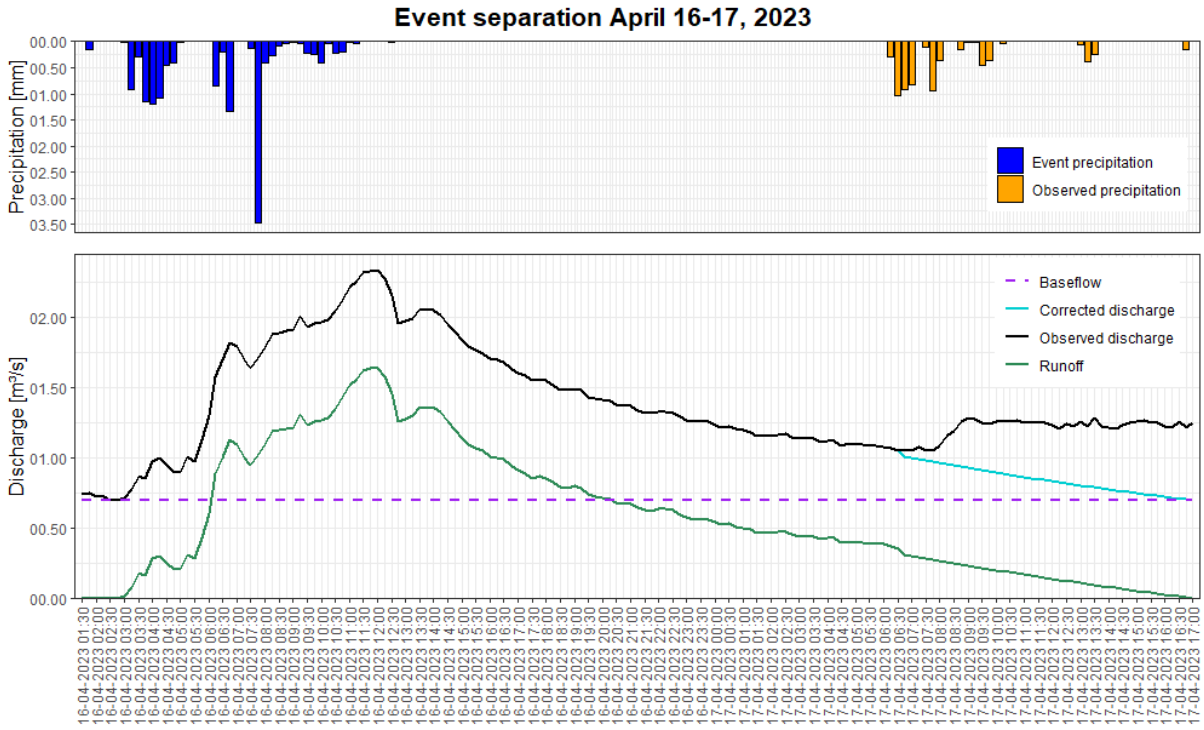

Figure 41. April 16-17, 2023 event separation.

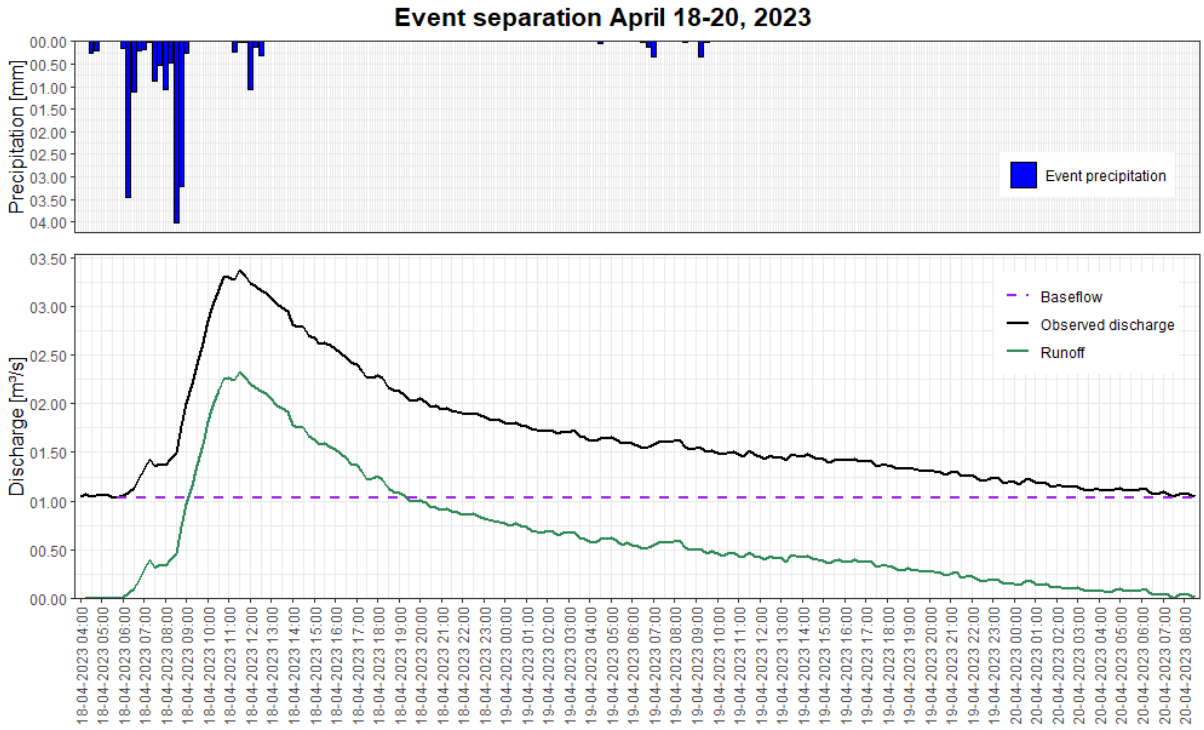

Figure 42. April 18-20, 2023 event separation.

The April 23-24, 2023 complex hydrograph was resloved into two single peaked hydrographs (Figure 43). The following steps were followed: (1) extending the recession curve to separate the events from the next event, resulting in the corrected discharge curve, (2) separation of the baseflow and the runoff, (3) extension of the recession curve of the event 1, (4) determination of the runoff of event 2 by the difference between the runoff and the event 1 runoff, and (5) separation of the precipitation for each event.

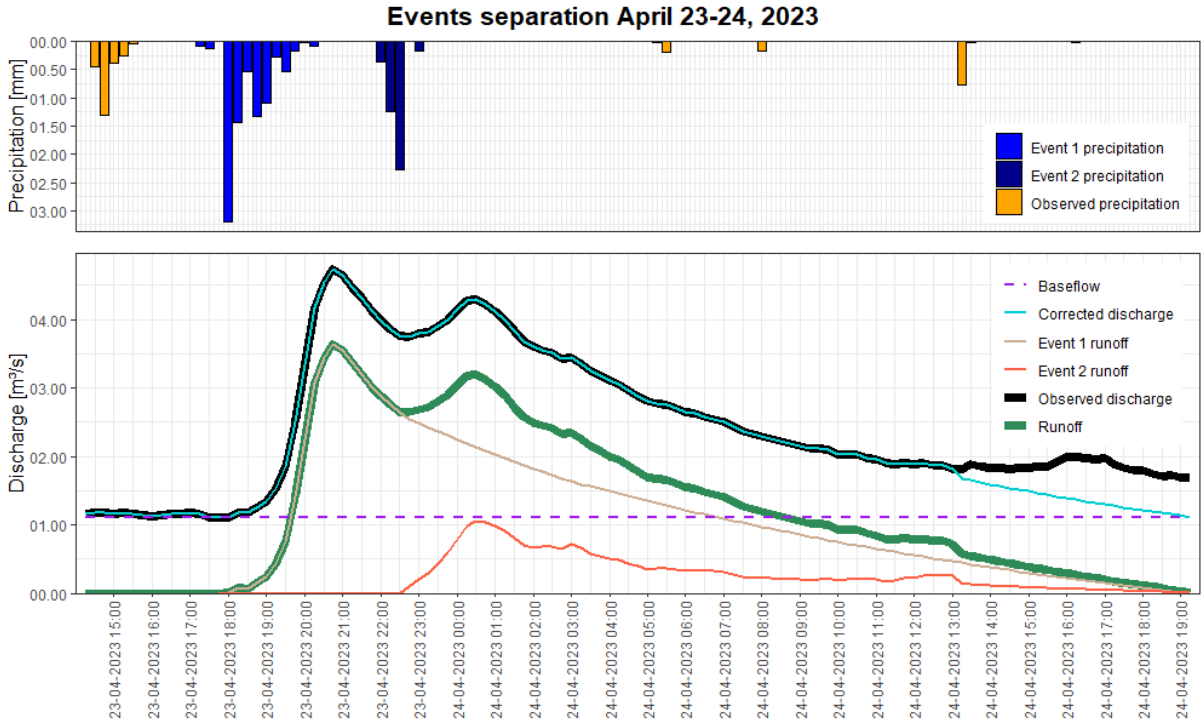

Figure 43. April 23-24, 2023 event separation.

For the Aprill 28-29, 2023 events separation, the complex hydrograph was also resolved into single peaked hydrographs (Figure 44). Steps were the following: (1) identification of the baseflow and the corresponding runoff, (2) extension of the recession curve of the event 1, (3) determination of the runoff the event 2, (4) extension of the recession curve of the event 2, and (5) separation of the precipitation for each event. The third peak, occurring on April 29, 2023 was analyzed separately (see Figure 45).

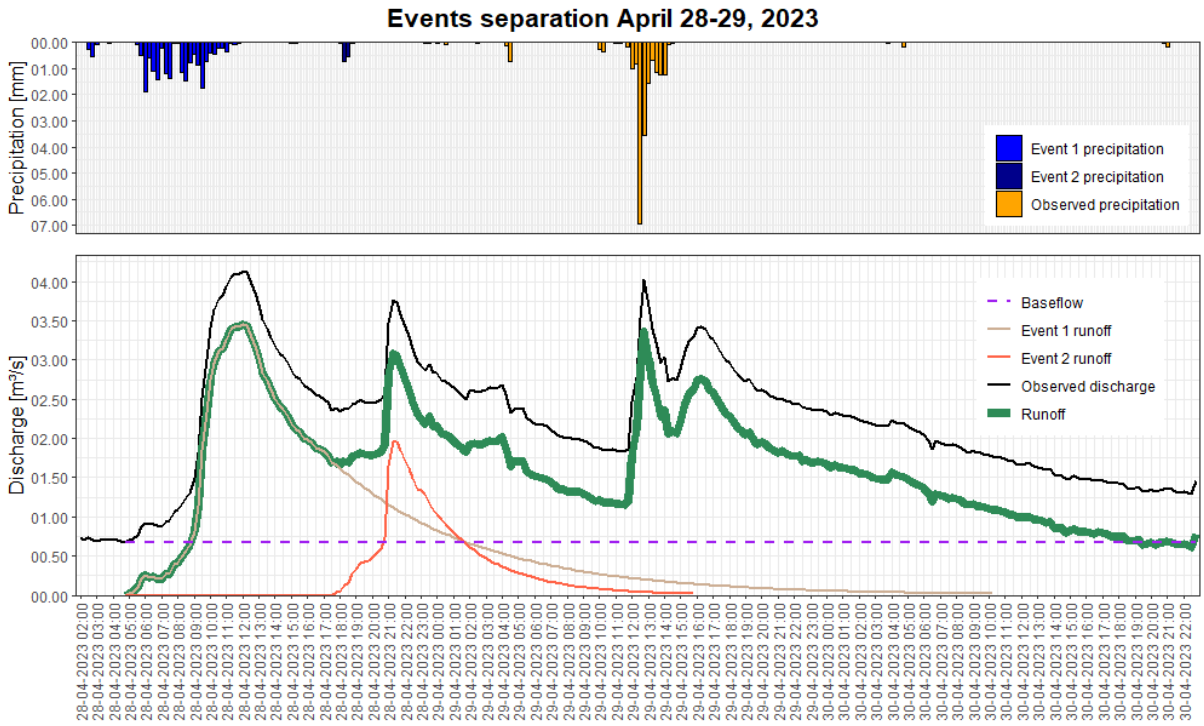

Figure 44. April 28-29, 2023 event separation.

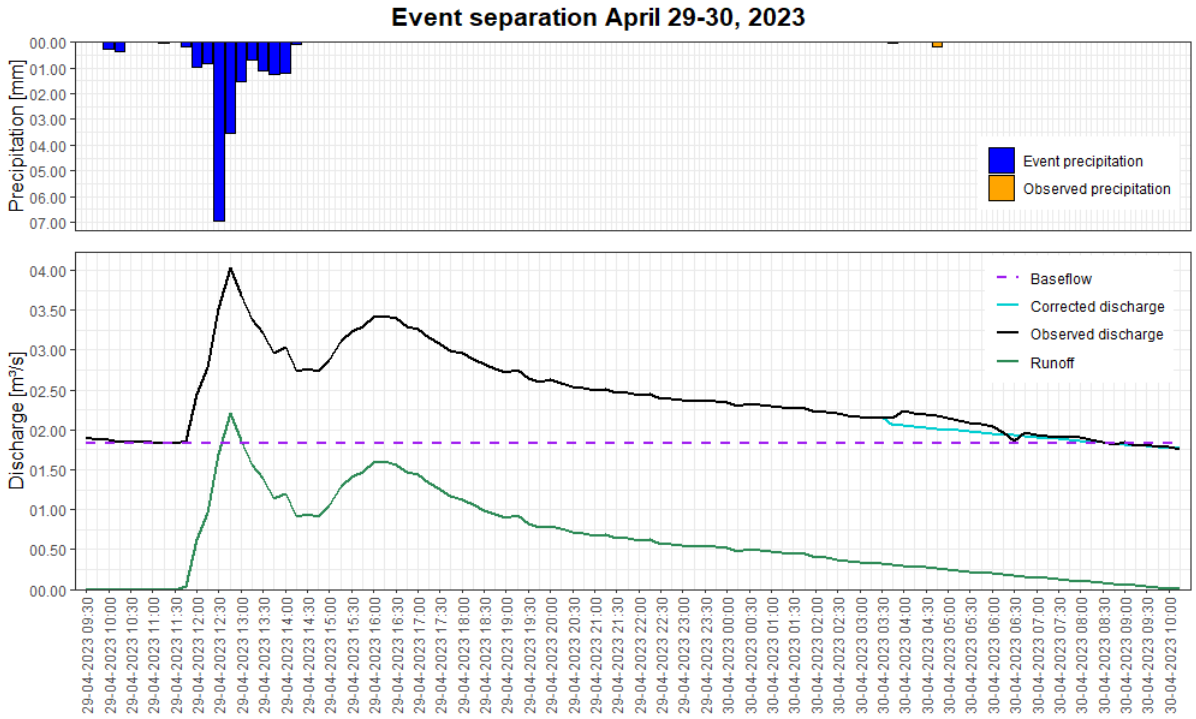

Figure 45. April 29, 2023 event separation.

For the April 30 – May 03, 2023 events separation (Figure 46), the following steps were followed: (1) separation of the baseflow and the runoff, (2) extension of the event 1 recession curve, (3) determination of the event 2 runoff and (4) extension of its recession curve.

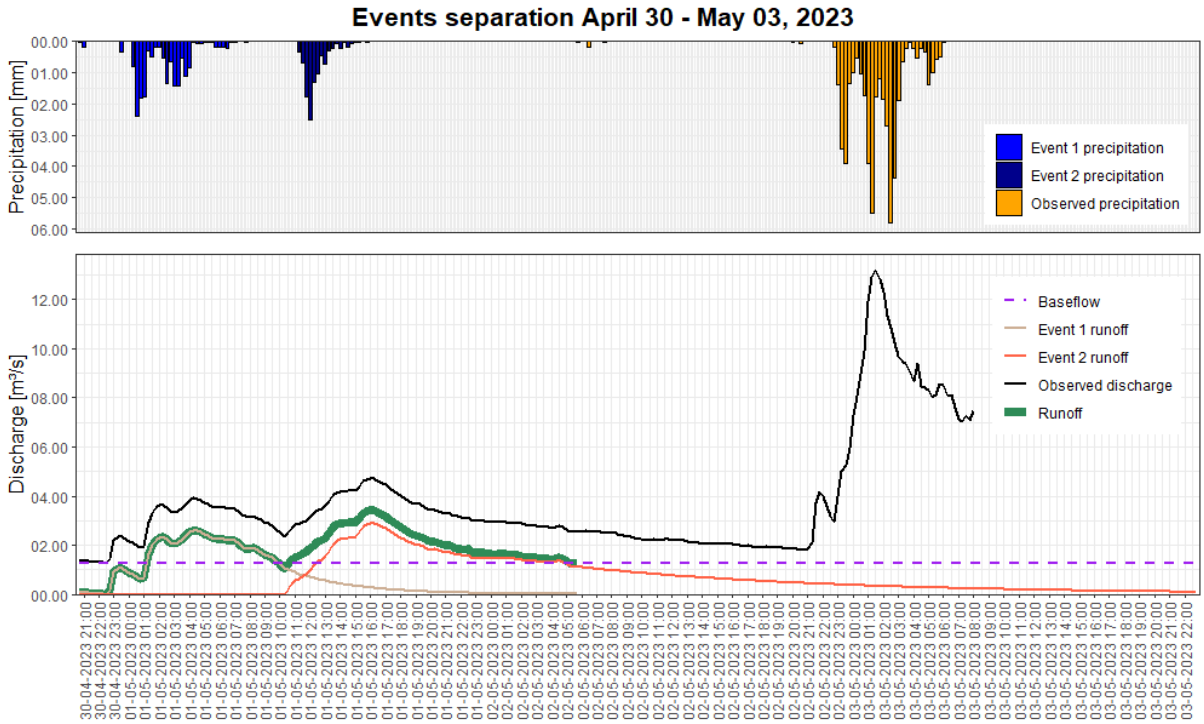

Figure 46. April 30 - May 03, 2023 events separation.

As explained before, the event of May 2 to 3, 2023 should not be fully considered for hydrologic modeling, as measured peak flows (exceeding 10.28 m^3/s) may be distorted due to the probable overtopping of river banks. No further discharge was measured after 08:00, when the Diver was taken out of the water.

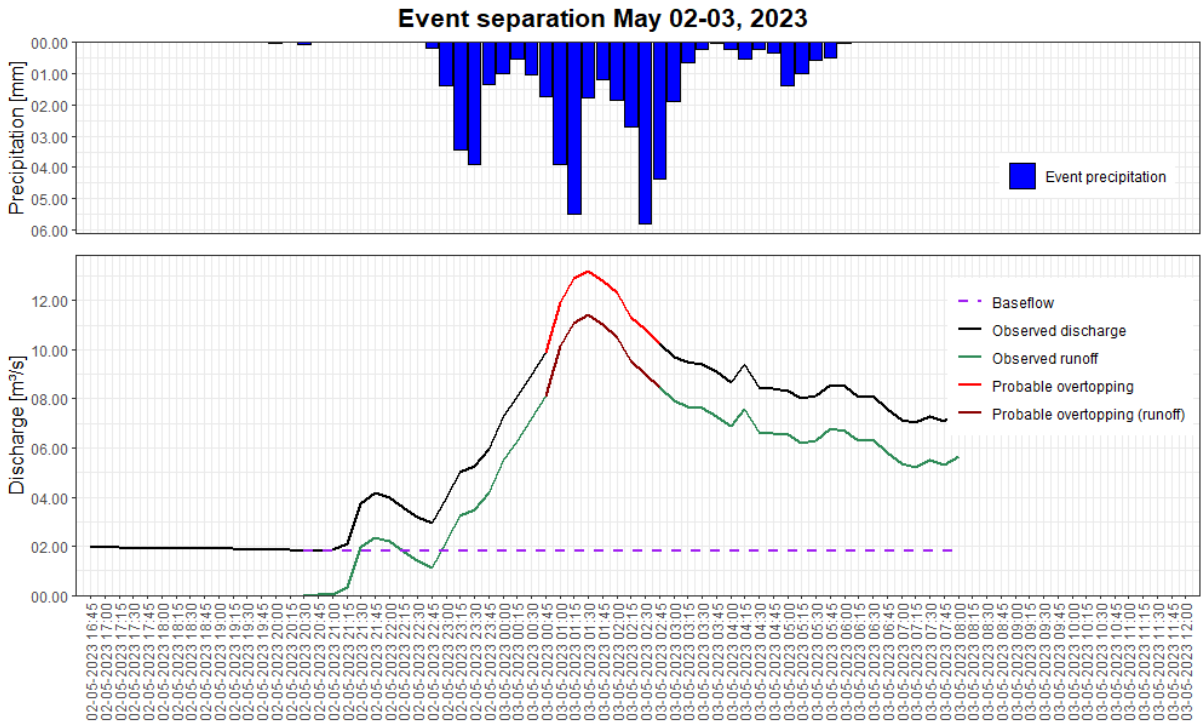

Figure 47. May 02-03, 2023 event separation.

This selection and separation of events resulted in a total of 13 events ready to be used as observation data for hydrologic modeling. The characteristics of these events are presented in the table 4. It should be noted that discharge characteristics for the May 2-3, 2023 event could not be calculated, as part of the event is probably distorted and no discharge data is available from 08:00 onwards.

Event precipitation characteristics include: total precipitation (the total amount of precipitation measured (≥ 0.1 mm/15min)), the duration (calculated taking into account precipitation ≥ 0.1 mm/15min), the maximum intensity measured and the average intensity (total precipitation over the duration of the precipitation event).

The discharge characteristics include: the runoff volume (calculated by multiplying each runoff measured by the number of seconds in 15 minutes), the runoff coefficient which is the ratio

between the runoff volume and the total volume of precipitation. Finally, the peak discharge and the time to peak as defined above. Unfortunately, it is not possible to calculate the lag time directly from the observation data, as it is the time interval between the centroid of the excess precipitation and the peak flow, but the excess precipitation is not known before the hydrological modeling. The observed lag times for each event will be calculated during calibration, as suggested by McEnroe *et al.* (2016).

	Precipitation				Discharge			
Date	**Total precipitation (mm)**	**Duration (min)**	**Max intensity (mm/h)**	**Average intensity (mm/h)**	**Runoff volume (mm)**	**Runoff coefficient**	**Peak (m^3/s)**	**Time to peak (min)**
31 March 2023	22.39	210	52.85	6.40	0.26	0.01	1.07	240
02-03 April 2023	39.69	330	39.88	7.22	3.73	0.09	3.99	240
15-16 April 2023	9.82	180	23.85	3.27	0.35	0.04	1.05	75
16-17 April 2023	13.65	555	13.90	1.48	1.88	0.14	1.64	360
18-20 April 2023	18.73	300	16.10	3.75	2.71	0.14	2.33	330
(1) - 23-24 April 2023	11.19	330	12.79	2.03	2.37	0.21	3.63	165
(2) - 23-24 April 2023	4.05	75	9.07	3.24	0.52	0.13	1.06	240
(1) - 28-29 April 2023	17.96	525	7.45	2.05	3.02	0.17	3.46	435
(2) - 28-29 April 2023	1.27	30	2.87	2.53	0.78	0.62	1.96	225
29-30 April 2023	19.00	255	27.81	4.47	1.20	0.06	2.20	75
30 April - 02 May 2023	17.13	585	9.49	1.76	2.02	0.12	2.62	465
01-03 May 2023	9.77	210	10.04	2.79	3.97	0.41	2.91	360
02-03 May 2023	49.16	435	23.24	6.78	/	/	/	/

Table 4. Precipitation and discharge characteristics of the 13 selected events.

4.9.3. HEC-HMS

HEC-HMS – Hydrologic Engineering Center – Hydrologic Modeling System is a physically based semi-distributed hydrologic model that has been developed by the Hydrologic Engineering Center of the US Army Corps of Engineers. A semi-distributed model is a model in which the study area can be divided into smaller units (e.g., watershed divided into subbasins) reacting uniformly to precipitation. In this approach, parameters are defined for each subbasin (Halwatura & Najim, 2013). This subdivision was not performed in this case in order to simplify the model as much as possible.

HEC-HMS was selected for its open-source nature and its established reliability in assessing flash flood risks, as demonstrated by Halwatura & Najim (2013) and Icyimpaye *et al*. (2022). Additionally, Xin *et al*. (2019) conducted a comparative study of HEC-HMS against four other

widely used hydrologic models for simulating flash floods in small catchments of a hilly area in China. Their findings indicated that HEC-HMS outperformed the other models, proving its suitability for flash flood simulation. Furthermore, Haddad (2022) successfully utilized HEC-HMS to model extreme rainfall-runoff events in northern Algeria, while Zema *et al*. (2017) applied it to a southern Italian watershed with an average slope steepness of 28.6%. The applicability of the model was also confirmed by Nandalal & Ratnayake (2016), who demonstrated its effectiveness in modeling rainfall-runoff events in Sri Lanka.

The two main components of the HEC-HMS model are: (1) the "Loss Method", which is used to describe the losses of precipitation, due mainly to infiltration and to compute the excess precipitation for each time interval in the modeling process, and (2) the "Transform Method" which transforms the excess precipitation at the watershed into a hydrograph at the outlet (Sahu *et al*., 2023).

4.9.3.1. Loss Methods

HEC-HMS offers a total of 11 loss methods. Selecting an appropriate loss method is crucial when setting up an HEC-HMS model. This is particularly challenging in regions with environmental conditions that differ from those where the loss methods were initially developed. In such contexts, referring to previous studies where the models have been successfully applied and validated can provide valuable guidance (Zema *et al*., 2016). However, the most suitable loss method differs from one catchment to another and the model simulation results have been showed to be location specific (Prabaswara & Wickramaarachchi, 2022).

For this work, 3 methods were selected, namely: (1) the Soil Conservation Service – Curve Number (SCS-CN), (2) the Initial and Constant (IC), and (3) the Green and Ampt (GA) methods. These methods have been recommended for event-based precipitation-runoff simulations (Prabaswara & Wickramaarachchi, 2022; Zema *et al*., 2017).

The SCS-CN method is mature, simple to use, and has been successfully applied in thousands of studies (USACE, 2023; Zema *et al*., 2017). Moreover, SCS-CN is the only one to fully take LULC into account and one goal of the LAFHAZAV (ARES) project is to better understand the

influence of LULC changes on precipitation-runoff relation. However, Halwatura & Najim (2013) found that SCS-CN did not perform well in a tropical catchment.

IC is also a mature, widely used method which is accessible and need few parameters (USACE, 2023; Zema *et al.*, 2017).

Finally, the Green and Ampt method is more complex, but is physically based and has shown good results in some studies and is generally able to appropriately represent infiltration processes (Kazezyılmaz-Alhan *et al.*, 2021; Sardoii *et al.*, 2012; Tügel *et al.*, 2022).

Below is a description of the three methods and their parameter estimates for HEC-HMS simulations.

4.9.3.1.1. Soil Conservation Service – Curve Number (SCS-CN) method

The SCS-CN method is based on the following hypothesis:

$$\frac{F_a}{S} = \frac{P_e}{P - I_a}$$

Where F_a is the infiltrated part of the total precipitation, S is the potential maximum retention which is a measure of the ability of a watershed to abstract and retain precipitation. P_e is the precipitation excess accumulation at time t, P is the total precipitation and I_a is the initial abstraction (Sahu *et al.*, 2023).

Since $P = P_e + I_a + F_a$, the method expresses the precipitation excess (P_e) as following (see Appendix 5 for calculations):

$$P_e = \frac{(P - I_a)^2}{(P - I_a) + S}$$

An empirical relationship between I_a and S has been developed by the SCS:

$$I_a = 0.2\,S$$

Thanks to this relationship we can reformulate the previous equation in this way:

$$P_e = \frac{(P - 0.2\,S)^2}{(P + 0.8\,S)}$$

The potential maximum retention (S) parameter is calculated from an intermediate parameter, the Curve Number (CN):

$$S = \frac{25400 - 254 * CN}{CN} \text{ (mm) or } S = \frac{1000}{CN} - 10 \text{ (in)}$$

The formula using metric units is preferred; however, some empirical formulas require the calculation of S in inches. The CN depends on the watershed characteristics including soil textures, LULC, antecedent moisture conditions (AMC). It ranges from 30 for very permeable soil to 100 for a water body (completely impervious).

Since the Nyarutovu subbasin is not uniform and contains several LULC, a composite CN had to be calculated using a GIS process based on this formula:

$$CN_{composite} = \frac{\sum A_i * CN_i}{\sum A_i}$$

Where A_i and CN_i are respectively the area and the CN of the subdivision i (USACE, 2023).

The GIS process consisted of using the LULC map and to assign a CN to each LULC by referring to tables provided by USDA (1986) in their technical release 55 (TR-55) (see Appendices 6 to 9). These tables allow for the estimation of the CN based on the LULC, its conditions, and the hydrologic soil group (HSG) of the study area. The HSG ranges from A to D, with group A having low runoff potential and high infiltration rates, and group D having high runoff potential and low infiltration rates. The HSG of Nyarutovu subbasin was considered as group D (see Figure 48) as soils in Nyarutovu are mainly composed of clay loam.

HSG	*Soil textures*
A	Sand, loamy sand, or sandy loam
B	Silt loam or loam
C	Sandy clay loam
D	Clay loam, silty clay loam, sandy clay, silty clay, or clay

Figure 48. Classification of hydrologic soil groups in relation to the soil textures (USDA, 1986 based on Brakensiek & Rawls, 1983)

The CN were assigned as described in Table 5. These values are similar to those found by Uwizeyimana *et al*. (2019) for a little watershed in southern province of Rwanda.

LULC	CN	Cover description in TR-55
Rangelands	80	Grass, fair conditions, HSG D
Trees	79	Woods, fair conditions, HSG D
Built-up areas	84	Open space, fair conditions (grass cover 50% to 75%), HSG D
Crops	81	Row crops, contoured and terraced, good conditions, HSG D

Table 5. Assigned CN to the different LULC classes of Nyarutovu watershed according to the TR-55 tables.

Finally, the composite CN is calculated in the GIS by calculating the area-weighted mean CN for the watershed. This calculation yields a CN of 80.86 for the Nyarutovu watershed.

Finally, the CN is modified for each event according to its antecedent moisture conditions (AMC). There are three antecedent moisture conditions determined by the cumulative precipitation depth during 5 days prior to the event. Several thresholds for defining these groups are established in the literature. The classical thresholds proposed by SCS were adopted (see Table 6). The thresholds for the growing season were chosen as the high levels of precipitation and moderate temperatures of tropical countries provide long growing season (Ahmad Shafuan *et al*., 2018).

	Total rain in previous 5 days	
AMC Type	Dormant Season	Growing Season
I	Less than 13 mm	Less than 36 mm
II	13–28 mm	36–53 mm
III	More than 28 mm	More than 53 mm

Table 6. Previous 5 days precipitation thresholds to define AMC (Sahu *et al*., 2023)

The $\mathrm{AMC_{II}}$ is the average annual condition while $\mathrm{AMC_{I}}$ and $\mathrm{AMC_{III}}$ represent dry and wet conditions respectively (Sahu *et al*., 2023). $\mathrm{CN_{I}}$ and $\mathrm{CN_{III}}$ values can be calculated from the $\mathrm{CN_{II}}$ value using specific formulas. Parasuraman *et al*. (2007) compared and discussed the validity of the most commonly used formulas and concluded that the formulas proposed by Hawkins *et al*. (1985) perform better than others:

$$\mathrm{CN_{I}} = \frac{\mathrm{CN_{II}}}{2.281 - 0.01281\ \mathrm{CN_{II}}}$$

$$\mathrm{CN_{III}} = \frac{\mathrm{CN_{II}}}{0.427 + 0.00573\ \mathrm{CN_{II}}}$$

The values of CN corresponding to each AMC calculated with the formulas from Hawkins *et al*. (1985) are shown in Table 7.

CN (AMC)	Value
$\mathbf{CN_I\ (AMC_I)}$	64.94
$\mathbf{CN_{II}\ (AMC_{II})}$	80.86
$\mathbf{CN_{III}\ (AMC_{III})}$	90.82

Table 7. CN values in relation to the AMC for Nyarutovu watershed.

The AMC and corresponding CN values for the 13 selected events are presented in Table 8.

Date	Previous 5 days precipitation (mm)	AMC	CN
31 March 2023	5.34	AMC_I	64.94
02-03 April 2023	26.99	AMC_I	64.94
15-16 April 2023	32.06	AMC_I	64.94
16-17 April 2023	39.25	AMC_{II}	80.86
18-20 April 2023	50.33	AMC_{II}	80.86
(1) - 23-24 April 2023	20.09	AMC_I	64.94
(2) - 23-24 April 2023	28.97	AMC_I	64.94
(1) - 28-29 April 2023	30.52	AMC_I	64.94
(2) - 28-29 April 2023	46.81	AMC_{II}	80.86
29-30 April 2023	35.22	AMC_I	64.94
30 April – 02 May 2023	53.34	AMC_{III}	90.82
01-03 May 2023	58.54	AMC_{III}	90.82
02-03 May 2023	67.06	AMC_{III}	90.82

Table 8. Previous 5 days precipitation and corresponding AMC and CN values for the 13 selected events.

4.9.3.1.2. Initial and constant (IC) method

The initial and constant (IC) method uses a hypothetical single soil layer to account for changes in moisture. Only 2 parameters are required: (1) the initial loss (I_a) which represents the part of precipitation that is intercepted or stored in the watershed and does not contribute to runoff, and (2) the maximum potential rate of precipitation loss (f_c) which is assumed to be constant throughout an event. The general equation (Figure 49) to calculate the excess precipitation (Pe) for each time interval is given by:

$$pe_t = \begin{cases} 0 & \text{if } \sum p_i < I_a \\ p_t - f_c & \text{if } \sum p_i > I_a \text{ and } p_t > f_c \\ 0 & \text{if } \sum p_i > I_a \text{ and } p_t < f_c \end{cases}$$

Figure 49. Excess precipitation formula of the initial and constant loss method (USACE, 2023).

Where p_t is the precipitation rate during the time interval t and p_i is the initial precipitation depth.

Basically, once the sum of precipitation exceeds the initial loss, runoff can begin if precipitation exceeds the infiltration rate. Otherwise, the soil is considered to absorb all the precipitation that falls on it (Prabaswara & Wickramaarachchi, 2022; USACE, 2023).

The initial loss parameter can be estimated at between 10 and 20% of total event precipitation for forested areas, with a maximum of 0.5 inches (12.7 mm). Others recommend that for forests and grasslands the initial loss varies between 0.5 and 1.5 inches (12.7 and 38.1 mm) (USACE, 1994). Zema *et al*. (2017) suggested to adopt 38.1, 25.4 and 12.7 mm for AMC_I, AMC_{II} and AMC_{III} respectively. In the same approach, values of 20, 15 and 10 % are chosen for AMC_I, AMC_{II} and AMC_{III} respectively, with a maximum of 12.7 mm (see Table 9).

The constant rate of loss parameter can be associated with the dominant soil texture of the study area. Skaggs & Khaleel (1982) published estimates of rate of loss for the different SCS soil groups. These values may be used in the absence of better information (USACE, 2023). For clay loams, loss rate ranges from 0.05 to 0.15 inches/h (1.27 to 3.81 mm/h). As an estimate, a value of 2.54 mm/h was chosen.

Date	Previous 5 days precipitation (mm)	AMC	Total precipitation (mm)	Estimated initial loss (mm)
31 March 2023	5.34	AMC_I	22.39	4.478
02-03 April 2023	26.99	AMC_I	39.69	7.938
15-16 April 2023	32.06	AMC_I	9.82	1.964
16-17 April 2023	39.25	AMC_{II}	13.65	2.0475
18-20 April 2023	50.33	AMC_{II}	18.73	2.8095
(1) - 23-24 April 2023	20.09	AMC_I	11.19	2.238
(2) - 23-24 April 2023	28.97	AMC_I	4.05	0.81
(1) - 28-29 April 2023	30.52	AMC_I	17.96	3.592
(2) - 28-29 April 2023	46.81	AMC_{II}	1.27	0.1905
29-30 April 2023	35.22	AMC_I	19	3.8
30 April – 02 May 2023	53.34	AMC_{III}	17.13	1.713
01-03 May 2023	58.54	AMC_{III}	9.77	0.977
02-03 May 2023	67.06	AMC_{III}	49.16	4.916

Table 9. Previous 5 days precipitation, corresponding AMC, total precipitation and corresponding estimated initial loss for the 13 selected events.

4.9.3.1.3. Green and Ampt (GA) method

The Green and Ampt (GA) method was originally derived from a simplification of Richard's equation (1931) for unsaturated water flow. In this method, the soil is considered to have a uniform profile of infinite extent and constant initial water content. As the water content at the soil surface increases, the movement of water infiltration (wetting front) is assumed to have a piston displacement as shown in Figure 50 (USACE, 1994, 2023).

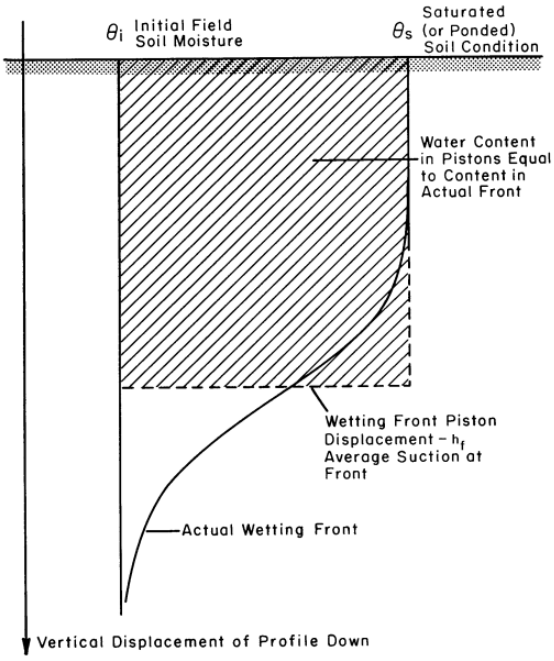

Figure 50. Conceptual representation of the Green and Ampt loss method (USACE, 1994).

The model computes the precipitation loss (f_t) in a time interval as:

$$f_t = K\left[\frac{1 + (Ø - \theta_i)S_f}{F_t}\right]$$

Where K is the saturated hydraulic conductivity, Ø is the effective porosity, θ_i is the initial moisture content (Ø – θ_i is the initial moisture deficit), S_f is the wetting front suction and F_t is the cumulative loss at time t (USACE, 2023).

The model requires 4 parameters:

1. The saturated hydraulic conductivity which represents the minimum rate (mm/h) at which water can infiltrate into the soil once the soil is fully saturated.
2. The wetting front suction head (mm) which describes the movement of water downwards through the soil column, it describes in fact the attraction of water within the void spaces of the soil column.
3. The effective porosity which is the porosity portion that is interconnected and actually contributes to water flow through the soil.

These first 3 parameters can be estimated based on the Green and Ampt parameters estimations for soil texture classes (see Appendix 10) realized by Rawls *et al.* (1983) as

recommended by USACE (2024) and Chow *et al.* (1988). For clay loams, the effective porosity is estimated at 0.309, the wetting front suction head at 208.8 mm, and the hydraulic conductivity at 0.01 mm/h.

4. The initial water content can be related to AMC (Sahu *et al*., 2023).

The Muramba station, one of the ARES meteorological stations, measures both soil moisture and precipitation and, like Nyarutovu watershed, is located on clay loam soil. A relationship between previous 5 days precipitation and volumetric soil moisture at 20 cm depth (Déogratias Nahayo, personal communication; Pessl Instruments, 2024b) was derived for this station. This relationship was derived from daily data collected between November 2021 and September 2023, during which no precipitation outliers were identified (see Figure 51). This equation can be transferred to Nyarutovu watershed to estimate the initial soil water content for each event based on the previous 5 days precipitation (see Table 10):

$$\text{Water content} = 0.1294\ (\mathrm{P}_{5\ \mathrm{days}}) + 4.8587$$

The observations seem to be in agreement and of the same order of magnitude with the residual water content (7.5%) and field capacity (31.8%) for clay loam reported by Rawls *et al*. (1982).

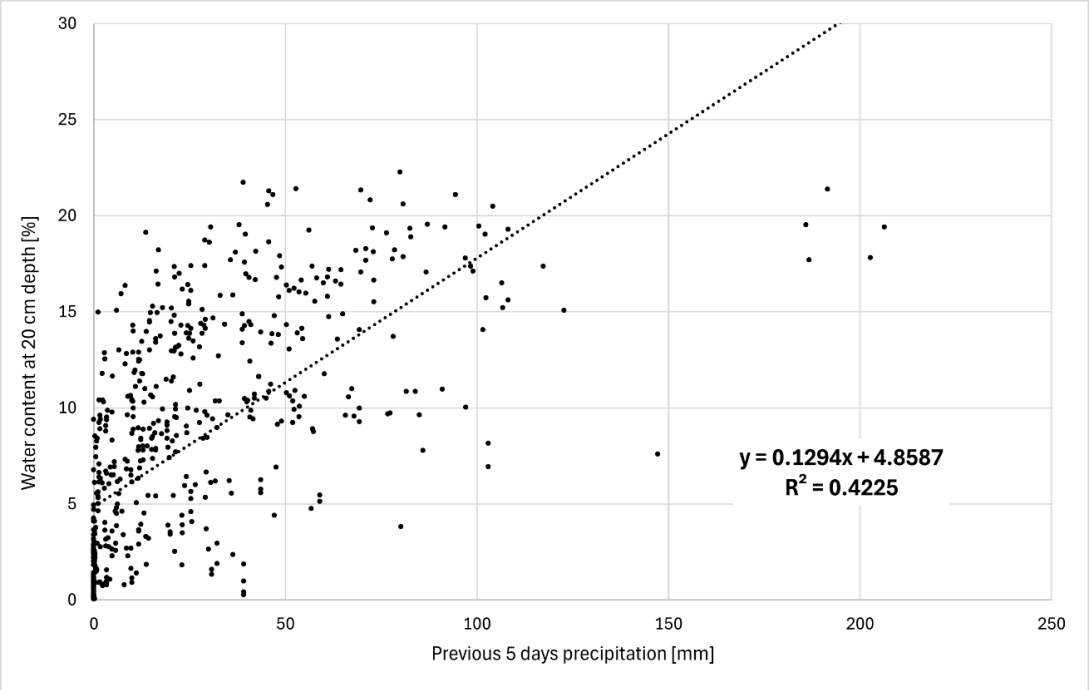

Figure 51. Relation between the previous 5 days precipitation and the water content at 20 cm depth for the Muramba station.

Date	Previous 5 days precipitation (mm)	Estimated initial water content
31 March 2023	5.34	0.055
02-03 April 2023	26.99	0.084
15-16 April 2023	32.06	0.090
16-17 April 2023	39.25	0.099
18-20 April 2023	50.33	0.114
(1) - 23-24 April 2023	20.09	0.075
(2) - 23-24 April 2023	28.97	0.086
(1) - 28-29 April 2023	30.52	0.088
(2) - 28-29 April 2023	46.81	0.109
29-30 April 2023	35.22	0.094
30 April – 02 May 2023	53.34	0.118
01-03 May 2023	58.54	0.124
02-03 May 2023	67.06	0.135

Table 10. Previous 5 days precipitation and corresponding estimated initial water content for the 13 selected events.

4.9.3.2. Transform methods

Among the 7 transform methods available in HEC-HMS, the Soil Conservation Service – Unit Hydrograph (SCS-UH) was selected for this work.

The SCS-UH model has been effectively applied to simulate extreme precipitation-runoff events in various regions. Haddad (2022) successfully used this method in Algeria, while Athira *et al*. (2023) achieved similar success in Kerala, India. The combination of SCS-UH with the SCS-CN loss method has been identified as the optimal approach for predicting flood discharges due to its simplicity and minimal data requirements (Duan & Froehlich, 2012). Furthermore, Zema *et al*. (2017) endorsed the SCS-UH method for its efficiency, noting that it only requires a single parameter. Supporting this, Zelelew and Melesse (2018) found that the SCS-UH method was the most effective transform method in their study conducted in northwest Ethiopia.

4.9.3.2.1. Unit Hydrograph concept

Before explaining in more details the selected method, the basic concepts of unit hydrographs will be first explained. The unit hydrograph is defined as the hydrograph of storm runoff resulting from an unitary precipitation excess (1 cm for example) generated uniformly over the drainage area at a constant rate for an effective duration. In other words, it is the pulse response function of a watershed. The two important principles of the unit hydrograph are: (1) the principle of proportionality, which tells us that we can scale the unit hydrograph according to the excess precipitation volume of each event, and (2) the principle of superposition, which allows us to sum the scaled hydrographs for all rainfall events, taking into account their temporal distribution (Chow *et al.*, 1988; Raghunath, 2006; USACE, 2023). Theses concepts are illustrated in Figure 52.

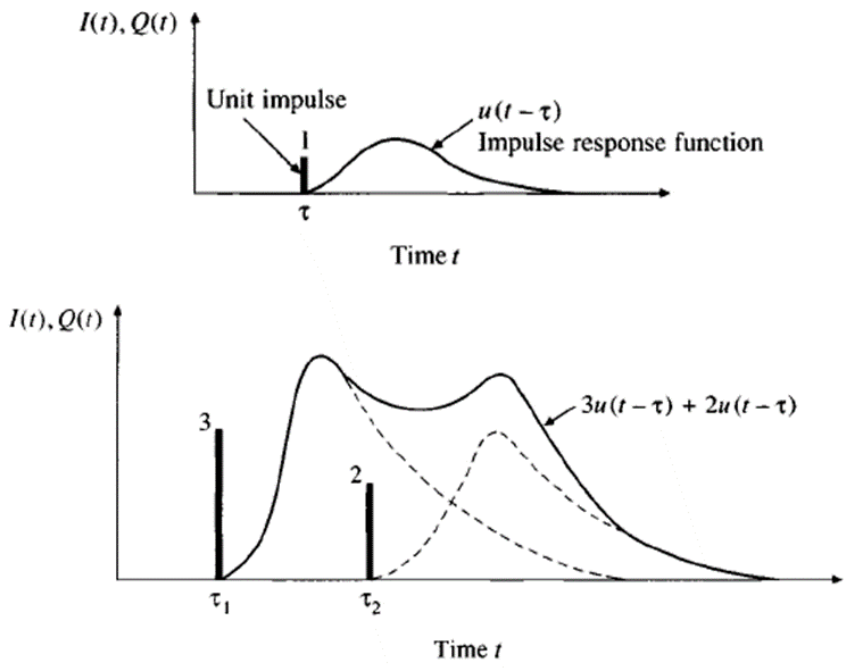

Figure 52. Illustration of the concept of unit hydrograph and the principles of proportionality and superposition (Chow *et al.*, 1988).

4.9.3.2.2. Soil Conservation Service – Unit Hydrograph (SCS-UH) method

The SCS-UH method is based on a dimensionless, curvilinear unit hydrograph for which the discharge (q) is a fraction of the peak discharge (q_p), and the time (t) is a fraction of the time to peak (T_p).

The lag time (L) is related to the time of rise as:

$$T_p = \frac{t_r}{2} + L$$

Where t_r is the duration of excess precipitation (or computational time step) (USACE, 2023).

To apply the method in HEC-HMS, the lag time parameter has to be estimated. Several formula to calculate lag time from watershed morphologic characteristics exist and they often yield results with significant differences (Sultan *et al.*, 2022). The USDA (2010) has proposed a formula for time lag which was used successfully in a lot of studies (Athira *et al.*, 2023; Bucała-Hrabia *et al.*, 2020; Duan & Froehlich, 2012). This formula can be written, after conversion to the S.I. system and in minutes, as follows:

$$L = \frac{(LF\ 3280.84)^{0.8}\ (\frac{1000}{CN} - 9)^{0.7}}{1900\ \sqrt{S}} * 60$$

Where L is the lag time (min), LF is the longest flowpath length (km), CN is the curve number of the Watershed and S represents the average basin slope (%). The lag time calculated with this formula for the Nyarutovu watershed is 65.18 minutes.

Finally, another parameter must be defined: the peak rate factor (PRF). A change in the peak rate factor results in a change in the percentage of runoff occurring before the time of peak. With standard settings (PRF = 484), 37.5% of total runoff occurs before the peak (USACE, 2023). However, for mountainous watersheds, a PRF value of 600 is recommended (Cahyono & Adidarma, 2019; Młyński *et al.*, 2020; USACE, 2023). Indeed, small mountainous catchments are characterized by a rapid response to precipitation, resulting in high peak flows and short flood durations. Higher PRF values reflect the shape of such floods (Młyński *et al.*, 2020). An illustration of the influence of variation of the PRF is available in Appendix 11.

4.9.3.3. Calibration

HEC-HMS provides an automatic parameter calibration module that allows for the calibration of loss and transform method parameters to ensure that the simulated flow rates match the observed flow rates as closely as possible. Several objective functions are available for calibration. Here, the minimization of the peak discharge error has been used, as suggested

by USACE, 2023, since we are interested in peak flooding. This objective function is calculated as follows:

$$\text{Percent error in peak discharge} = 100\ \frac{\mathrm{q_s(peak)} - \mathrm{q_0(peak)}}{\mathrm{q_0(peak)}}$$

Where $\mathrm{q_s(peak)}$ is the simulated peak discharge and $\mathrm{q_0(peak)}$ is the observed peak discharge.

The parameters for the three loss methods were calibrated individually for each event. Note that the 02-03 May, 2023 event was not used for calibration as its peak discharge is not known due to probable overtopping. For the SCS-CN method, the Curve Number (CN) was optimized. For the Initial and Constant rate method (IC), the constant rate was adjusted. For the Green-Ampt method (GA), the conductivity was optimized. Additionally, the lag time was optimized for each event within the transform method to find the observed lag times for individual events as done by McEnroe *et al*. (2016). The lag time was constrained to be equal to or greater than 52 minutes because HEC-HMS requires the simulation time step to be smaller than 0.29 times the lag time.

Once the parameters had been optimized for each event, the median values were calculated and used to attempt to simulate all 13 events. The median is often used as a measure of central tendency because it is not significantly affected by outliers (McEnroe *et al*., 2016). The aim is to determine whether stable parameters have been identified for the Nyarutovu watershed that can be used to reliably simulate floods. The parameters that were not optimized (initial abstraction for IC, effective porosity, the wetting front suction head and the initial water content for GA) were kept unchanged.

5. Results

5.1. Precipitation and discharge time series

The precipitation and discharge time series produced are shown in Figure 53.

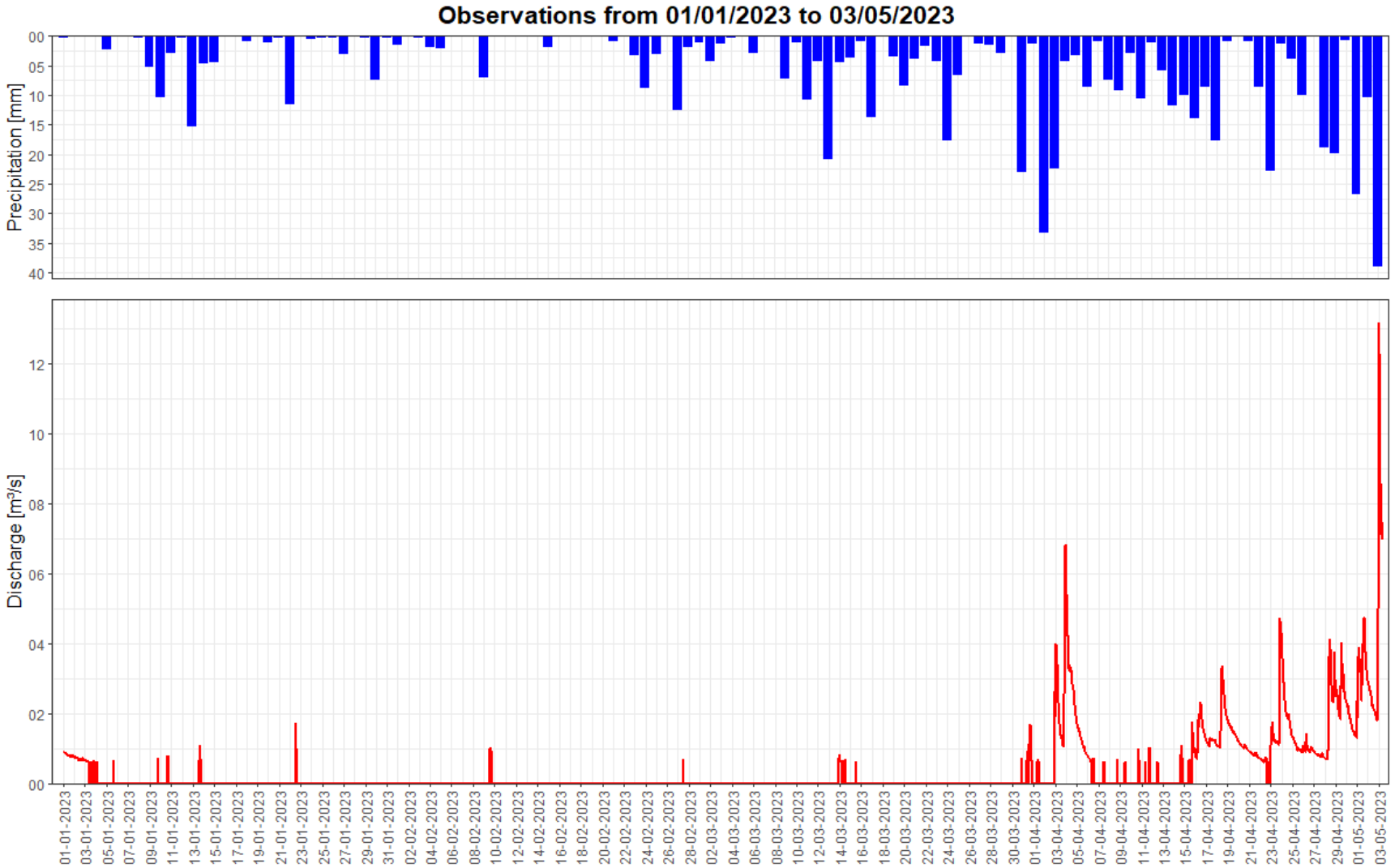

Figure 53. Precipitation and discharge observation time series for the period January 1, 2023 to May 3, 2023. Note that only daily precipitation is displayed, but the data with 15-minute time steps are actually those used for hydrologic modeling.

A total of 697 mm was measured in Nyarutovu watershed, which is fairly close to the average values for Rwanda for the same months (607 mm). The monthly precipitation measured was distributed differently from the average monthly precipitation for Rwanda (1991-2020) (World Bank, 2021). As shown in Figure 54, in January and February 2023, there was a precipitation deficit, while in March, April and May 2023, there was a precipitation surplus. These results are consistent with the high water events that took place in April and May 2023 in the study area. The highest precipitation rate was measured on March 31, 2023 at 11:30 with 52.85 mm/h recorded.

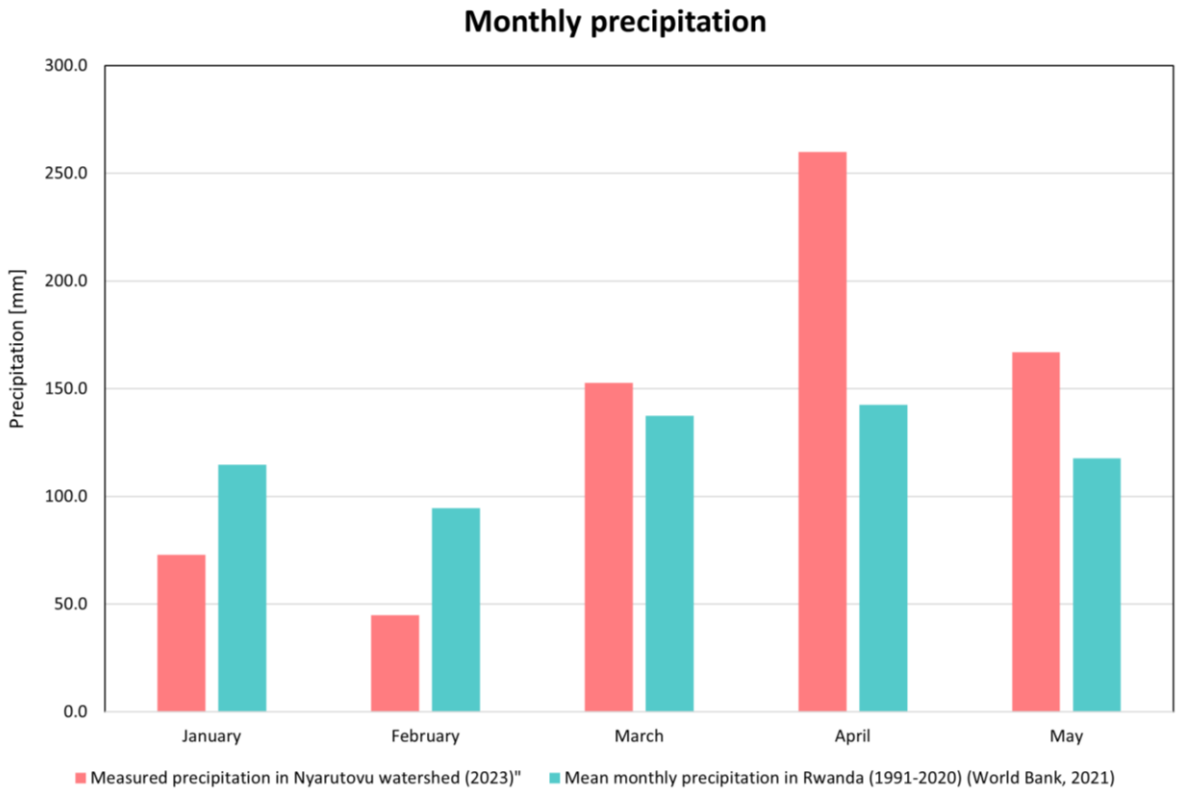

Figure 54. Comparison between the mean monthly precipitation in Rwanda (1991-2020) and the observed precipitation in the Nyarutovu subbasin for the months of January, February, March, April, and May 2023.

5.2. First HEC-HMS simulations

The first HEC-HMS simulations with the parameters found in the literature lead to poor performance, with percent error in peak discharge up to 16,284.37 % (see Table 11 and Figure 55). No loss method performed well. The SCS-CN simulated no flow for 7 of the events while 3 simulations had errors in peak discharge between -100 and 100 %, as illustrated by the example of the 02-03 April, 2023 event in Figure 56. The IC and GA methods systematically

and grossly overestimated discharges as illustrated in Figure 57. In other words, the IC and GA methods greatly underestimated the infiltration capacity of Nyarutovu watershed.

		SCS-CN		IC		GA	
Date	Observed peak discharge (m^3/s)	Sim. peak disch (m^3/s)	Error in peak disch. (%)	Sim. peak disch. (m^3/s)	Error in peak disch. (%)	Sim. peak disch. (m^3/s)	Error in peak disch. (%)
31 March 2023	1.07	0	-100	133.1	12297.72	175.9	16284.37
02-03 April 2023	3.99	6.5	62.80	159.6	3897.38	215.7	5302.48
15-16 April 2023	1.05	0	-100	58.4	5471.80	79.1	7446.75
16-17 April 2023	1.64	0.4	-75.57	29.2	1683.5	41.3	2422.55
18-20 April 2023	2.33	2.4	2.97	58.5	2409.78	80.4	3349.34
(1) - 23-24 April 2023	3.63	0	-100	21.1	480.6	48.2	1226.3
(2) - 23-24 April 2023	1.06	0	-100	18.9	1677.26	28.7	2598.8
(1) - 28-29 April 2023	3.46	0	-100	18.6	438.13	43.4	1155.64
(2) - 28-29 April 2023	1.96	0	-100	0.7	-64.31	6.5	231.39
29-30 April 2023	2.20	0	-100	81.5	3599.77	116.7	5197.71
30 April - 02 May 2023	2.62	19.3	637.72	33.2	1169.03	55.3	2013.77
01-03 May 2023	2.91	4.3	47.67	35.3	1112.24	55.3	1799.07
02-03 May 2023	11.4	123	978.95	129.3	1034.21	158.1	1286.84

Table 11. Observed and simulated peak discharges and corresponding error in peak discharge of the 13 selected events for the first HEC-HMS simulations with parameters found in the literature.

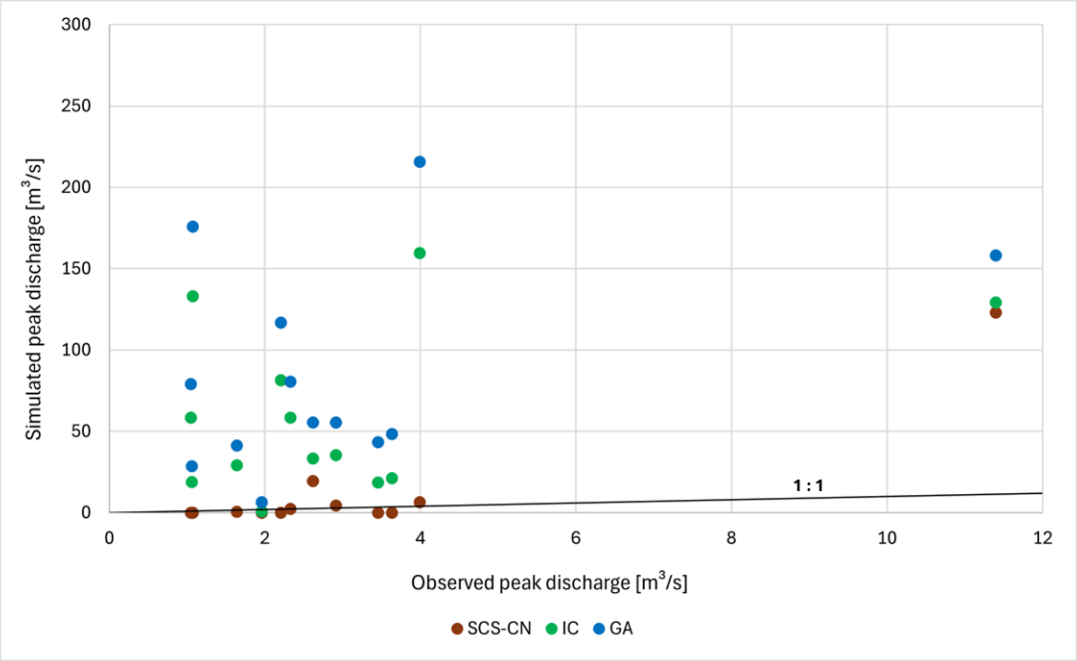

Figure 55. Comparison of observed and simulated peak discharges of the 13 selected events for the 3 loss methods with parameters found in the literature.

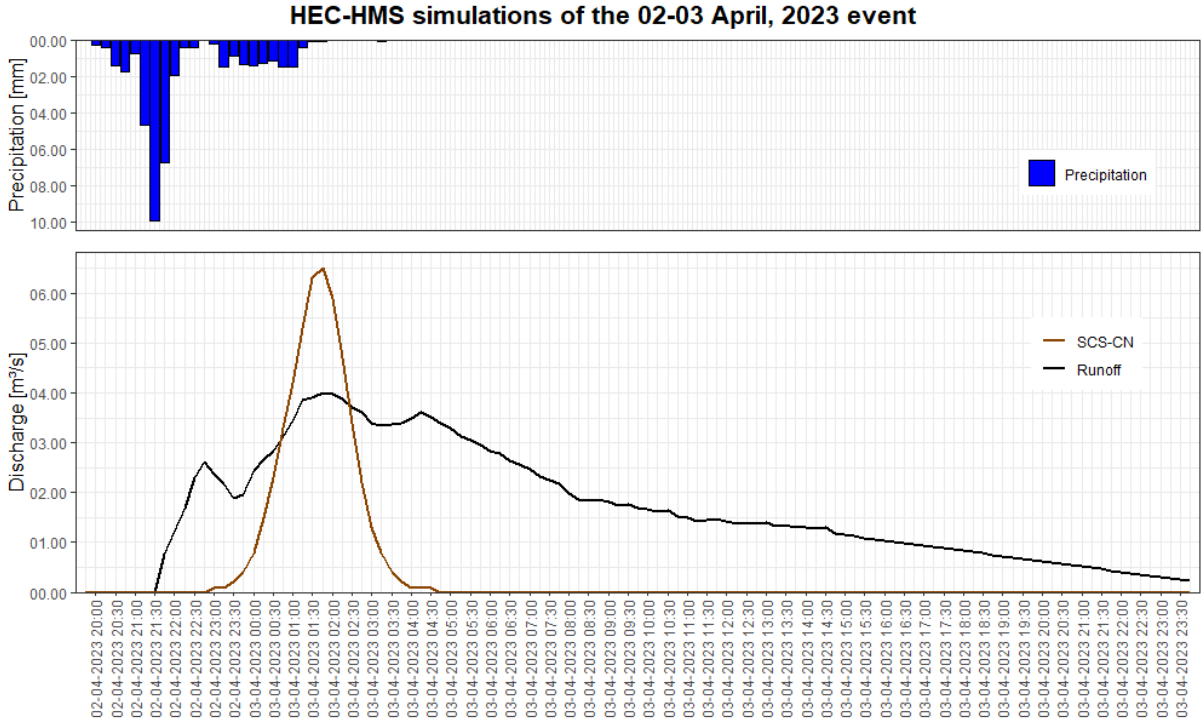

Figure 56. HEC-HMS simulation of the 02-03 April, 2023 event with the SCS-CN method (parameters found in the literature).

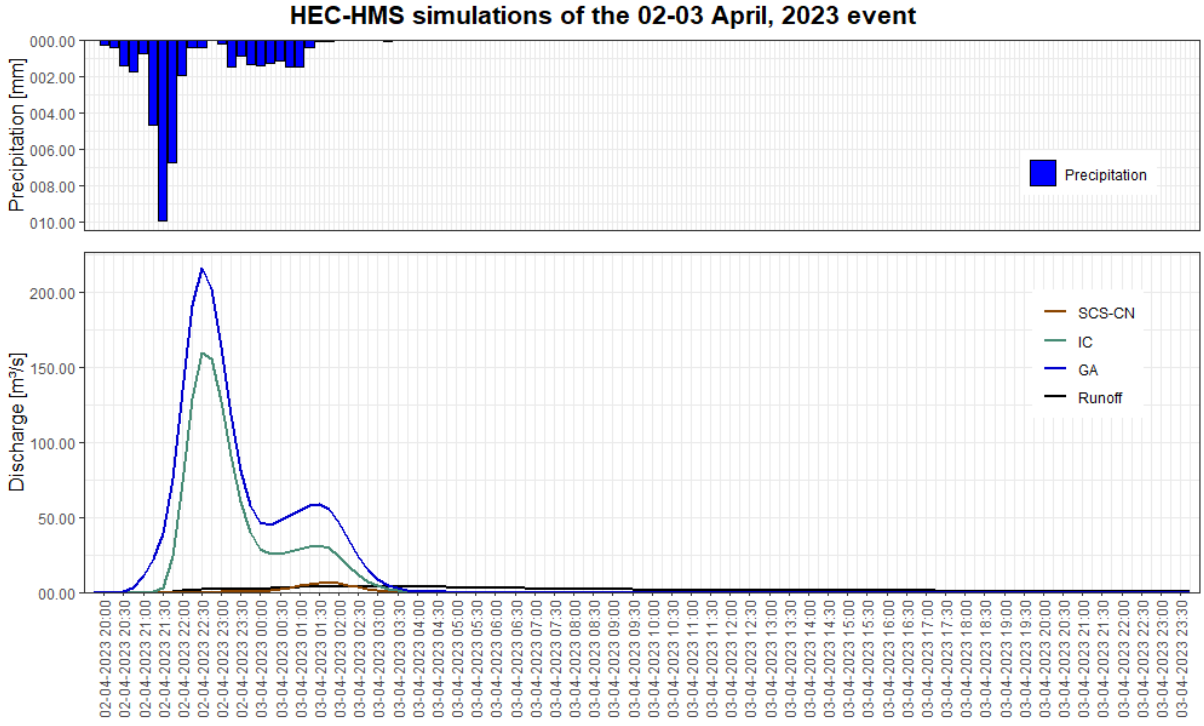

Figure 57. HEC-HMS simulation of the 02-03 April, 2023 event with the 3 loss methods (parameters found in the literature).

The rest of the simulations plots are available in Appendices 12 to 26.

5.3. HEC-HMS calibrations

The optimization of the parameters for each event (see Appendices 27 to 38) reveals a wide variation between events, indicating that no stable parameters have emerged for the Nyarutovu watershed. These parameters are listed in Table 12.

The optimized CN of the SCS-CN method ranges from 67 to 98.9, with a median value of 85.4. For the IC method, the optimized constant rate varies from 0.8 to 51.7 mm/h, with a median value of 9.6 mm/h. The conductivity in the GA method ranges from 0.01 to 11.3 mm/h, with a median value of 1.5 mm/h. The median lag time is 239.21 minutes.

	SCS-CN		**IC**		**GA**	
Date	CN	Lag time (min)	Constant rate (mm/h)	Lag time (min)	Conductivity (mm/h)	Lag time (min)
31 March 2023	76.1	293.2	51.7	184.2	11.3	132.6
02-03 April 2023	67.0	240.0	33.3	278.2	8.4	181.8
15-16 April 2023	89.2	254.8	23.5	52	2.6	226.7
16-17 April 2023	86.3	247.0	11.4	258.5	2.1	237.1
18-20 April 2023	84.6	278.5	12.6	287.6	2.7	298.7
(1) - 23-24 April 2023	94.05	269.1	6.4	103.0	0.5	107.8
(2) - 23-24 April 2023	96.4	256.4	7.8	195.5	0.4	223.2
(1) - 28-29 April 2023	84.4	242.6	4.4	300	0.9	192.5
(2) - 28-29 April 2023	98.9	55.2	0.8	278.0	0.01	245.8
29-30 April 2023	81.6	269.9	24.3	221.9	2.9	299.9
30 April - 02 May 2023	84.4	238.4	6.8	178.9	0.6	190.0
01-03 May 2023	92.1	236.0	7.2	160.1	0.5	295.4

Table 12. Optimized parameters of the 3 loss methods and the transform method after HEC-HMS calibration of each events.

5.4. HEC-HMS simulations with optimized parameters

As might be expected given the wide variation in parameters during calibration, the simulations with the optimized parameters (median values from calibration) are still of very poor quality (see Table 13 and Figure 58), with error in peak discharge up to 729 % for SCS-CN, 2713 % for IC and 2424.3 % for GA. The simulations plots are available in Appendices 39 to 51. Unfortunately, even after attempting to calibrate the parameters using observed data, none of the three loss methods successfully simulated the relationship between precipitation and discharge at the scale of the Nyarutovu watershed. At this point, it is clear that forecasting a flood event would be impossible, given the instability of parameters found for the Nyarutovu watershed.

		SCS-CN		IC		GA	
Date	Observed peak discharge (m^3/s)	Sim. peak disch (m^3/s)	Error in peak disch. (%)	Sim. peak disch. (m^3/s)	Error in peak disch. (%)	Sim. peak disch. (m^3/s)	Error in peak disch. (%)
31 March 2023	1.07	8.9	729.0	30.2	2713.0	27.1	2424.3
02-03 April 2023	3.99	27.7	593.8	35.5	789.1	39.8	896.8
15-16 April 2023	1.05	0.1	-90.5	10.1	863.6	4.8	358.0
16-17 April 2023	1.64	1.3	-20.6	3.0	83.2	3.7	126.0
18-20 April 2023	2.33	3.1	33.0	7.4	217.5	10.0	329.0
(1) - 23-24 April 2023	3.63	0.0	-100.0	0.8	-78.0	0.0	-100.0
(2) - 23-24 April 2023	1.06	0.0	-100.0	0.0	-100.0	0.0	-100.0
(1) - 28-29 April 2023	3.46	4.3	24.4	0.0	-100.0	0.6	-82.6
(2) - 28-29 April 2023	1.96	0.0	-100.0	0.0	-100.0	0.0	-100.0
29-30 April 2023	2.20	5.5	149.7	14.0	535.5	11.3	413.0
30 April - 02 May 2023	2.62	3.3	26.1	0.0	-100.0	0.0	-100.0
01-03 May 2023	2.91	0.1	-96.6	0.3	-89.7	0.0	-100.0
02-03 May 2023	11.4	43.8	284.2	28.9	153.5	51.7	353.5

Table 13. Observed and simulated peak discharges and corresponding error in peak discharge of the 13 selected events for the first HEC-HMS simulations with the optimized parameters (same parameters for all 13 events).

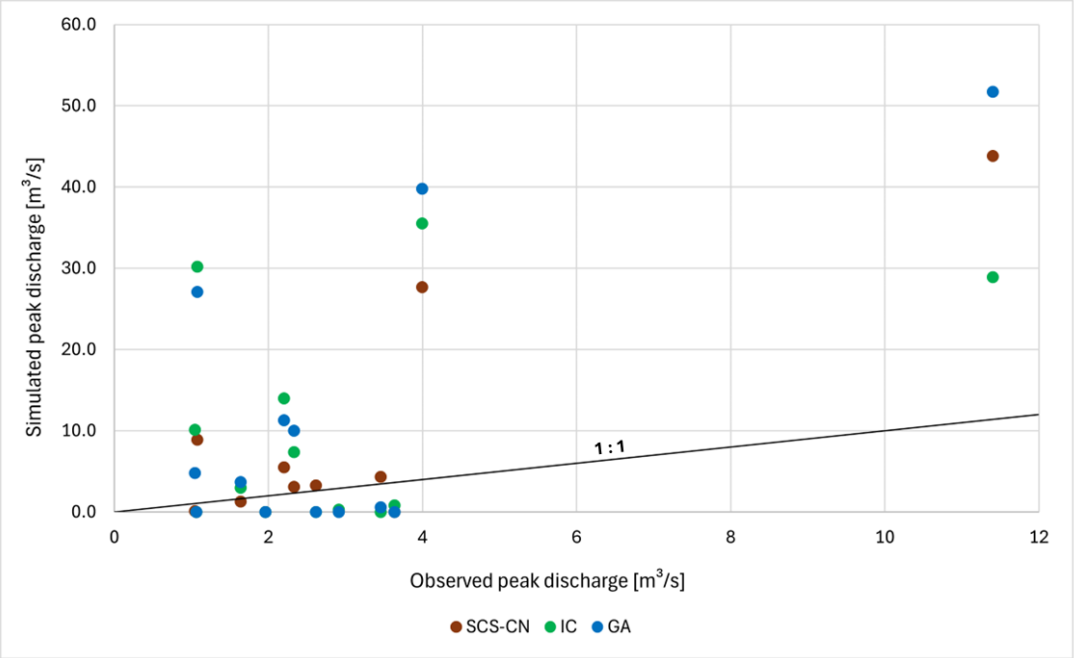

Figure 58. Comparison of observed and simulated peak discharges of the 13 selected events for the 3 loss methods with the optimized parameters.

6. Discussion

Poor results may obscure other interesting and underlying findings. In this sense, it is necessary to discuss and try to understand what has led to the poor results to draw potential conclusions.

6.1. Data uncertainty

Watershed hydrologic modeling, along with the associated calibration and verification processes, requires a large amount of spatial and temporal data, such as topography, land use, land cover, soil types, and precipitation and discharge monitoring data. In practice, the availability and quality of these data often present significant challenges. Often, the overall quality of the modeling can be compromised due to a lack of high-resolution data for developing, calibrating, and validating the model. In hydrologic modeling, the accuracy of the results is often more dependent on data quality than on the quality of the models used, as input errors propagate through the model, directly affecting the accuracy of the final predictions. Therefore, quantifying and understanding the uncertainty in hydrologic input data is essential for correctly interpreting modeling results (Buytaert *et al*., 2006; Chu & Steinman, 2009; De Silva *et al*., 2014; Nandalal & Ratnayake, 2016). Furthermore, it should be noted that the actual study period is relatively short. Precipitation and discharge data are available from January 1, 2023, to May 3, 2023, but almost no discharge events were measured before late March, which limits the analysis period and thus the number of events studied. Having more significant events would likely have improved the quality of the hydrologic modeling.

6.1.1. Uncertainty in precipitation data

Precipitation is the most important input factor in hydrologic modeling. However, this input is subject to uncertainty due to measurement errors, systematic errors in the interpolation method, and stochastic errors arising from the random nature of rainfall (Buytaert *et al*., 2006). Uncertainty in precipitation data can lead to incorrect simulation results and sometimes even to erroneous conclusions (Belayneh *et al*., 2020). Reliable and accurate precipitation data are particularly important in small watersheds, where flows are sensitive to

variations on small spatial and temporal scales due to rapid hydrologic response and high watershed variability (Cristiano *et al*., 2017).

As highlighted in the methodology, many outliers had to be manually cleaned. It is possible that some incorrect data may have survived the cleaning process. Furthermore, accurately estimating the spatial distribution of precipitation from punctual observations is challenging. This is particularly true in mountainous environments, where irregular topography further influences precipitation patterns. The spatial variability of precipitation is often influenced by local topographical differences and the orientation of mountains, which can amplify variability through processes such as rain shading and strong winds (Belayneh *et al*., 2020; Buytaert *et al*., 2006). Furthermore, Fiener & Auerswald (2009) found that, for a small test site (1.4 km²) in southern Germany, spatial variability increased with precipitation intensity and that, for single events, the assumption of spatially uniform precipitation is invalid on the sub-kilometer scale.

The most effective way to improve the quality of spatial precipitation estimation would be to increase the density of the monitoring network. However, this approach is often very costly and frequently impractical (Buytaert *et al*., 2006).

To put things into perspective, the surface area of each of the rain gauges used for this study is 200 cm², which, compared with the 45.15 km² of the Nyarutovu watershed, represents only 0.00000004% of the study area. However, the methodology used for this study, i.e. IDW interpolation, involves only 3 stations, of which Janja has a weight of 79.9%. It is assumed that the measurements from the Janja station, and to a lesser extent from the Busengo and Muramba stations, are representative of the precipitation across the entire Nyarutovu watershed. However, the Nyarutovu watershed is located in a mountainous, tropical zone and is subject to high spatial variability in precipitation. Precipitation data recorded by Busengo, Janja and Muramba stations (the 3 closest to Nyarutovu) provide evidence of intense localized precipitation on the days of the 13 selected events as illustrated in Figure 59, 60 & 61 (see Appendices 52 to 57 for all other days of selected events).

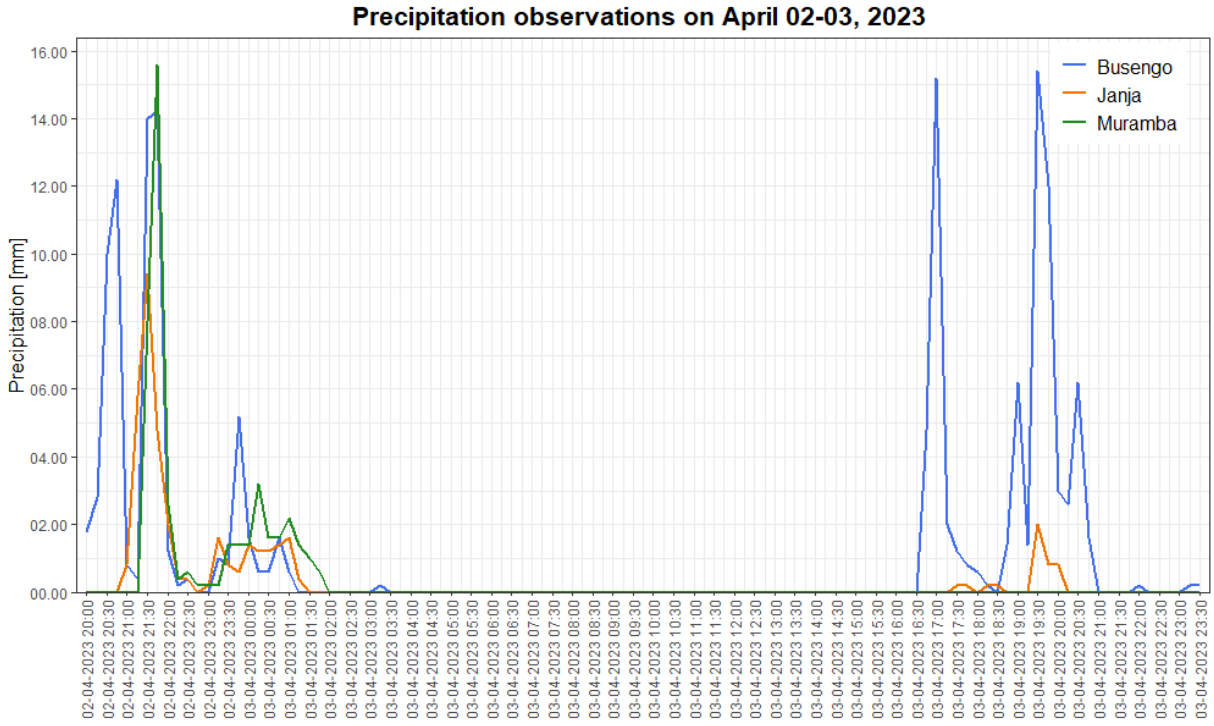

Figure 59. Precipitation observations on 02-03 April, 2023 providing evidences of intense and localized precipitation.

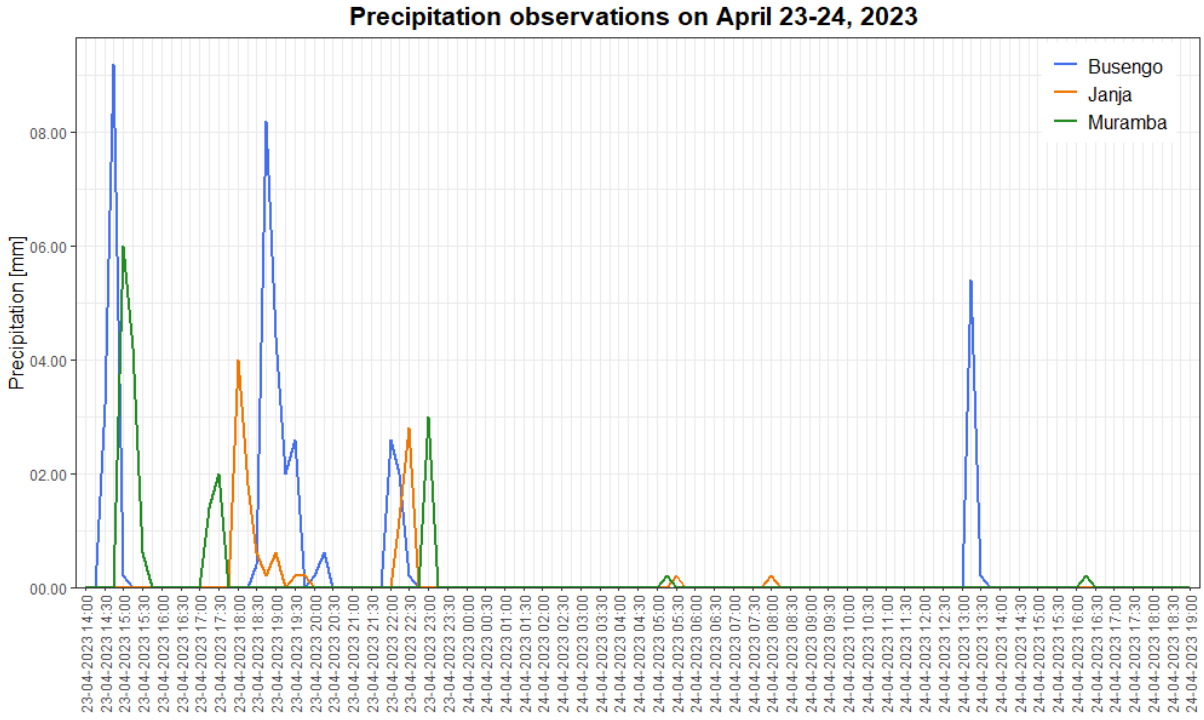

Figure 60. Precipitation observations on April 23-24, 2023 providing evidences of intense and localized precipitation.

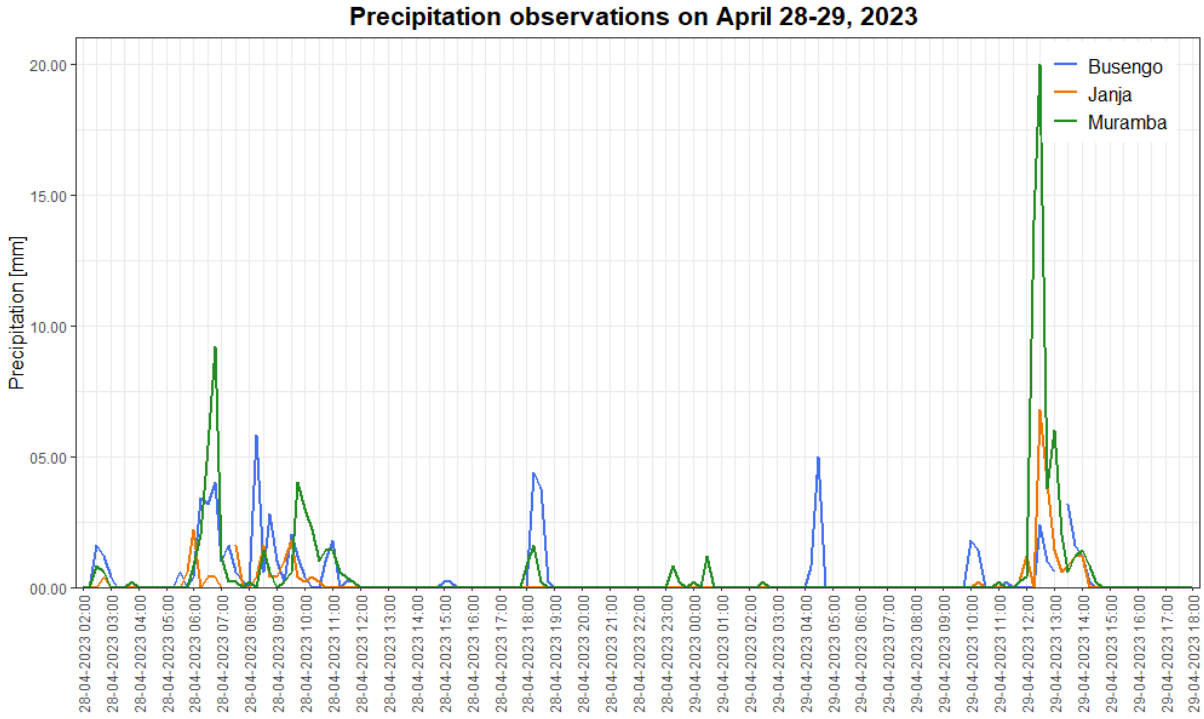

Figure 61. Precipitation observations on 28-29 April, 2023 providing evidences of intense and localized precipitation.

For hydrologic modeling, the consequences of such precipitation behaviors vary depending on the case. If an intense, very local storm occurs in a part of the watershed with no rain gauge, it could be recorded as a small precipitation event if less intense precipitation occur above the rain gauges available. However this event can result in a large discharge event in the dataset due to the not recorded storm. During calibration in HEC-HMS, the parameters for this event will tend to underestimate the storage and infiltration capacity of the watershed, as we try to force the model to produce a flow with less precipitation than actually occurred. Conversely, if an intense and very local rainfall event falls over the Janja station, this measurement is then extrapolated (at 79.9%) to the entire catchment. When calibrating in HEC-HMS, the parameters will tend to overestimate the infiltration or retention capacity of the watershed, as the model has more precipitation input than actually occurred to simulate the observed flow.

This lack of precision in estimating the actual precipitation over the entire watershed is most likely the main reason for the poor results in hydrologic modeling, along with the fact that the parameters of the loss methods vary with each event. It is in fact not possible to find a stable relationship for the watershed if the input data are not correct. The discharge will be systematically overestimated when the precipitation is overestimated and conversely,

underestimated when the precipitation is underestimated. Taking March 31, 2023, as an example, we measured very intense precipitation (up to 52.85 mm/h). This intense local event is certainly not representative of the watershed as a whole. For this reason, we note that during simulations, this event has the most overestimated peak flows. During calibration, this is the event for which the optimized parameters suggest the most a watershed that stores precipitation and has high infiltration capacities (low CN, high constant rate and high conductivity for SCS-CN, IC and GA loss methods respectively). Gunathilake *et al*. (2020) experienced similar problems with the hydrologic modeling of a tropical watershed, attributing mismatches in peak discharge to localized storm events.

6.1.2. Uncertainty in discharge data

As explained in the methodology for discharge data, discharge observations are estimated indirectly from water level via the rating curve, and water level is itself estimated indirectly from pressure probe observations. Consequently, discharge data are rarely correct and are subject to many sources of error (Kastali *et al*., 2022).

Water level data are dependent on the quality of pressure observations. Incorrect water levels may be calculated if there are too great differences in atmospheric pressure between the Diver and BaroDiver. As we have just discussed, there are many storms in the Nyarutovu catchment area, and these are usually accompanied by pressure drops.

The main source of uncertainty in discharge data is the rating curve. Indeed, as previously explained, the establishment of the rating curve was laborious. It was established from water level observations and discharge measurements, as the water level at the staff gauge was not recorded during the discharge measurements. Furthermore, significant uncertainties arise when discharge measurement dates are likely incorrect, as evidenced by the fact that no water level was measured on October 6, 2022, and that the manual observer also noted a water level of 0, whereas the measured discharge is 3.41 m^3/s. Additionally, the water levels used to establish the rating curve are the average water levels recorded from 08:00 to 12:00 on the presumed discharge measurement days. In the end, only 5 points are used to establish the rating curve, 4 of which have their discharge measured using the floating method, which is not very accurate. It should also be noted that the riverbed can change, in which case the rating curve no longer corresponds to the river.

Moreover, according to the rating curve, the flows below 0.5258 m^3/s are not measurable. Below this value it is impossible to know whether the flow is zero or if there is a flow that is simply not measured by the Diver.

Finally, some outliers must be discarded, such as the flow data for April 4, 2023 (Mukungwa overtopping) or the peak discharge on May 3, 2023, which correspond to a water level of over 2.5 m and which, according to the estimated height of the Nyarutovu banks, correspond to an overtopping, making the rating curve unusable (Cosandey & Robinson, 2000). This further adds to the uncertainty in the discharge data.

6.2. Hydrologic modeling

Even if the data were perfectly accurate, there are still uncertainties in hydrologic modeling, given that we are attempting to model, and therefore simplify, all the complex natural processes involved between precipitation and runoff in a watershed.

Firstly, as discussed in the methodology section, the method for separating baseflow, which assumes it is constant throughout the event, is a simplification and can be prone to error, despite its intention to be a straightforward method to apply. Furthermore, the separation of events by extending the recession curves is subjective and questionable.

Zema *et al*. (2017) state that the applicability of HEC-HMS outside of the USA, where the model was initially developed, is not fully established. Therefore, it requires further testing under various geomorphological and climatic conditions to confirm its spatial transferability to different environmental contexts.

The SCS-CN loss method is one of the most popular techniques for predicting direct runoff volume of a given rainfall event (Soulis *et al*., 2009). However the method has several disadvantages such as its high sensitivity to its sole parameter: the curve number. Even a small error in estimating the CN can have significant impact on the simulated runoff (Ponce & Hawkins, 1996; Soomro *et al*., 2019). Other disadvantages include the absence of clear guidance on how to vary antecedent condition, the varying accuracy of the method for different biomes, the empirical ratio of 0.2 between initial abstraction and maximum potential retention which does not take into account the storm characteristics and timing (Ponce & Hawkins, 1996; USACE, 2023). Additionally, the method does not take into account the

intensity and the temporal distribution of precipitation. Consequently, the same loss will be computed by the method if it rains 1 mm in one day or in 15 minutes (Soulis *et al*., 2009; USACE, 2023). Furthermore, Halwatura & Najim (2013) report that the SCS-CN method did not perform well in a tropical catchment in Sri Lanka and USACE (2023) states that the applicability of the method elsewhere than midwestern USA is uncertain. As can be seen from the results, the Nyarutovu watershed does not appear to have a stable CN. In fact, the CN is dependent on each event. Moreover, a detailed examination reveals that the calibrated CN values exhibit a very strong relationship with the total precipitation of the events (R^2 = 0.94), as illustrated in Figure 62. This behavior, which has been documented in previous studies, suggests a situation where the SCS-CN method does not perform well (Hawkins, 1993; Soulis *et al*., 2009).

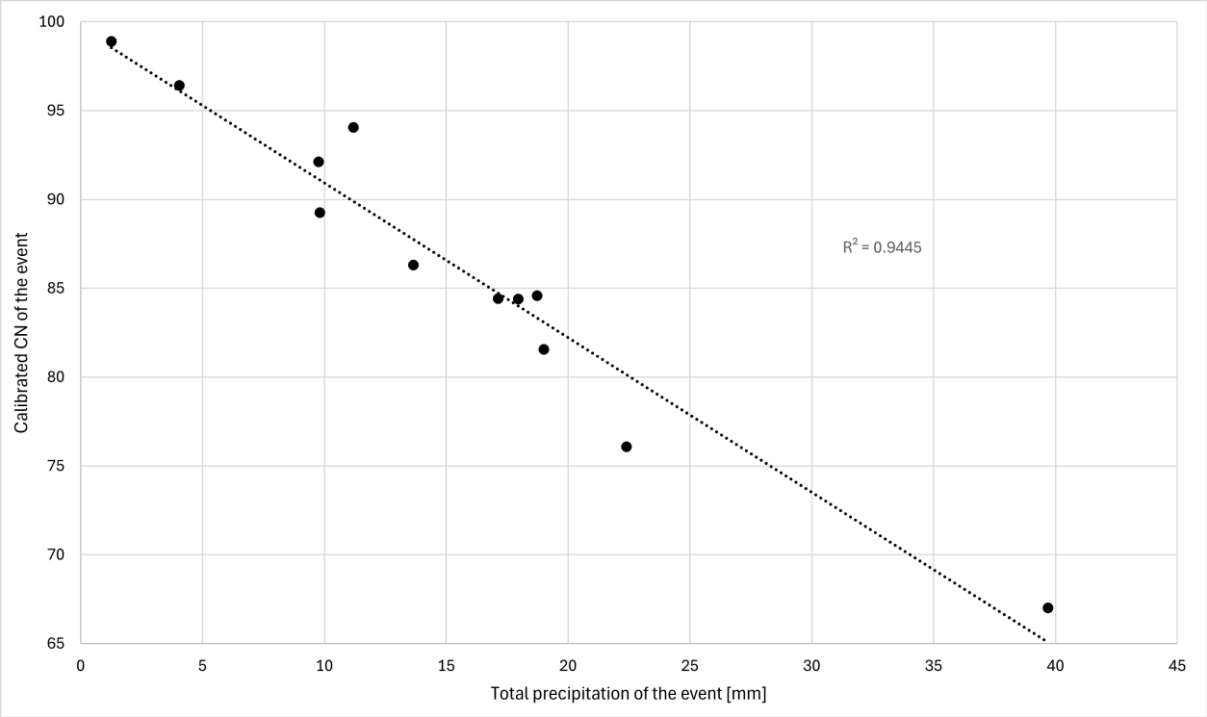

Figure 62. Relation between the calibrated SCS-CN curve number and the total precipitation of the events.

For the IC and GA loss methods, it appears that the initial parameters found in the literature and used for the first simulations significantly underestimated the infiltration capacity of the Nyarutovu watershed. As discussed by Duan & Froehlich (2012), the application of these methods depends on the accurate determination of their parameters. However, these estimations are complex due to the wide range of values for different soil types found in the literature. USACE (2023) states that the Initial and Constant (IC) method may be too simple to accurately predict losses within an event. Meanwhile, the Green-Ampt (GA) method is not

widely used because it is less parsimonious than other simpler methods, resulting in less practical experience with it compared to the simpler methods. Moreover, similar to SCS-CN, there is a quite strong relationship between total event precipitation and the calibrated parameters: the constant rate for IC and conductivity for GA (see Figure 63). This raises questions about the applicability of these methods, as the parameters seem to vary significantly with each event.

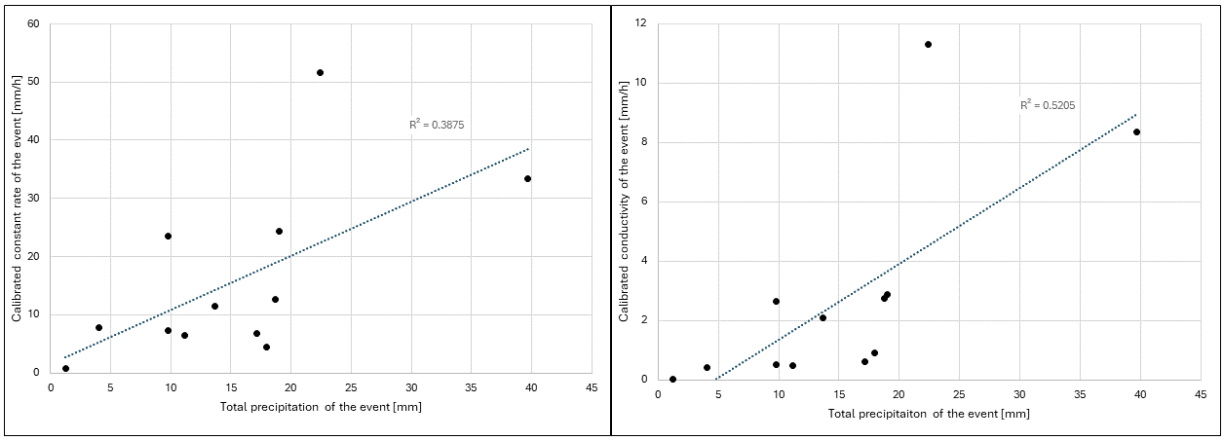

Figure 63. Relationships between the total precipitation and the calibrated parameters of the events (from left to right: the constant rate of the IC method and the conductivity of the GA method.

Finally, the SCS-UH transform method is a simplification of reality and introduces its own uncertainties. Despite its successful application in many studies, Bhunya *et al*. (2011) suggest that for catchments larger than 16 km², the method can introduce large errors. The method assumes that the lag time for the watershed is constant. However, lag time varies with each event, particularly influenced by the intensity, spatial and temporal distribution of precipitation (Sultan *et al*., 2022; Zhang *et al*., 2007).

7. Conclusion

In conclusion, this master thesis focused on studying a small (45.15 km²) watershed in northwest Rwanda. This mountainous region is prone to flood risks, especially flash floods (FloodList, 2024; Nsengiyumva, 2012). The goal of this work was to model the dynamics between precipitation and runoff at the Nyarutovu watershed scale.

The first step involved cleaning and preparing precipitation and discharge data rigorously for hydrologic modeling. This resulted in precipitation and discharge time series from January 1, 2023, to May 3, 2023. The subsequent study focused on selecting 13 events for modeling, separating baseflow, and distinguishing between individual events. Then, the hydrologic modeling software HEC-HMS was utilized. This model comprises two critical components: (1) the loss method, which simulates precipitation losses and excess precipitation, and (2) the transform method, which converts this excess precipitation into an outlet hydrograph (Sahu *et al*., 2023). Among the available methods, three loss methods were employed: Soil Conservation Service - Curve Number (SCS-CN), Initial and Constant (IC), and Green-Ampt (GA) methods, as well as one transform method: Soil Conservation Service - Unit Hydrograph (SCS-UH) transform method. The parameterization of these methods involved identifying optimal parameters from literature sources related to LULC, soil texture type, and local characteristics. The parameters were then calibrated using observations. Unfortunately, the results of the simulations and calibration were found to be very poor.

The most likely reason for these poor results is the uncertainty associated with the data, which often impacts the accuracy of the results more significantly than the methods employed (De Silva *et al*., 2013). Specifically, accurate precipitation data are crucial as it is the most important input factor in hydrologic modeling (Buytaert *et al*., 2006). However, precipitation data are affected by uncertainties. It is evident that the average precipitation calculated through IDW interpolation from the three rain gauges may often not be representative of the precipitation across the entire Nyarutovu watershed, given the significant spatial variability of precipitation documented from precipitation observations. Finally, discharge data are also approximations and prone to errors, while hydrologic modeling itself involves numerous approximations, and the methods used are not perfect.

Looking forward, increasing the density of rain gauge networks could provide more reliable precipitation data necessary for accurate hydrologic modeling and improved understanding of flood dynamics in vulnerable areas. Hopefully, this will enable flood predictions and provide early warnings to populations. Nevertheless, it should be noted that the rain gauge network is already densely established due to the efforts of the ARES LAFHAZAV project. Further increasing the density of this network may not be financially feasible (Bernard Tychon, personal communication). Another potential solution to enhance precipitation measurement for future studies is the use of remote sensing data. In developing countries, where the rain gauge networks are limited, satellite precipitation products can serve as a valuable alternative. For example, Natumanya *et al*. (2022) used successfully the NASA-Power precipitation estimates to model precipitation-runoff relationship in Mozambique. Furthermore, as Uijlenhoet *et al*. (2018) highlighted, microwave links in cellular communication networks also present a valuable opportunity to provide high-resolution precipitation observations. This technique could be particularly accurate and useful in mountainous regions, which are susceptible to flash flooding.

References

Ahmad Shafuan, M. F., Nurhidayu, S., & Kamarudin, N. (2018). SCS-CN in Tropics: Is It Reliable? *The Pertanika Journal of Scholarly Research Reviews*, 3. Retrieved July 2024 from https://www.researchgate.net/publication/323118860_SCS-CN_in_Tropics_Is_It_Reliable/link/5a8104fda6fdcc0d4bac48d6/download?_tp=eyJjb250ZXh0Ijp7ImZpcnN0UGFnZSI6InB1YmxpY2F0aW9uIiwicGFnZSI6InB1YmxpY2F0aW9uIn19

Al Jazeera and News Agencies. (2023). *Flash floods hit western Rwanda, killing more than 100.* Retrieved October 2023 from https://www.aljazeera.com/news/2023/5/3/at-least-55-killed-in-rwanda-flash-floods

Alaska Satellite Facility Distribution Active Archive Center (ASF DAAC). (2014). *ALOS PALSAR Radiometric Terrain Correction (RTC)* (includes material from JAXA/METI, 2011). Retrieved March 2024 from https://asf.alaska.edu/datasets/daac/alos-palsar-radiometric-terrain-correction/

Athira, S., Katpatal, Y. B., & Londhe, D. S. (2023). Flood Modelling and Inundation Mapping of Meenachil River Using HEC-RAS and HEC-HMS Software. In S. Haddout, P. Krishnamoorthy Lakshmi, & A. M. Hoguane. (eds.). *Climate Change and Ocean Renewable Energy*. Cham: Springer Nature Switzerland, 113–130. https://doi.org/10.1007/978-3-031-26967-7_9

Beilicci, E. & Beilicci, R. (2015). A comparative analysis of two advanced hydroinformatic tools for rainfall – runoff phenomena modeling. *Scientific Bulletin of Politehnica University of Timişoara, Transactions on Hydrotechnics*, 60(74), 2. Retrieved March 2024 from https://www.ct.upt.ro/buletinhidro/2015-2/0010Erika_2.pdf

Belayneh, A., Sintayehu, G., Gedam, K., & Muluken, T. (2020). Evaluation of satellite precipitation products using HEC-HMS model. *Modeling Earth Systems and Environment*, 6(4), 2015–2032. https://doi.org/10.1007/s40808-020-00792-z

Bhunya, P. K., Panda, S. N., & Goel, M. K. (2011). Synthetic Unit Hydrograph Methods: A Critical Review. *The Open Hydrology Journal*, 5(1). Retrieved July 2024 from https://benthamopen.com/ABSTRACT/TOHYDJ-5-1

Blume, T., Zehe, E., & Bronstert, A. (2007). Rainfall—Runoff response, event-based runoff coefficients and hydrograph separation. *Hydrological Sciences Journal*, 52(5), 843–862. https://doi.org/10.1623/hysj.52.5.843

Bucała-Hrabia, A., Kijowska-Strugała, M., Bryndal, T., Cebulski, J., Kiszka, K., & Kroczak, R. (2020). An integrated approach for investigating geomorphic changes due to flash flooding in two small stream channels (Western Polish Carpathians). *Journal of Hydrology: Regional Studies*, 31, 100731. https://doi.org/10.1016/j.ejrh.2020.100731

Buytaert, W., Celleri, R., Willems, P., Bièvre, B. D., & Wyseure, G. (2006). Spatial and temporal rainfall variability in mountainous areas: A case study from the south Ecuadorian Andes. *Journal of Hydrology*, 329(3), 413–421. https://doi.org/10.1016/j.jhydrol.2006.02.031

Cahyono, C., & Adidarma, W. (2019). Influence analysis of peak rate factor in the flood events' calibration process using HEC–HMS. *Modeling Earth Systems and Environment*, 5. https://doi.org/10.1007/s40808-019-00625-8

Carreta *et al*. (2023). *Climate Change 2022 – Impacts, Adaptation and Vulnerability: Working Group II Contribution to the Sixth Assessment Report of the Intergovernmental Panel on Climate Change* (1st ed.). Cambridge University Press, 551–712. https://doi.org/10.1017/9781009325844

Centre for Research on the Epidemiology of Disasters United Nations Office for Disaster Risk Reduction (CRED). (2020). *The human cost of disasters: An overview of the last 20 years (2000-2019) | UNDRR.* Retrieved January 2024 from http://www.undrr.org/publication/human-cost-disasters-overview-last-20-years-2000-2019

Chorowicz, J. (2005). The East African rift system. *Journal of African Earth Sciences*, 43(1), 379–410. https://doi.org/10.1016/j.jafrearsci.2005.07.019

Chow, V. T., Maidment, D. R., & Mays, L. W. (1988). *Applied hydrology*. New York: McGraw-Hill. Retrieved July 2024 from https://wecivilengineers.wordpress.com/wp-content/uploads/2017/10/applied-hydrology-ven-te-chow.pdf

Chu, X., & Steinman, A. (2009). Event and Continuous Hydrologic Modeling with HEC-HMS. *Journal of Irrigation and Drainage Engineering*, 135(1), 119–124. https://doi.org/10.1061/(ASCE)0733-9437(2009)135:1(119)

Cosandey, C., & Robinson, M. (2000). *Hydrologie continentale*. Paris: Armand Colin, 368 p.

Cristiano, E., ten Veldhuis, M.-C., & van de Giesen, N. (2017). Spatial and temporal variability of rainfall and their effects on hydrological response in urban areas – a review. *Hydrology and Earth System Sciences*, 21(7), 3859–3878. https://doi.org/10.5194/hess-21-3859-2017

De Silva, M. M. G. T., Weerakoon, S. B., & Herath, S. (2014). Modeling of Event and Continuous Flow Hydrographs with HEC–HMS: Case Study in the Kelani River Basin, Sri Lanka. *Journal of Hydrologic Engineering*, 19(4), 800–806. https://doi.org/10.1061/(ASCE)HE.1943-5584.0000846

Duan, Z., & Froehlich, D. C. (2012). Comparing influence of combinations of precipitation loss and rainfall excess-runoff transform models to flood flow rate in a flatland watershed. *International Journal of Hydrology Science and Technology*, 2(1), 22–33. https://doi.org/10.1504/IJHST.2012.045937

Duncan, H. P. (2019). Baseflow separation – A practical approach. *Journal of Hydrology*, 575, 308–313. https://doi.org/10.1016/j.jhydrol.2019.05.040

Fang, X., Cleveland, T., Garcia, C. A., Thompson, D., & Malla, R. (2005). *Literature review on timing parameters for hydrographs.* Department of Civil Engineering, Lamar University, Beaumont, 83 p. Retrieved July 2024 from https://www.depts.ttu.edu/techmrtweb/documents/reports/complete_reports/4696_complete.pdf

Fiener, P., & Auerswald, K. (2009). Spatial variability of rainfall on a sub-kilometre scale. *Earth Surface Processes and Landforms*, 34(6), 848–859. https://doi.org/10.1002/esp.1779

FloodList. (2023). *Rwanda – FloodList*. Retrieved January 2024 from https://floodlist.com/tag/rwanda

Genç, O., Ardıçlıoğlu, M., & Ağıralioğlu, N. (2015). Calculation of mean velocity and discharge using water surface velocity in small streams. *Flow Measurement and Instrumentation*, 41, 115–120. https://doi.org/10.1016/j.flowmeasinst.2014.10.013

Gilewski, P. (2021). Impact of the grid resolution and deterministic interpolation of precipitation on rainfall-runoff modeling in a sparsely gauged mountainous catchment. *Water*, 13(2), 230. https://doi.org/10.3390/w13020230

Gunathilake, M. B., Panditharathne, P., Gunathilake, A. S., & Warakagoda, N. (2020). Application of a HEC-HMS model on event-based simulations in a tropical watershed. *Engineering and Applied Science Research*, 47(4), 349–360. https://doi.org/10.14456/EASR.2020.38

Haddad, A. (2022). Extreme Rainfall-Runo Events Modeling Using HEC-HMS Model for Oued El Hachem Watershed, Northern Algeria. *Archives of Hydro-Engineering and Environmental Mechanics*, 69(1), 45–57. https://doi.org/10.2478/heem-2022-0004

Halwatura, D., & Najim, M. M. M. (2013). Application of the HEC-HMS model for runoff simulation in a tropical catchment. *Environmental Modelling & Software*, 46, 155–162. https://doi.org/10.1016/j.envsoft.2013.03.006

Hauet, A., Morlot, T., & Daubagnan, L. (2018). Velocity profile and depth-averaged to surface velocity in natural streams: A review over a large sample of rivers. *E3S Web of Conferences*, 40, 06015. https://doi.org/10.1051/e3sconf/20184006015

Hawkins, R. H., Hjelmfelt, A. T., & Zevenbergen, A. W. (1985). Runoff Probability, Storm Depth, and Curve Numbers. *Journal of Irrigation and Drainage Engineering*, 111(4), 330–340. https://doi.org/10.1061/(ASCE)0733-9437(1985)111:4(330)

Hengl, T., Heuvelink, G. B. M., Kempen, B., Leenaars, J. G. B., Walsh, M. G., Shepherd, K. D., *et al*. (2015). Mapping Soil Properties of Africa at 250 m Resolution: Random Forests Significantly Improve Current Predictions. *PLOS ONE*, 10(6), e0125814. https://doi.org/10.1371/journal.pone.0125814

Icyimpaye, G., Abdelbaki, C., & Mourad, K. A. (2022). Hydrological and hydraulic model for flood forecasting in Rwanda. *Modeling Earth Systems and Environment*, 8(1), 1179–1189. https://doi.org/10.1007/s40808-021-01146-z

Impact Observatory, Microsoft & Esri. (2024). *Sentinel-2 10m land use/land cover time series of the world* [LULC map for 2023]. Retrieved April 2024 from https://livingatlas.arcgis.com/landcoverexplorer/#mapCenter=81.18780%2C6.76158%2C9.611111111111111&mode=step&timeExtent=2017%2C2023&year=2023

Jalili Pirani, F., & Modarres, R. (2020). Geostatistical and deterministic methods for rainfall interpolation in the Zayandeh Rud basin, Iran. *Hydrological Sciences Journal*, 65(16), 2678–2692. https://doi.org/10.1080/02626667.2020.1833014

Jonard, F. (2023). Notes from the spatial analysis course given at ULg to students of the master in geography, orientation global change [formula of the IDW interpolation method].

Jonkman, S. N. (2005). Global perspectives on loss of human life caused by floods. *Natural Hazards*, 34(2), 151–175. https://doi.org/10.1007/s11069-004-8891-3

Jurgiel, B., Verchere, P., Tourigny, E. & Becerra, J. (2023). *Profile Tool* [QGIS Extension]. Retrieved March 2023 from https://github.com/PANOimagen/profiletool

Karamage, F., Zhang, C., Fang, X., Liu, T., Ndayisaba, F., Nahayo, L., Kayiranga, A. & Nsengiyumva, J. B. (2017). Modeling Rainfall-Runoff Response to Land Use and Land Cover Change in Rwanda (1990–2016). *Water*, 9(2), 147. https://doi.org/10.3390/w9020147

Kastali, A., Zeroual, A., Zeroual, S., & Hamitouche, Y. (2022). Auto-calibration of HEC-HMS Model for Historic Flood Event under Rating Curve Uncertainty. Case Study: Allala Watershed, Algeria. *KSCE Journal of Civil Engineering*, 26(1), 482–493. https://doi.org/10.1007/s12205-021-1051-4

Kazezyılmaz-Alhan, C. M., Yalçın, İ., Javanshour, K., Aytekin, M., & Gülbaz, S. (2021). A hydrological model for ayamama watershed in Istanbul, Turkey, using HEC-HMS. *Water Practice and Technology*, 16(1), 154–161. https://doi.org/10.2166/wpt.2020.108

Kuksina, L. & Golosov, V. (2020). Flash floods: formation, study and distribution. *E3S Web of Conferences,* 163, 02005. https://doi.org/10.1051/e3sconf/202016302005

Langridge, M., Gharabaghi, B., McBean, E., Bonakdari, H., & Walton, R. (2020). Understanding the dynamic nature of Time-to-Peak in UK streams. *Journal of Hydrology*, 583, 124630. https://doi.org/10.1016/j.jhydrol.2020.124630

Li, L., & Mind'je, R. (2023). *Hydrogeological Hazard Susceptibility and Community Risk Perception in Rwanda: A Case Study of Floods and Landslides*. Singapore: Springer Nature, 107 p. https://doi.org/10.1007/978-981-99-1751-8

Ly, Sarann, Charles, C., & Degré, A. (2013). Different methods for spatial interpolation of rainfall data for operational hydrology and hydrological modeling at watershed scale: A review. *BASE,* 13(2). Retrieved February 2024 from https://popups.uliege.be/1780-4507/index.php?id=10003

Mair, A., & Fares, A. (2011). Comparison of Rainfall Interpolation Methods in a Mountainous Region of a Tropical Island. *Journal of Hydrologic Engineering*, 16(4), 371–383. https://doi.org/10.1061/(ASCE)HE.1943-5584.0000330

McEnroe, B. M., Young, C. B., Gamarra Zapata, R. A., & Kansas. Dept. of Transportation. Bureau of Research. (2016). *Estimation of watershed lag times and times of concentration for the Kansas City Area: Technical summary.* (No. KS-16-01). Retrieved August 2024 from https://rosap.ntl.bts.gov/view/dot/30791

Mind'je, R., Li, L., Amanambu, A. C., Nahayo, L., Nsengiyumva, J. B., Gasirabo, A., & Mindje, M. (2019). Flood susceptibility modeling and hazard perception in Rwanda. *International Journal of Disaster Risk Reduction*, 38, 101211. https://doi.org/10.1016/j.ijdrr.2019.101211

Młyński, D., Walega, A., Książek, L., Florek, J., & Petroselli, A. (2020). Possibility of Using Selected Rainfall-Runoff Models for Determining the Design Hydrograph in Mountainous Catchments: A Case Study in Poland. *Water*, 12, 1450. https://doi.org/10.3390/w12051450

Nandalal, H., & Ratnayake, U. (2016). Event Based Modeling of a Watershed Using HEC-HMS. *Engineer: Journal of the Institution of Engineers, Sri Lanka*, 43, 28. https://doi.org/10.4038/engineer.v43i2.6979

Natumanya, E., Ribeiro, N., Mwanjalolo, M. J. G., & Steinbruch, F. (2022). Using SWAT Model and Field Data to Determine Potential of NASA-POWER Data for Modelling Rainfall-Runoff in Incalaue River Basin. *Computational Water, Energy, and Environmental Engineering*, 11(2), 65–83. https://doi.org/10.4236/cweee.2022.112004

Nsengiyumva, J. B. (2012). *Disaster high risk zones on floods and landslides.* Republic of Rwanda, Ministry of disaster management and refugee affairs. 33 p. Retrieved January 2024 from *https://www.preventionweb.net/files/28208_highriskzonesreportfinalpublication.pdf*

Ntwali, D., Ogwang, B. A., & Ongoma, V. (2016). The Impacts of Topography on Spatial and Temporal Rainfall Distribution over Rwanda Based on WRF Model. *Atmospheric and Climate Sciences*, 6(2), 145–157. https://doi.org/10.4236/acs.2016.62013

OCHA Regional Office for Southern and Eastern Africa (ROSEA). (2020). *Rwanda - Subnational Administrative Boundaries*. [Data set]. Retrieved March 2024 from *https://data.humdata.org/dataset/cod-ab-rwa?*

OCHA Regional Office for Southern and Eastern Africa (ROSEA). (2015). *Rwanda—Water courses (Rivers)* [Data set]. Retrieved December 2023 from https://data.humdata.org/dataset/rwanda-water-courses

OCHA Regional Office for Southern and Eastern Africa (ROSEA). (2018). *Rwanda—Water Bodies (Lakes)* [Data set]. Retrieved December 2023 from https://data.humdata.org/dataset/rwanda-water-bodies?

Parasuraman, S. B., Mishra, S., & Singh, V. (2007). *SCS-CN method revisited*. Retrieved July 2024 from https://www.researchgate.net/publication/230822228_SCS-CN_method_revisited

Pessl Instruments. (2024a). *Precipitation sensors* [technical specifications]. Retrieved March 2024 from https://metos.global/en/precipitation-sensors/

Pessl Instruments. (2024b). *Soil moisture sensors* [technical specifications].Retrieved August 2024 from https://metos.global/en/soil-moisture-sensors/

Ponce, V. M., & Hawkins, R. H. (1996). Runoff Curve Number: Has It Reached Maturity? *Journal of Hydrologic Engineering*, 1(1), 11–19. https://doi.org/10.1061/(ASCE)1084-0699(1996)1:1(11)

Prabaswara, M. H. M. A., & Wickramaarachchi, T. N. (2022). Event-based rainfall-runoff simulation using different precipitation loss methods: Case study in tropical monsoon catchment. *Sustainable Water Resources Management*, 9(1), 16. https://doi.org/10.1007/s40899-022-00795-x

Raghunath, H.M. (2006). *Hydrology (Principles, Analysis Design)*. 2nd Edition, New Delhi: New Age International (P) Ltd., 463 p.

Rawls, W. J., & Brakensiek, D. L. (1982). Estimating Soil Water Retention from Soil Properties. *Journal of the Irrigation and Drainage Division*, 108(2), 166–171. https://doi.org/10.1061/JRCEA4.0001383

Rawls, W. J., Brakensiek, D. L., & Miller, N. (1983). Green-ampt Infiltration Parameters from Soils Data. *Journal of Hydraulic Engineering*, 109(1), 62–70. https://doi.org/10.1061/(ASCE)0733-9429(1983)109:1(62)

ReliefWeb. (2023). *Rwanda: Floods and Landslides—May 2023*. Retrieved November 2023 from https://reliefweb.int/disaster/fl-2023-000064-rwa

Ruth, M. (2021). *Africa boundaries* [Data set]. Retrieved December 2023 from https://hub.arcgis.com/datasets/07610d73964e4d39ab62c4245d548625

Sahu, M. K., Shwetha, H. R., & Dwarakish, G. S. (2023). State-of-the-art hydrological models and application of the HEC-HMS model: A review. *Modeling Earth Systems and Environment*, 9(3), 3029–3051. https://doi.org/10.1007/s40808-023-01704-7

Sardoii, E. R., Rostami, N., Sigaroudi, S. K., & Taheri, S. (2012). Calibration of loss estimation methods in HEC-HMS for simulation of surface runoff (case study: Amirkabir dam watershed, Iran). *Advances in Environmental Biology*, 6(1), 343–348. Retrieved July 2024 from https://www.researchgate.net/publication/289917089_Calibration_of_loss_estimation_methods_in_HECHMS_for_simulation_of_surface_runoff_case_study_Amirkabir_dam_watershed_Iran

Seneviratne *et al*. (2023). *Climate Change 2021 – The Physical Science Basis: Working Group I Contribution to the Sixth Assessment Report of the Intergovernmental Panel on Climate Change* (1st ed.). Cambridge University Press. https://doi.org/10.1017/9781009157896

Skaggs, R. W., and Khaleel, R. (1982). Chapter 4: Infiltration. *In* Haan, C.T., Johnson, H.P. & Brakenstek, D.L. (eds). *Hydrologic modelling of Small Watersheds*. Michigan: American Society of Agricultural Engineers. An ASAE Monograph Number 5 in a Series.

Soomro, A. G., Babar, M. M., Memon, A. H., Zaidi, A. Z., Ashraf, A., & Lund, J. (2019). Sensitivity of Direct Runoff to Curve Number Using the SCS-CN Method. *Civil Engineering Journal*, 5(12), 2738–2746. https://doi.org/10.28991/cej-2019-03091445

Soulis, K., Valiantzas, J., Dercas, N., & Londra, P. (2009). Analysis of the Runoff Generation Mechanism for the Investigation of the SCS-CN Method Applicability to A Partial Area Experimental Watershed. *Hydrology and Earth System Sciences*, 13, 605–615. https://doi.org/10.5194/hess-13-605-2009

Sultan, D., Tsunekawa, A., Tsubo, M., Haregeweyn, N., Adgo, E., Meshesha, D. T. *et al.* (2022). Evaluation of lag time and time of concentration estimation methods in small tropical watersheds in Ethiopia. *Journal of Hydrology: Regional Studies*, 40, 101025. https://doi.org/10.1016/j.ejrh.2022.101025

Tügel, F., Hassan, A., Hou, J., & Hinkelmann, R. (2022). Applicability of Literature Values for Green–Ampt Parameters to Account for Infiltration in Hydrodynamic Rainfall–Runoff Simulations in Ungauged Basins. *Environmental Modeling & Assessment*, 27(2), 205–231. https://doi.org/10.1007/s10666-021-09788-0

Uijlenhoet, R., Overeem, A., & Leijnse, H. (2018). Opportunistic remote sensing of rainfall using microwave links from cellular communication networks. *Wiley Interdisciplinary Reviews: Water*, 5(4). https://doi.org/10.1002/wat2.1289

USACE. (1994). *Flood-Runoff Analysis*. 214 p. Retrieved July 2024 from https://www.publications.usace.army.mil/Portals/76/Publications/EngineerManuals/em_1110-2-1417.pdf

USACE. (2023). *HEC-HMS technical reference manual*. 246 p. Retrieved October 2023 from https://www.hec.usace.army.mil/confluence/hmsdocs/hmstrm

USACE. (2024). *HEC-HMS tutorials and guides*. 2304 p. Retrieved July 2024 from https://www.hec.usace.army.mil/confluence/hmsdocs/hmsguides

USDA. (1986). *Urban Hydrology for Small Watersheds. Technical Release 55 (TR-55)*. 164 p. Retrieved February 2024 from https://www.nrc.gov/docs/ML1421/ML14219A437.pdf

USDA. (2010). Time of concentration. *In* USDA NRCS, *Part 630 Hydrology, National Engineering Handbook*, 29 p. Retrieved May 2024 from https://irrigationtoolbox.com/NEH/Part630_Hydrology/NEH630-ch15draft.pdf

USDA. (2017). *Soil Survey Manual*. Agriculture Handbook No. 18, 639 p. Retrieved July 2024 from https://www.nrcs.usda.gov/sites/default/files/2022-09/The-Soil-Survey-Manual.pdf

USGS. (n.d.). *What are the two types of floods? | U.S. Geological Survey*. Retrieved January 2024 from https://www.usgs.gov/faqs/what-are-two-types-floods

Uwizeyimana, D., Mureithi, S. M., Mvuyekure, S. M., Karuku, G., & Kironchi, G. (2019). Modelling surface runoff using the soil conservation service-curve number method in a drought prone agro-ecological zone in Rwanda. *International Soil and Water Conservation Research,* 7(1), 9–17. https://doi.org/10.1016/j.iswcr.2018.12.001

Van Essen Instruments. (2004). *TD Diver Product manual*. 34 p. Retrieved February 2024 from https://www.daiki.co.jp/Manual/Diver%20(GB)%20HL341v3.pdf

Van Essen Instruments. (2016). *Diver product manual*. 26 p. Retrieved April 2024 from https://www.vanessen.com/images/PDFs/Diver-ProductManual-en.pdf

World Bank. (2021).*Climate Change Knowledge Portal.* Retrieved November 2023 from https://climateknowledgeportal.worldbank.org/

World Bank. (2017). *Poverty and Inequality Platform* [Open data]. Retrieved November 2023 from https://data.worldbank.org

World Meteorological Organization (WMO), FFEM, Institut de Recherche pour le développement (IRD) & Groupe des écoles EIER – ETSHER. (2007). *Training session on calibration of rating curves.* Retrieved April 2023 from https://library.wmo.int/idurl/4/56139

United Nations Population Division. (2018). *Urban and rural populations* [open data] Retrieved November 2023 from https://population.un.org/wup/Download/

Xin, Z., Shi, K., Wu, C., Wang, L., & Ye, L. (2019). Applicability of Hydrological Models for Flash Flood Simulation in Small Catchments of Hilly Area in China. Open Geosciences, 11(1), 1168–1181. https://doi.org/10.1515/geo-2019-0089

YSI. (2020). *Flow Probes—FP111, FP211, and FP311* [Specification sheet]. Retrieved from https://www.ysi.com/File%20Library/Documents/Specification%20Sheets/FP111-Flow-Probe-Specification-Sheet.pdf

Zelelew, D. G., & Melesse, A. M. (2018). Applicability of a Spatially Semi-Distributed Hydrological Model for Watershed Scale Runoff Estimation in Northwest Ethiopia. *Water*, 10(7), 923. https://doi.org/10.3390/w10070923

Zema, D. A., Labate, A., Martino, D., & Zimbone, S. M. (2017). Comparing Different Infiltration Methods of the HEC-HMS Model: The Case Study of the Mésima Torrent (Southern Italy). *Land Degradation & Development*, 28(1), 294–308. https://doi.org/10.1002/ldr.2591

Zhang, S., Liu, C., Yao, Z., Guo, L. (2007). Experimental study on lag time for a small watershed. *Hydrological Processes*, 21, 1045–1054. https://doi.org/10.1002/hyp.6285

Appendix

Appendix 1: Location of Mukungwa watershed and Nyarutovu subbasin in relation to Rwandan provinces and districts.

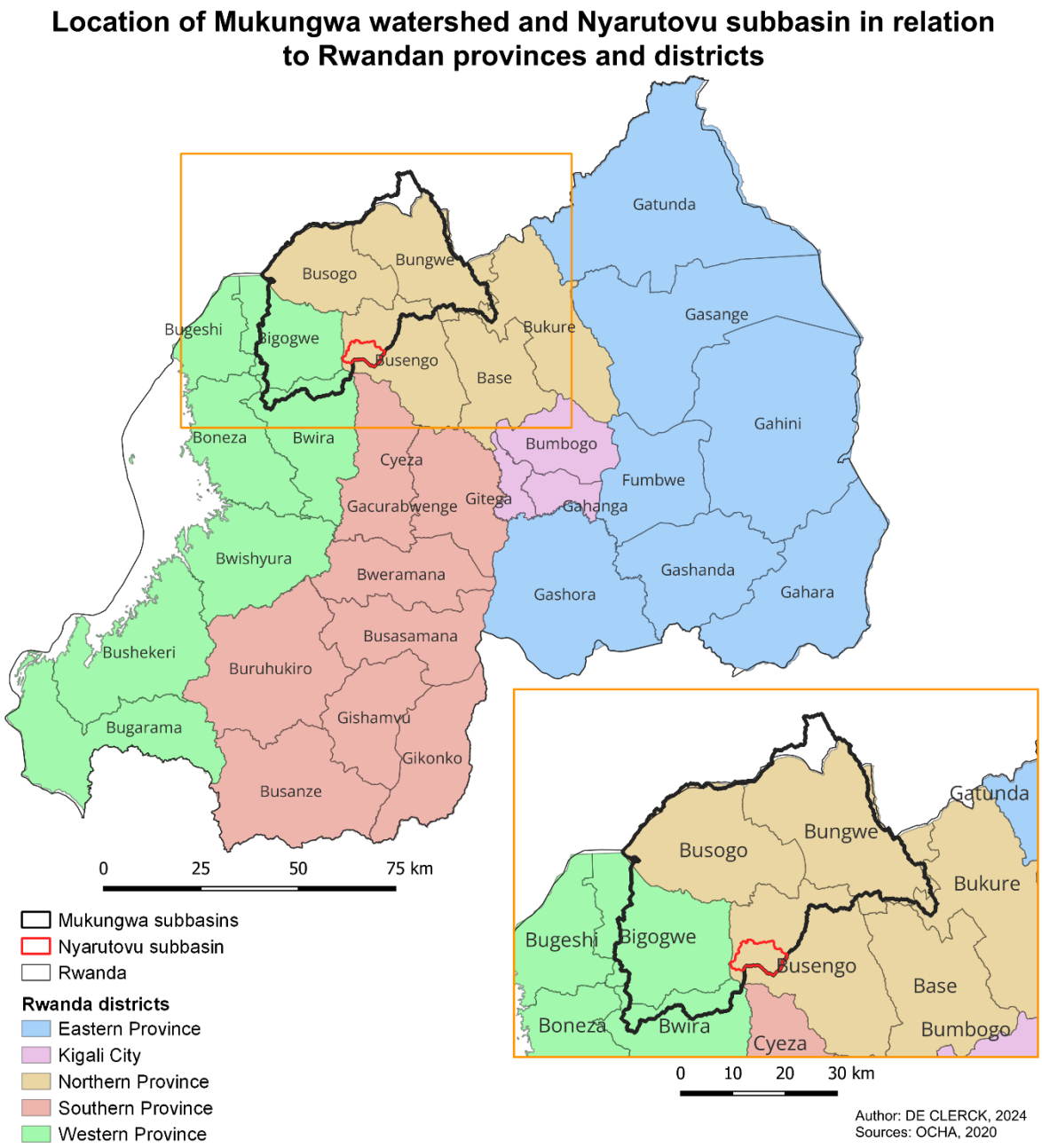

Appendix 2: Flood susceptibility map for Rwanda and Mukungwa watersheds (Mind'je *et al*., 2019; modified).

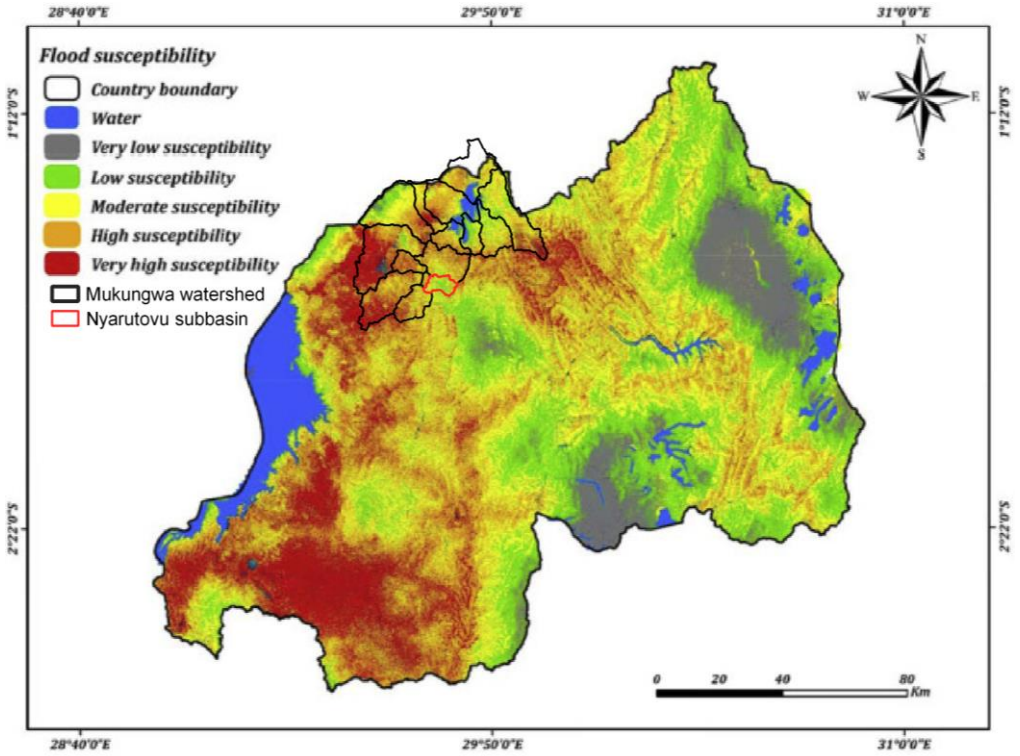

Appendix 3: Soil texture maps for Rwanda, Mukungwa watershed and Nyarutovu subbasin (Karamage *et al*., 2017; modified).

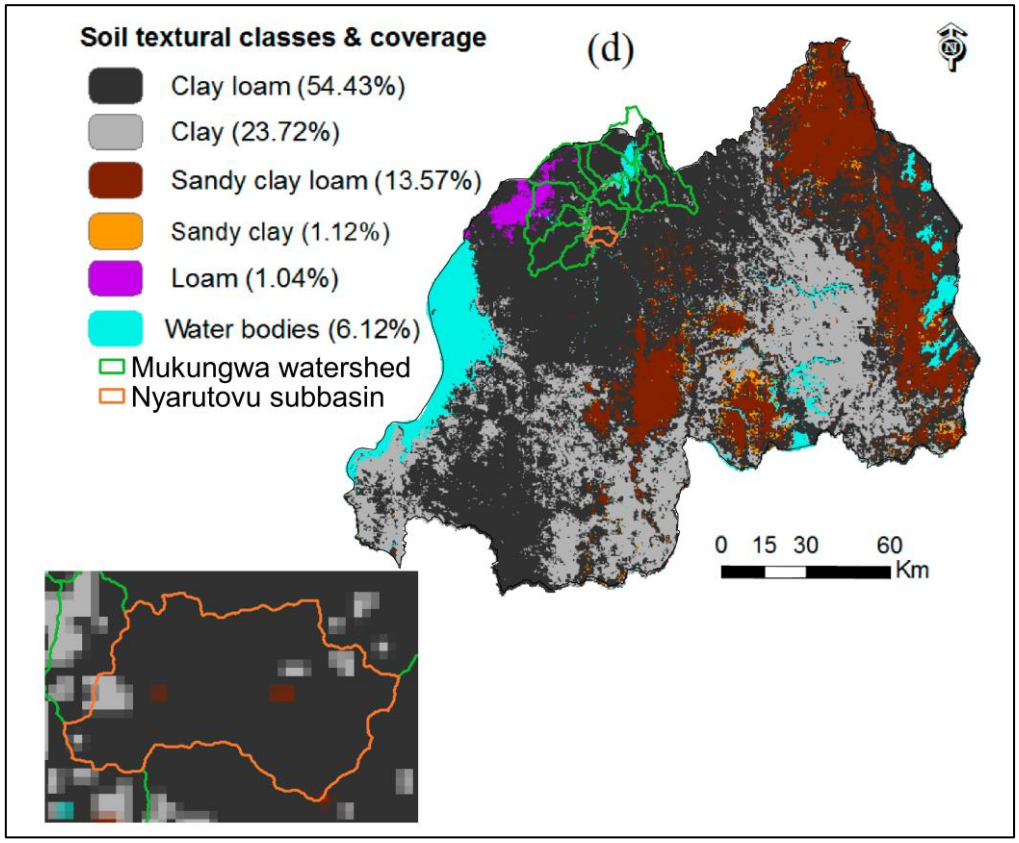

Appendix 4: Soil texture maps for Rwanda, Mukungwa watershed and Nyarutovu subbasin (Li & Mind'je, 2023).

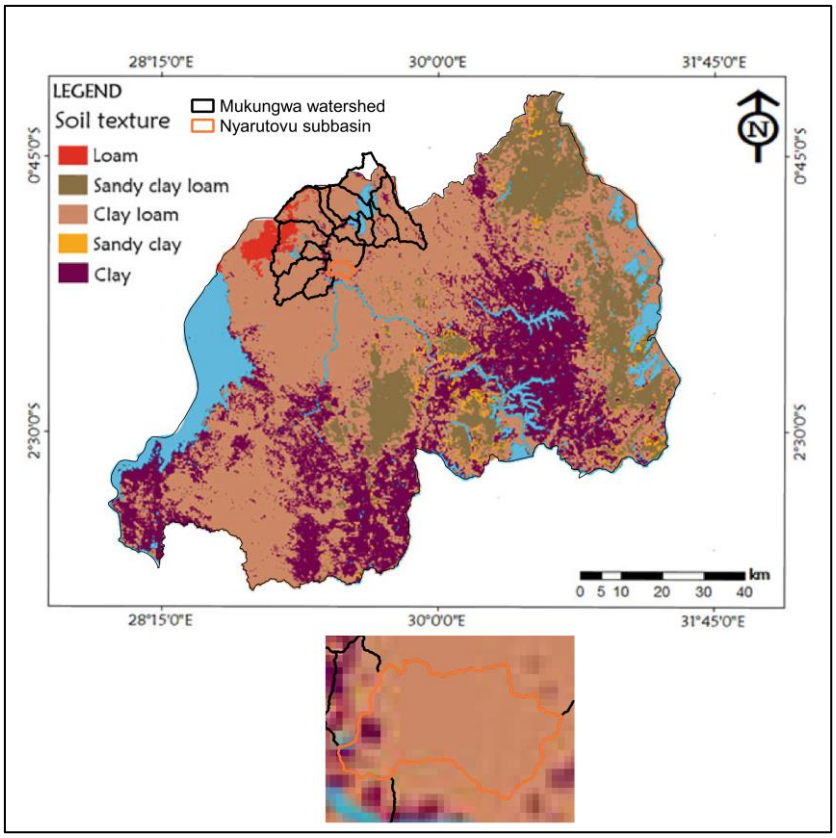

Appendix 5: Calculation of the SCS-CN formula for precipitation excess.

Since

$$\frac{F_a}{S} = \frac{P_e}{P - I_a}$$

$$P = P_e + I_a + F_a \Leftrightarrow F_a = P - P_e - I_a$$

We found:

$$\frac{(P - P_e - I_a)(P - I_a)}{S} = P_e$$

$$\Leftrightarrow \frac{(P - I_a)(P - I_a)}{S} - \frac{P_e(P - I_a)}{S} = P_e$$

$$\Leftrightarrow \frac{(P - I_a)^2}{S} = P_e\left(1 + \left(\frac{P - I_a}{S}\right)\right)$$

$$\Leftrightarrow \frac{(P - I_a)^2}{S\left(1 + \left(\frac{P - I_a}{S}\right)\right)} = P_e$$

$$\Leftrightarrow \frac{(P - I_a)^2}{(P - I_a) + S} = P_e$$

Appendix 6: Curve Number tables of the Technical Release 55 (TR-55) of USDA (1986). (Part 1 of 4)

Table 2-2a Runoff curve numbers for urban areas [1]

Cover description		Curve numbers for hydrologic soil group			
Cover type and hydrologic condition	Average percent impervious area [2]	A	B	C	D
Fully developed urban areas (vegetation established)					
Open space (lawns, parks, golf courses, cemeteries, etc.) [3]:					
Poor condition (grass cover < 50%)		68	79	86	89
Fair condition (grass cover 50% to 75%)		49	69	79	84
Good condition (grass cover > 75%)		39	61	74	80
Impervious areas:					
Paved parking lots, roofs, driveways, etc. (excluding right-of-way)		98	98	98	98
Streets and roads:					
Paved; curbs and storm sewers (excluding right-of-way)		98	98	98	98
Paved; open ditches (including right-of-way)		83	89	92	93
Gravel (including right-of-way)		76	85	89	91
Dirt (including right-of-way)		72	82	87	89
Western desert urban areas:					
Natural desert landscaping (pervious areas only) [4]		63	77	85	88
Artificial desert landscaping (impervious weed barrier, desert shrub with 1- to 2-inch sand or gravel mulch and basin borders)		96	96	96	96
Urban districts:					
Commercial and business	85	89	92	94	95
Industrial	72	81	88	91	93
Residential districts by average lot size:					
1/8 acre or less (town houses)	65	77	85	90	92
1/4 acre	38	61	75	83	87
1/3 acre	30	57	72	81	86
1/2 acre	25	54	70	80	85
1 acre	20	51	68	79	84
2 acres	12	46	65	77	82
Developing urban areas					
Newly graded areas (pervious areas only, no vegetation) [5]		77	86	91	94
Idle lands (CN's are determined using cover types similar to those in table 2-2c).					

[1] Average runoff condition, and $I_a = 0.2S$.

[2] The average percent impervious area shown was used to develop the composite CN's. Other assumptions are as follows: impervious areas are directly connected to the drainage system, impervious areas have a CN of 98, and pervious areas are considered equivalent to open space in good hydrologic condition. CN's for other combinations of conditions may be computed using figure 2-3 or 2-4.

[3] CN's shown are equivalent to those of pasture. Composite CN's may be computed for other combinations of open space cover type.

[4] Composite CN's for natural desert landscaping should be computed using figures 2-3 or 2-4 based on the impervious area percentage (CN = 98) and the pervious area CN. The pervious area CN's are assumed equivalent to desert shrub in poor hydrologic condition.

[5] Composite CN's to use for the design of temporary measures during grading and construction should be computed using figure 2-3 or 2-4 based on the degree of development (impervious area percentage) and the CN's for the newly graded pervious areas.

Appendix 7: Curve Number tables of the Technical Release 55 (TR-55) of USDA (1986). (Part 2 of 4)

Table 2-2b Runoff curve numbers for cultivated agricultural lands [1]

Cover description			Curve numbers for hydrologic soil group			
Cover type	Treatment [2]	Hydrologic condition [3]	A	B	C	D
Fallow	Bare soil	—	77	86	91	94
	Crop residue cover (CR)	Poor	76	85	90	93
		Good	74	83	88	90
Row crops	Straight row (SR)	Poor	72	81	88	91
		Good	67	78	85	89
	SR + CR	Poor	71	80	87	90
		Good	64	75	82	85
	Contoured (C)	Poor	70	79	84	88
		Good	65	75	82	86
	C + CR	Poor	69	78	83	87
		Good	64	74	81	85
	Contoured & terraced (C&T)	Poor	66	74	80	82
		Good	62	71	78	81
	C&T+ CR	Poor	65	73	79	81
		Good	61	70	77	80
Small grain	SR	Poor	65	76	84	88
		Good	63	75	83	87
	SR + CR	Poor	64	75	83	86
		Good	60	72	80	84
	C	Poor	63	74	82	85
		Good	61	73	81	84
	C + CR	Poor	62	73	81	84
		Good	60	72	80	83
	C&T	Poor	61	72	79	82
		Good	59	70	78	81
	C&T+ CR	Poor	60	71	78	81
		Good	58	69	77	80
Close-seeded or broadcast legumes or rotation meadow	SR	Poor	66	77	85	89
		Good	58	72	81	85
	C	Poor	64	75	83	85
		Good	55	69	78	83
	C&T	Poor	63	73	80	83
		Good	51	67	76	80

[1] Average runoff condition, and I_a=0.2S

[2] Crop residue cover applies only if residue is on at least 5% of the surface throughout the year.

[3] Hydraulic condition is based on combination factors that affect infiltration and runoff, including (a) density and canopy of vegetative areas, (b) amount of year-round cover, (c) amount of grass or close-seeded legumes, (d) percent of residue cover on the land surface (good ≥ 20%), and (e) degree of surface roughness.

Poor: Factors impair infiltration and tend to increase runoff.

Good: Factors encourage average and better than average infiltration and tend to decrease runoff.

Appendix 8: Curve Number tables of the Technical Release 55 (TR-55) of USDA (1986). (Part 3 of 4)

Table 2-2c Runoff curve numbers for other agricultural lands [1]

Cover description		Curve numbers for hydrologic soil group			
Cover type	Hydrologic condition	A	B	C	D
Pasture, grassland, or range—continuous forage for grazing. [2]	Poor	68	79	86	89
	Fair	49	69	79	84
	Good	39	61	74	80
Meadow—continuous grass, protected from grazing and generally mowed for hay.	—	30	58	71	78
Brush—brush-weed-grass mixture with brush the major element. [3]	Poor	48	67	77	83
	Fair	35	56	70	77
	Good	30 [4]	48	65	73
Woods—grass combination (orchard or tree farm). [5]	Poor	57	73	82	86
	Fair	43	65	76	82
	Good	32	58	72	79
Woods. [6]	Poor	45	66	77	83
	Fair	36	60	73	79
	Good	30 [4]	55	70	77
Farmsteads—buildings, lanes, driveways, and surrounding lots.	—	59	74	82	86

1 Average runoff condition, and $I_a = 0.2S$.

2 ***Poor:*** <50%) ground cover or heavily grazed with no mulch.
Fair: 50 to 75% ground cover and not heavily grazed.
Good: > 75% ground cover and lightly or only occasionally grazed.

3 ***Poor:*** <50% ground cover.
Fair: 50 to 75% ground cover.
Good: >75% ground cover.

4 Actual curve number is less than 30; use CN = 30 for runoff computations.

5 CN's shown were computed for areas with 50% woods and 50% grass (pasture) cover. Other combinations of conditions may be computed from the CN's for woods and pasture.

6 ***Poor:*** Forest litter, small trees, and brush are destroyed by heavy grazing or regular burning.
Fair: Woods are grazed but not burned, and some forest litter covers the soil.
Good: Woods are protected from grazing, and litter and brush adequately cover the soil.

Appendix 9: Curve Number tables of the Technical Release 55 (TR-55) of USDA (1986). (Part 4 of 4)

Table 2-2d Runoff curve numbers for arid and semiarid rangelands [1/]

Cover description		Curve numbers for hydrologic soil group			
Cover type	Hydrologic condition [2/]	A [3/]	B	C	D
Herbaceous—mixture of grass, weeds, and low-growing brush, with brush the minor element.	Poor		80	87	93
	Fair		71	81	89
	Good		62	74	85
Oak-aspen—mountain brush mixture of oak brush, aspen, mountain mahogany, bitter brush, maple, and other brush.	Poor		66	74	79
	Fair		48	57	63
	Good		30	41	48
Pinyon-juniper—pinyon, juniper, or both; grass understory.	Poor		75	85	89
	Fair		58	73	80
	Good		41	61	71
Sagebrush with grass understory.	Poor		67	80	85
	Fair		51	63	70
	Good		35	47	55
Desert shrub—major plants include saltbush, greasewood, creosotebush, blackbrush, bursage, palo verde, mesquite, and cactus.	Poor	63	77	85	88
	Fair	55	72	81	86
	Good	49	68	79	84

1 Average runoff condition, and I_a = 0.2S. For range in humid regions, use table 2-2c.
2 Poor: <30% ground cover (litter, grass, and brush overstory).
Fair: 30 to 70% ground cover.
Good: > 70% ground cover.
3 Curve numbers for group A have been developed only for desert shrub.

Appendix 10: Green and Ampt infiltration parameters for various soil classes (Chow *et al.*, 1988; based on Rawls *et al.*, 1983).

Green-Ampt infiltration parameters for various soil classes

Soil class	Porosity η	Effective porosity θ_e	Wetting front soil suction head ψ (cm)	Hydraulic conductivity K (cm/h)
Sand	0.437 (0.374–0.500)	0.417 (0.354–0.480)	4.95 (0.97–25.36)	11.78
Loamy sand	0.437 (0.363–0.506)	0.401 (0.329–0.473)	6.13 (1.35–27.94)	2.99
Sandy loam	0.453 (0.351–0.555)	0.412 (0.283–0.541)	11.01 (2.67–45.47)	1.09
Loam	0.463 (0.375–0.551)	0.434 (0.334–0.534)	8.89 (1.33–59.38)	0.34
Silt loam	0.501 (0.420–0.582)	0.486 (0.394–0.578)	16.68 (2.92–95.39)	0.65
Sandy clay loam	0.398 (0.332–0.464)	0.330 (0.235–0.425)	21.85 (4.42–108.0)	0.15
Clay loam	0.464 (0.409–0.519)	0.309 (0.279–0.501)	20.88 (4.79–91.10)	0.10
Silty clay loam	0.471 (0.418–0.524)	0.432 (0.347–0.517)	27.30 (5.67–131.50)	0.10
Sandy clay	0.430 (0.370–0.490)	0.321 (0.207–0.435)	23.90 (4.08–140.2)	0.06
Silty clay	0.479 (0.425–0.533)	0.423 (0.334–0.512)	29.22 (6.13–139.4)	0.05
Clay	0.475 (0.427–0.523)	0.385 (0.269–0.501)	31.63 (6.39–156.5)	0.03

The numbers in parentheses below each parameter are one standard deviation around the parameter value given. *Source:* Rawls, Brakensiek, and Miller, 1983.

Appendix 11: Illustration of the influence of Peak Rate Factor (PRF) variation (Młyński *et al.*, 2020). Note that NRCS-UH is another way of calling the SCS-UH method.

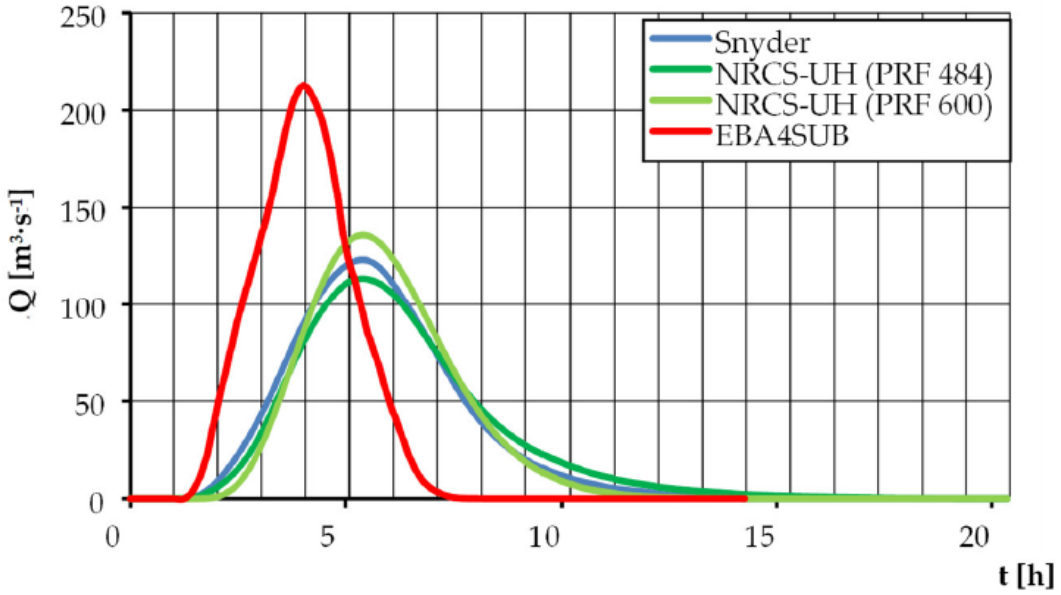

Appendix 12: HEC-HMS simulations of the March 31, 2023 event with the parameters found in the literature.

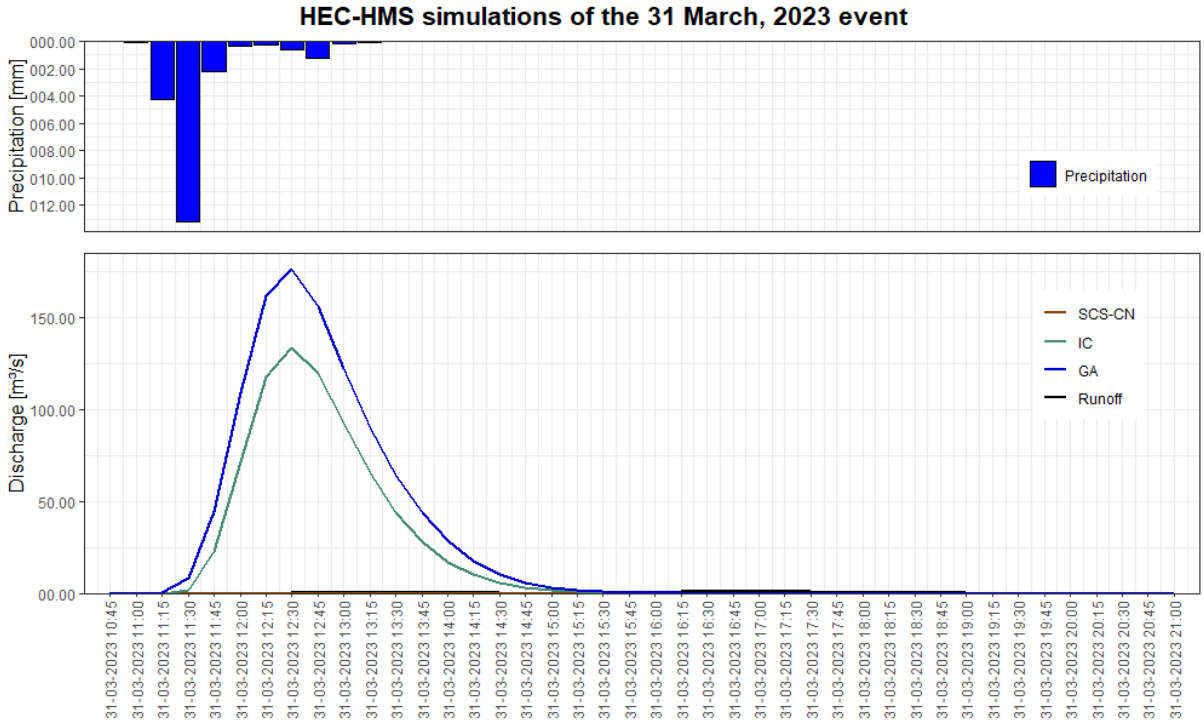

Appendix 13: HEC-HMS simulations of the April 15-16, 2023 event with the parameters found in the literature.

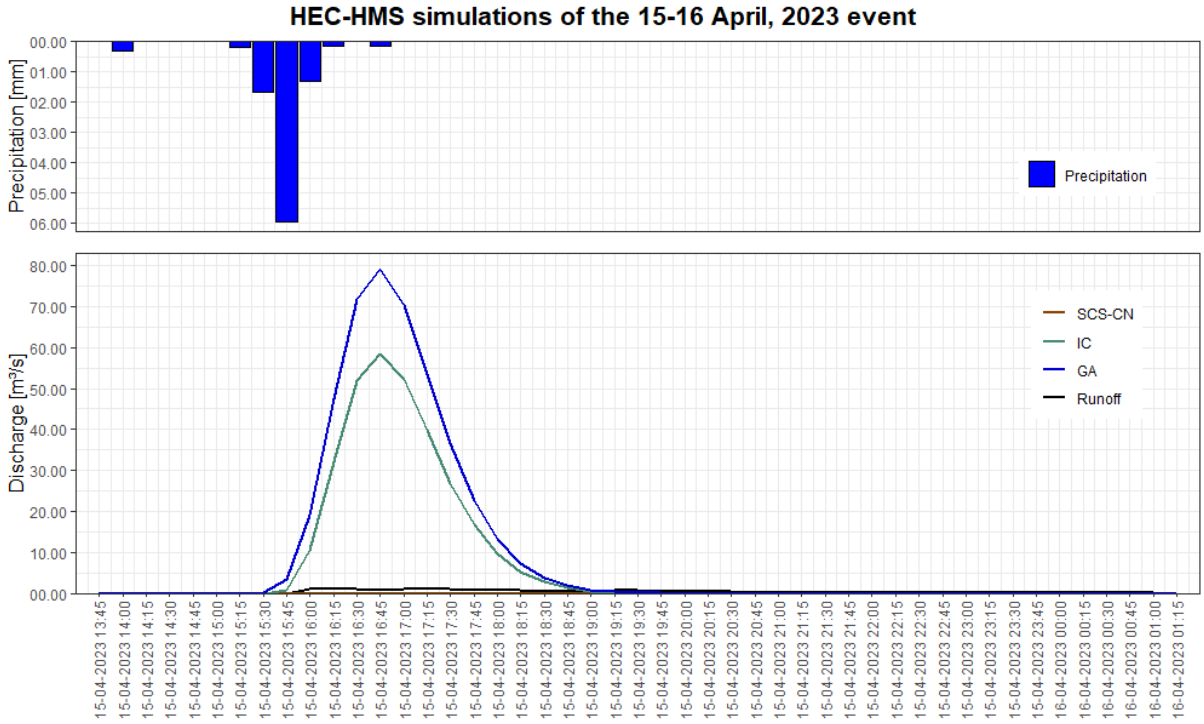

Appendix 14: HEC-HMS simulations of the April 16-17, 2023 event with the parameters found in the literature.

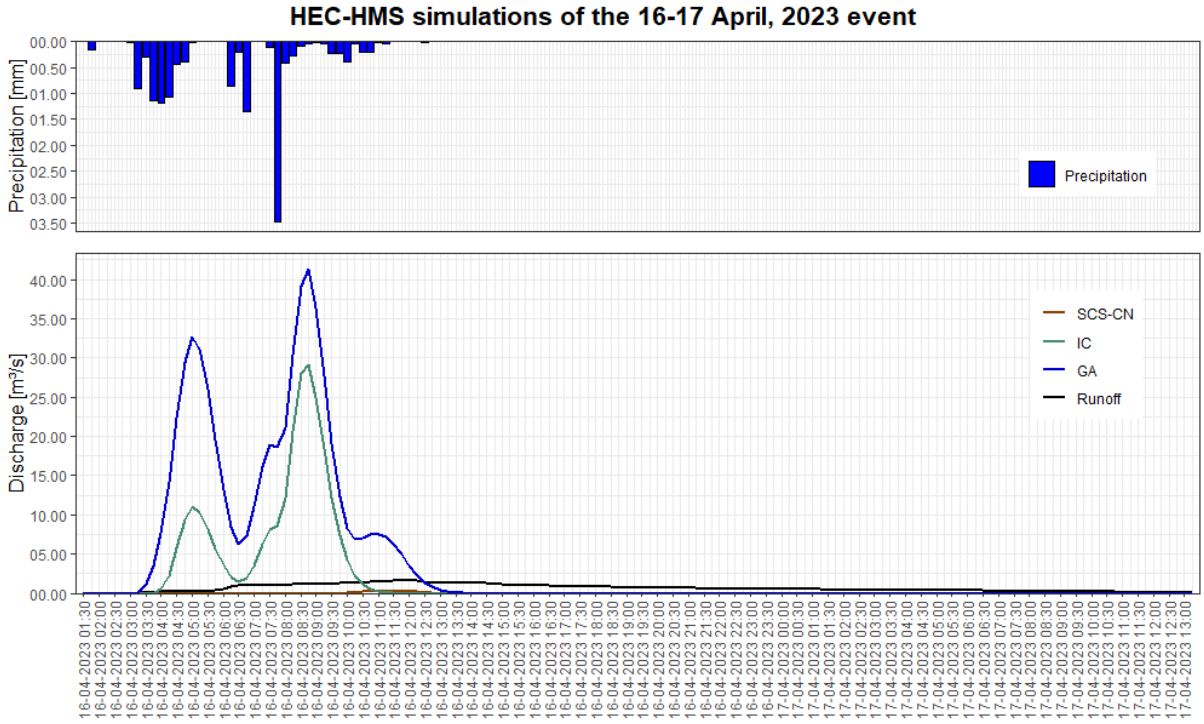

Appendix 15: HEC-HMS simulation of the April 16-17, 2023 event with the parameters found in the literature. Zoom on the SCS-CN method.

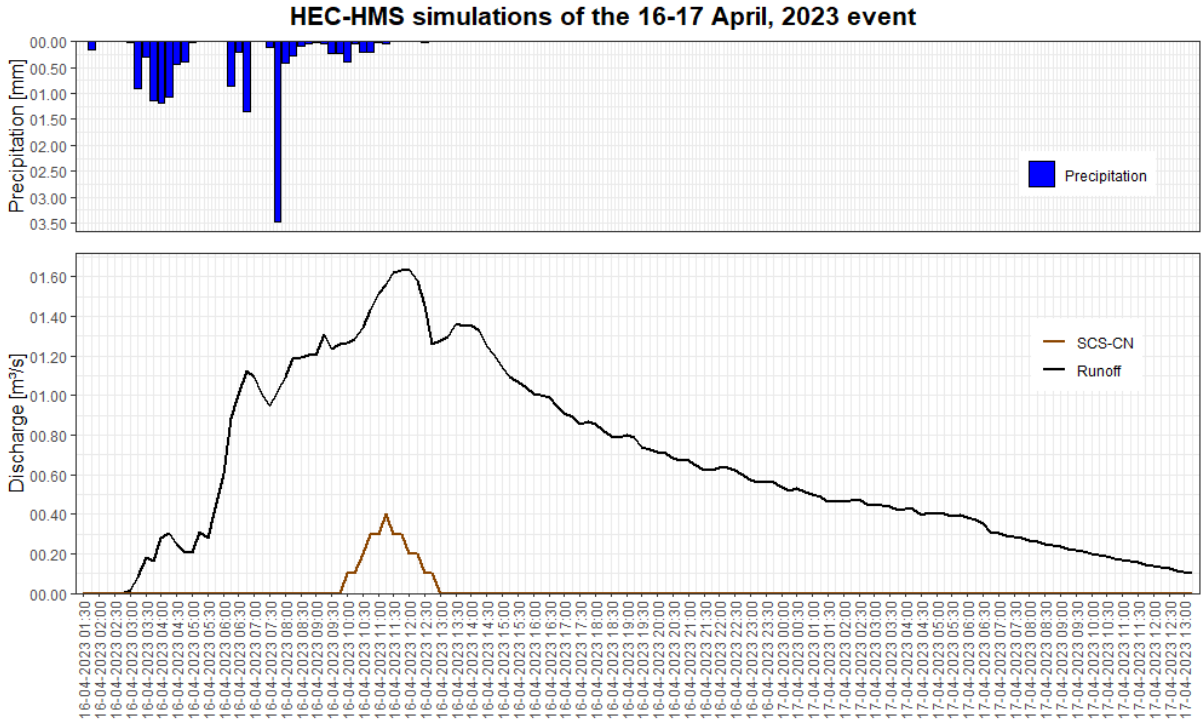

Appendix 16: HEC-HMS simulations of the April 18-20, 2023 event with the parameters found in the literature.

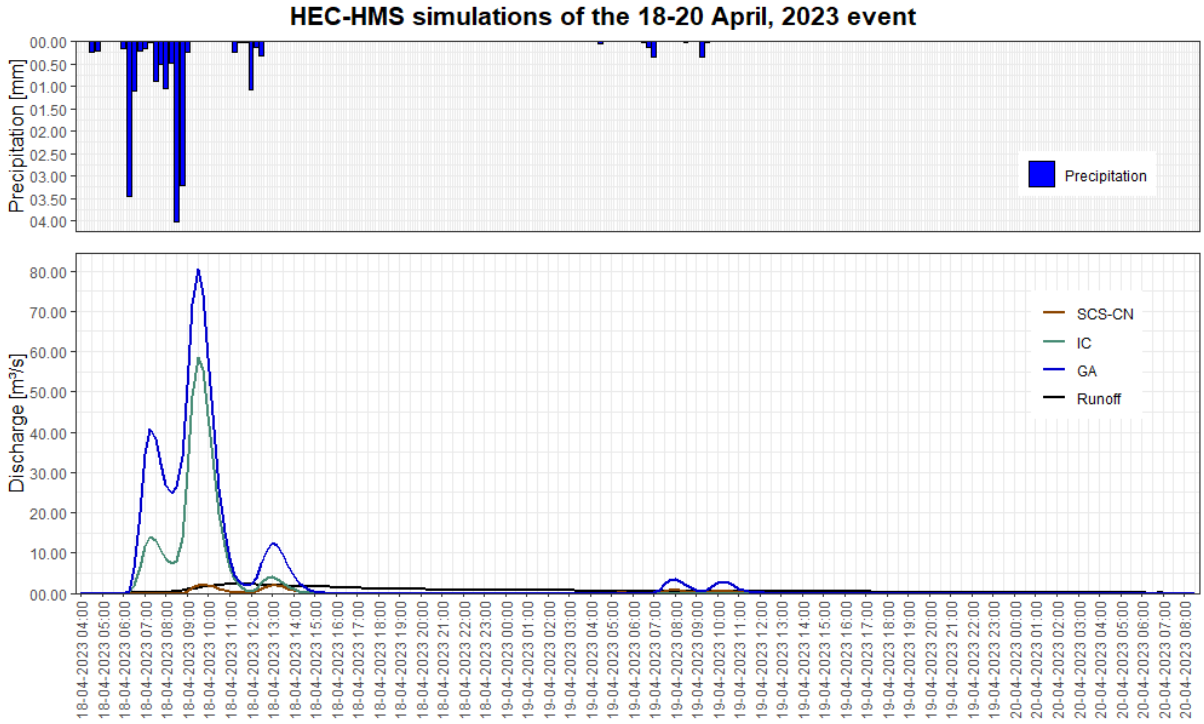

Appendix 17: HEC-HMS simulation of the April 18-20, 2023 event with the parameters found in the literature. Zoom the SCS-CN method. Zoom on the SCS-CN method.

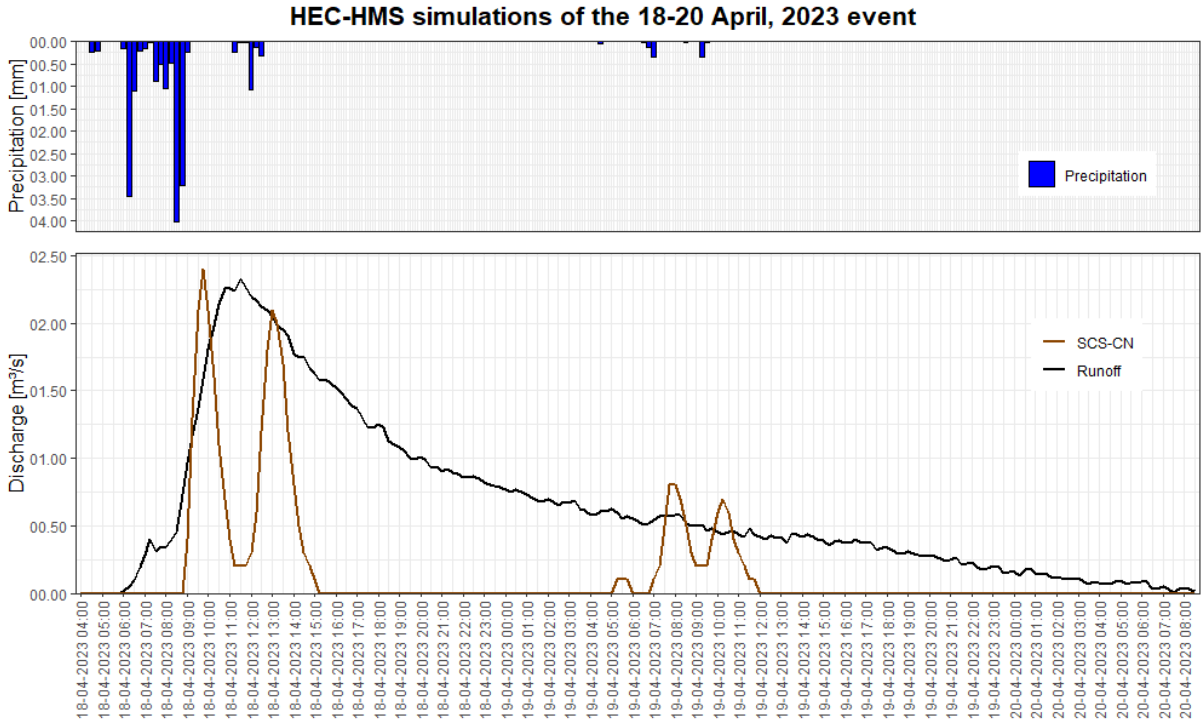

Appendix 18: HEC-HMS simulations of the (1) April 23-24, 2023 event with the parameters found in the literature.

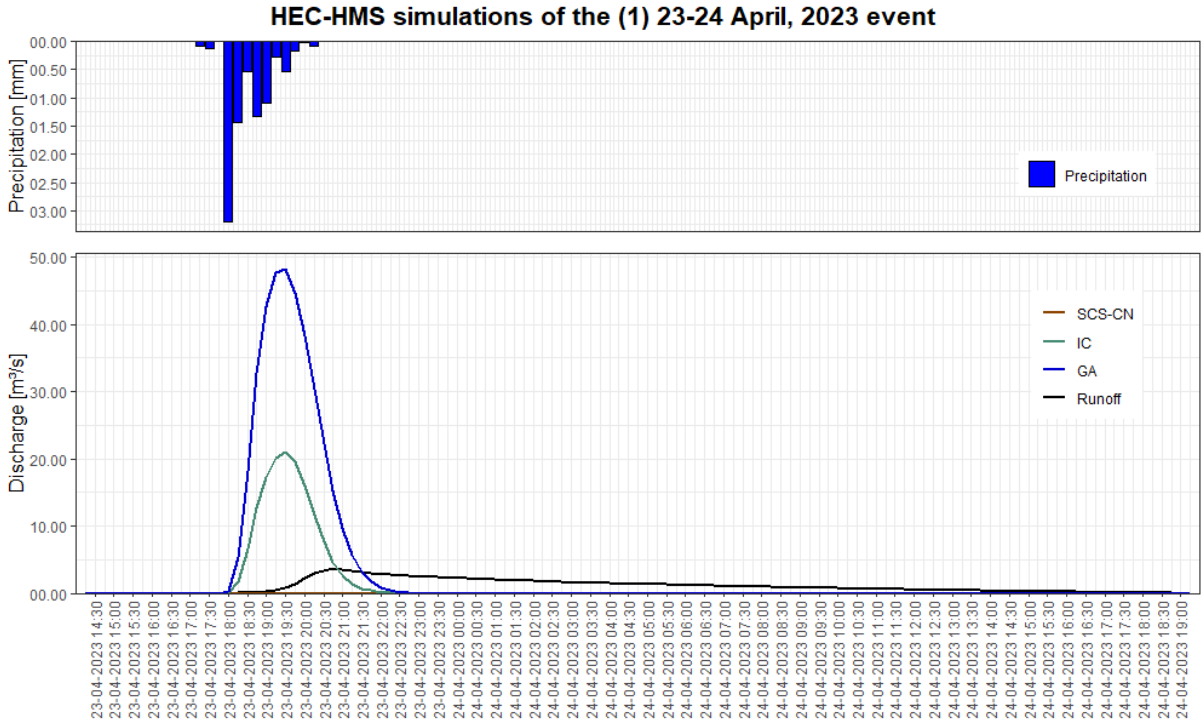

Appendix 19: HEC-HMS simulations of the (2) April 23-24, 2023 event with the parameters found in the literature.

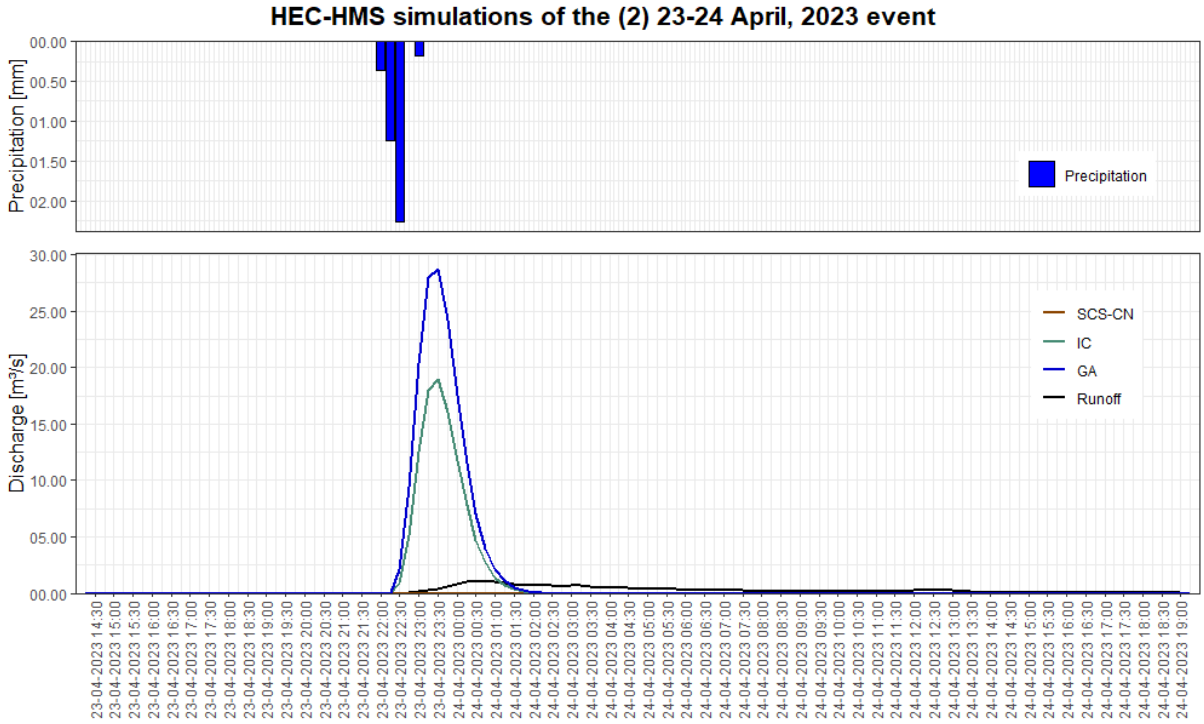

Appendix 20: HEC-HMS simulations of the (1) April 28-29, 2023 event with the parameters found in the literature.

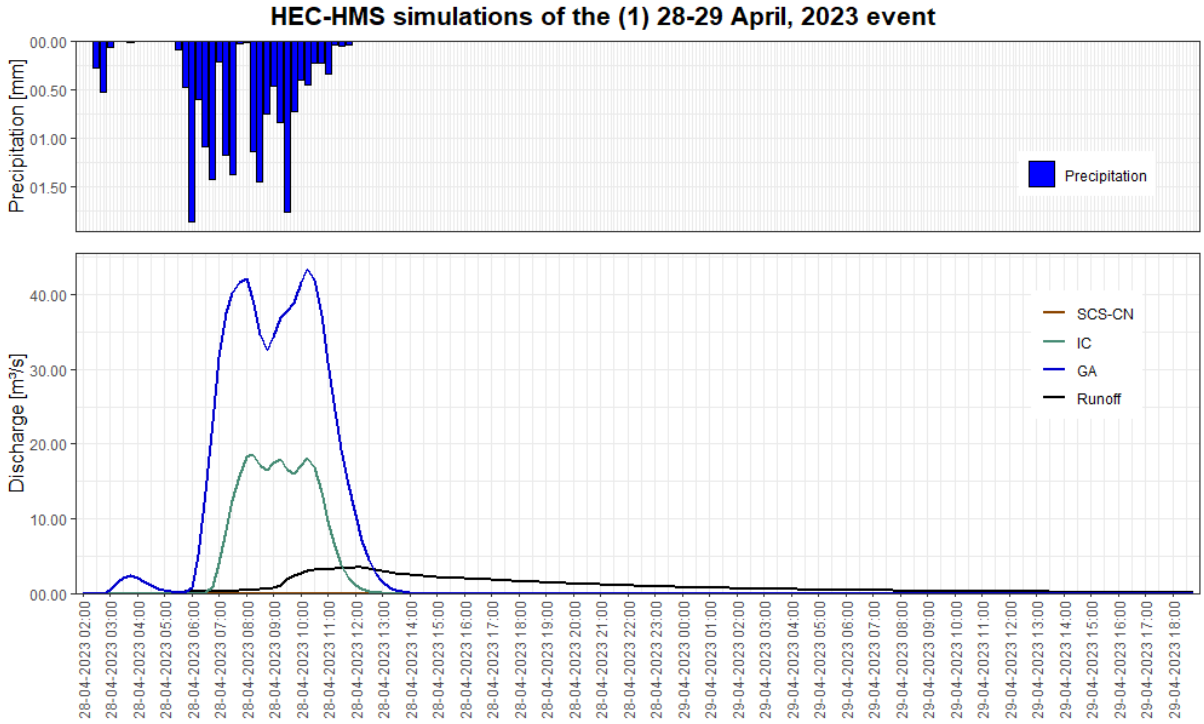

Appendix 21: HEC-HMS simulations of the (2) April 28-29, 2023 event with the parameters found in the literature.

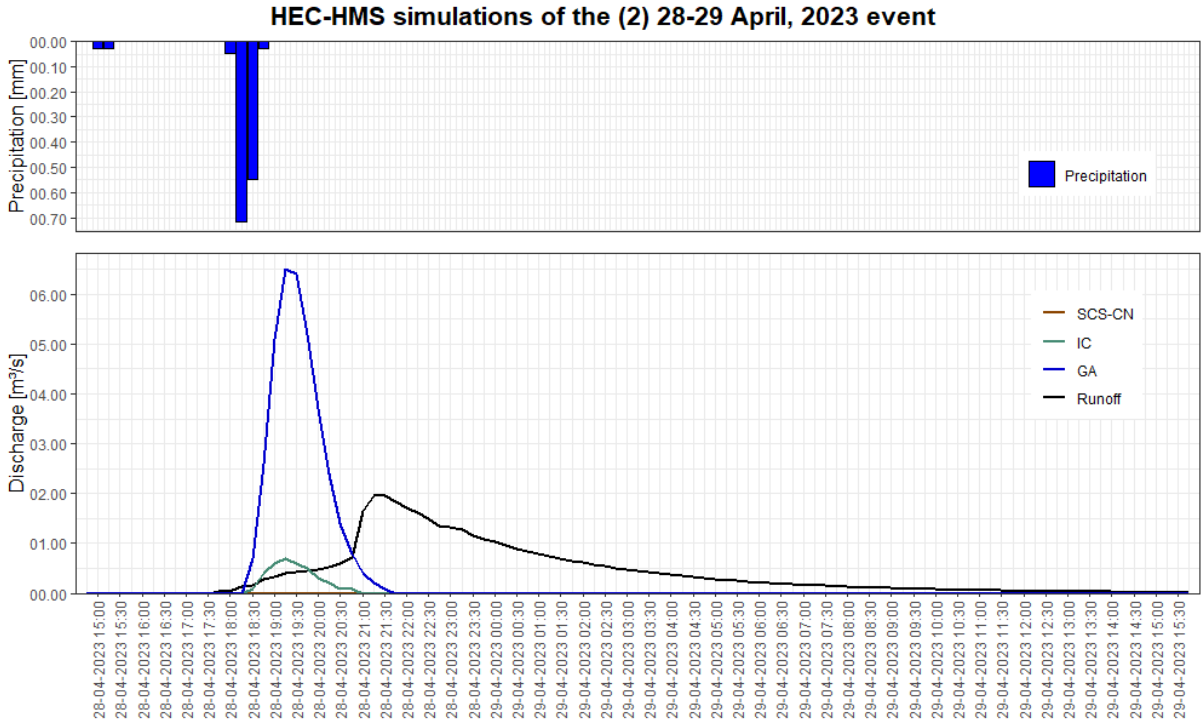

Appendix 22: HEC-HMS simulations of the April 29-30, 2023 event with the parameters found in the literature.

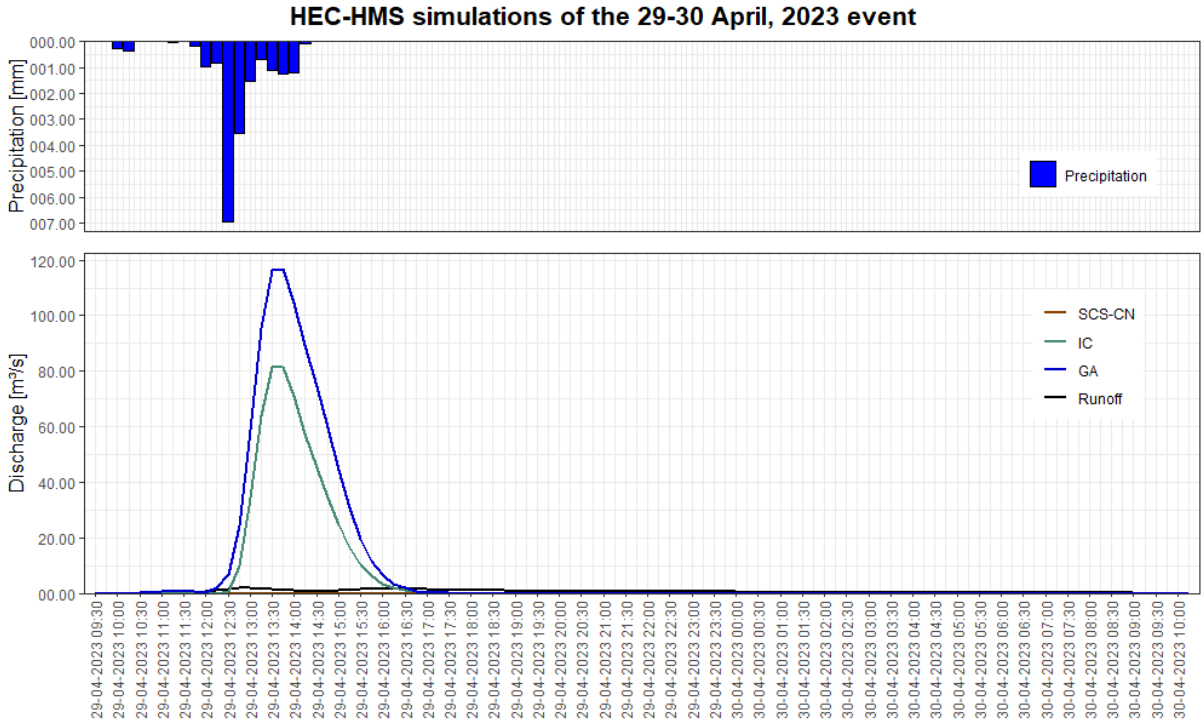

Appendix 23: HEC-HMS simulations of the April 30 – 02 May, 2023 event with the parameters found in the literature.

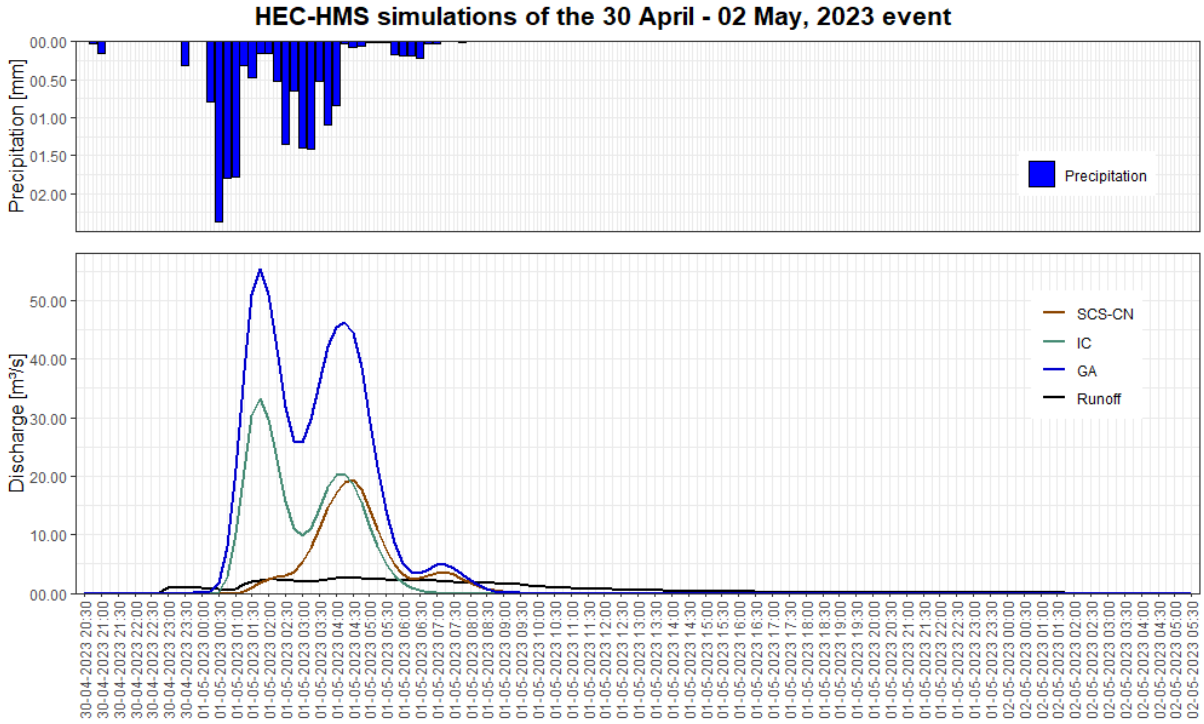

Appendix 24: HEC-HMS simulations of the 01-03 May, 2023 event with the parameters found in the literature.

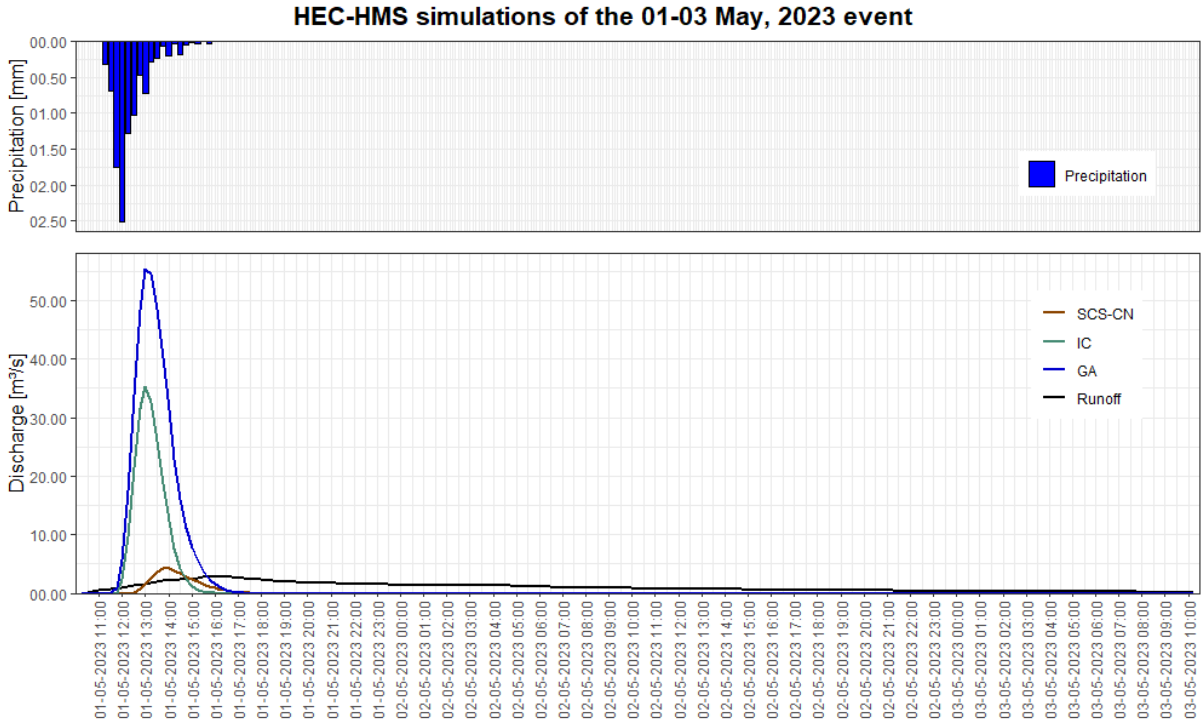

Appendix 25: HEC-HMS simulation of the 01-03 May, 2023 event with the parameters found in the literature. Zoom on the SCS-CN method.

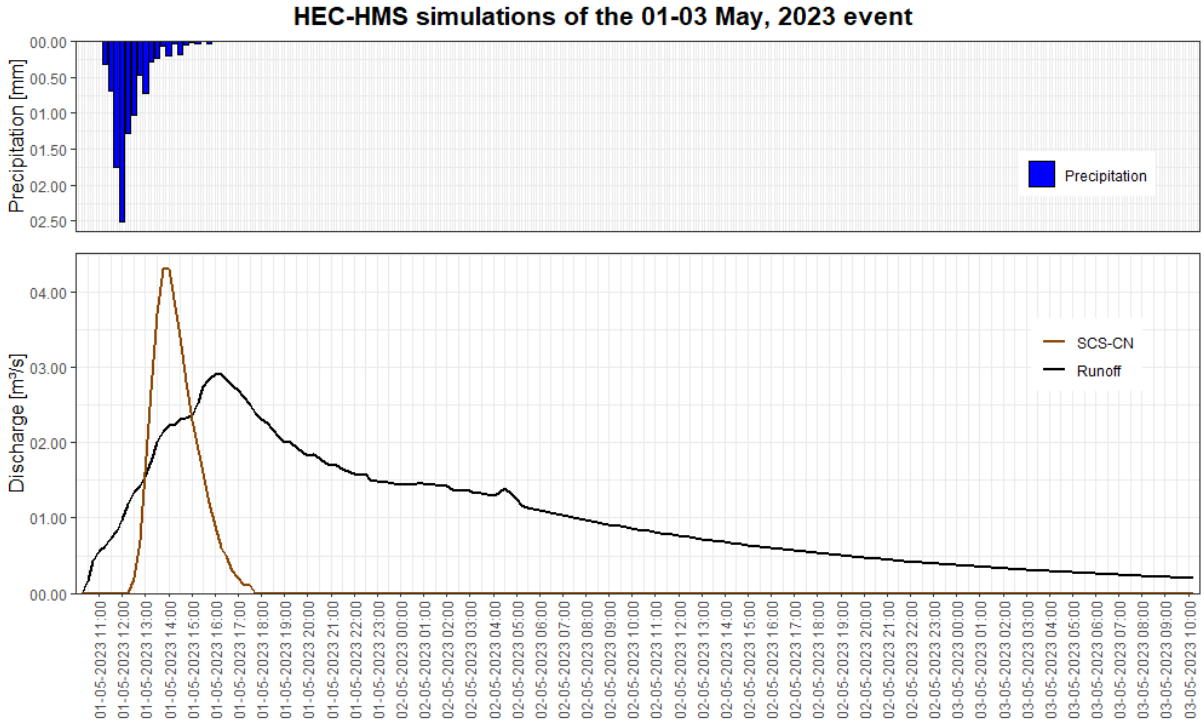

Appendix 26: HEC-HMS simulations of the 02-03 May, 2023 event with the parameters found in the literature.

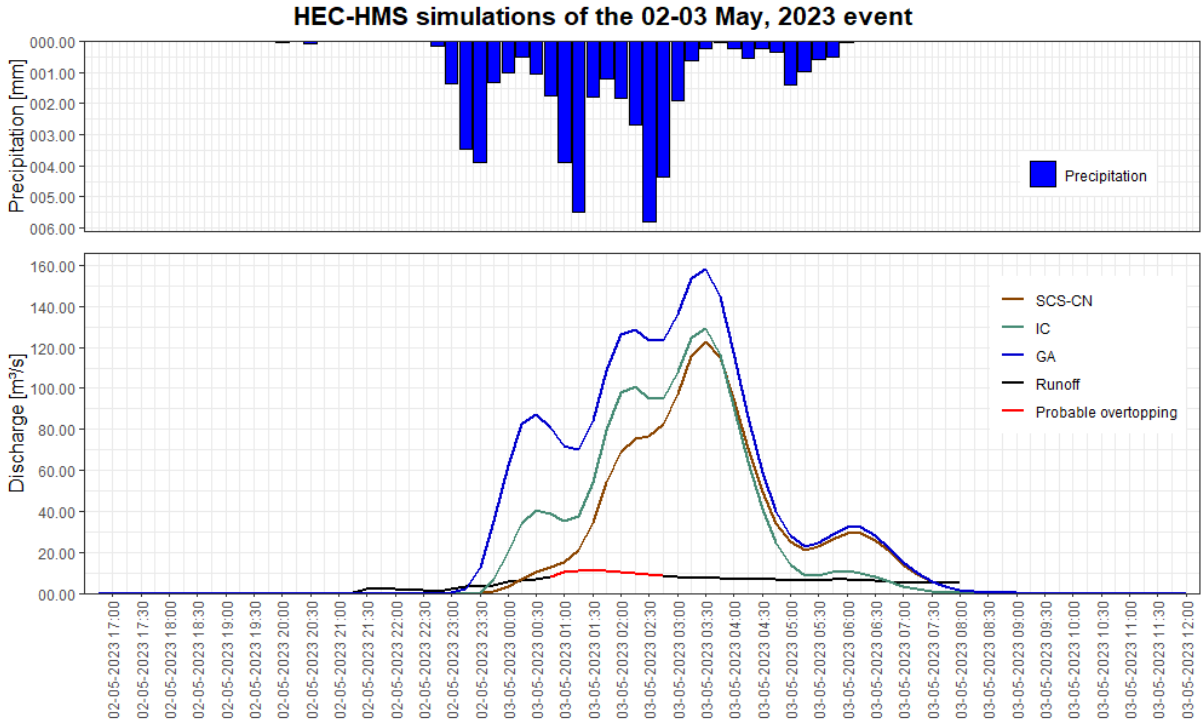

Appendix 27: HEC-HMS calibrations of the loss method parameters for the March 31, 2023 event.

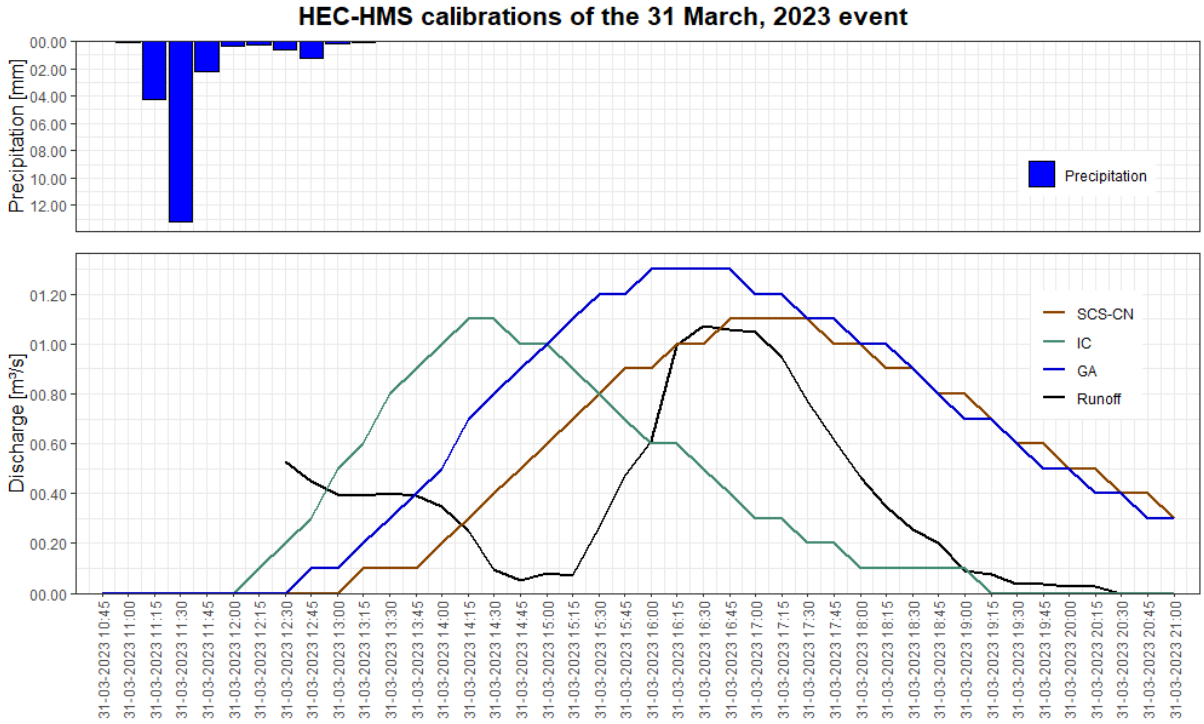

Appendix 28: HEC-HMS calibrations of the loss method parameters for the April 02-03, 2023 event.

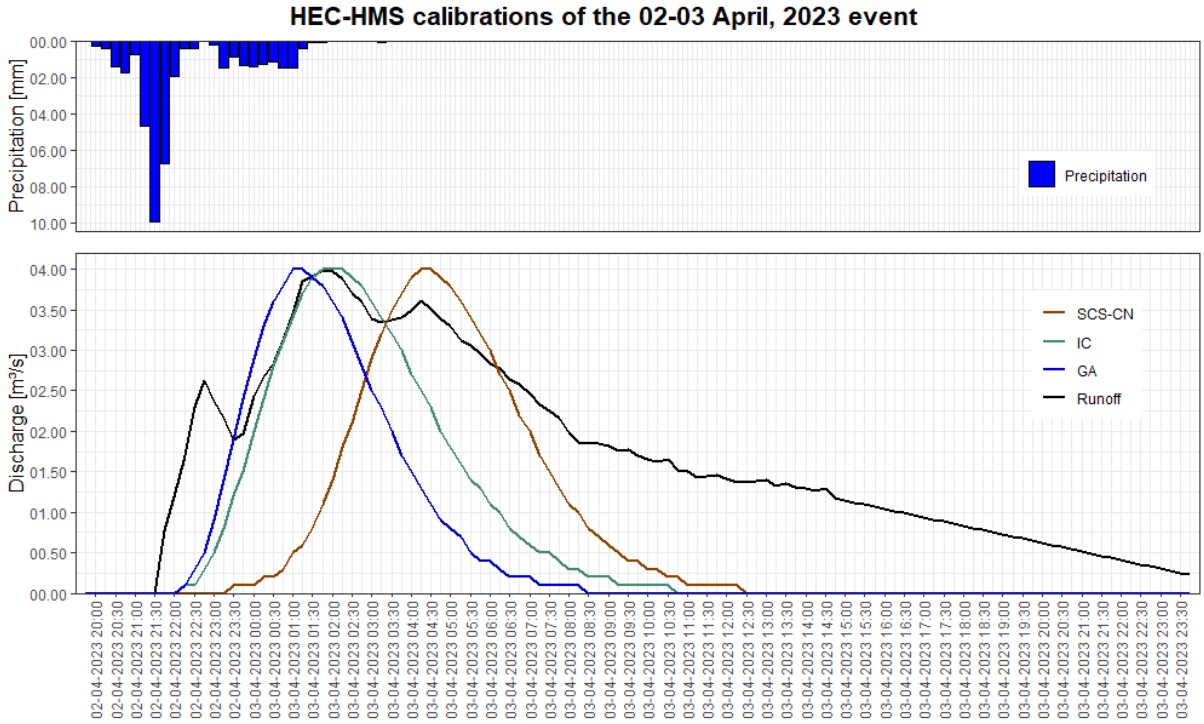

Appendix 29: HEC-HMS calibrations of the loss method parameters for the April 15-16, 2023 event.

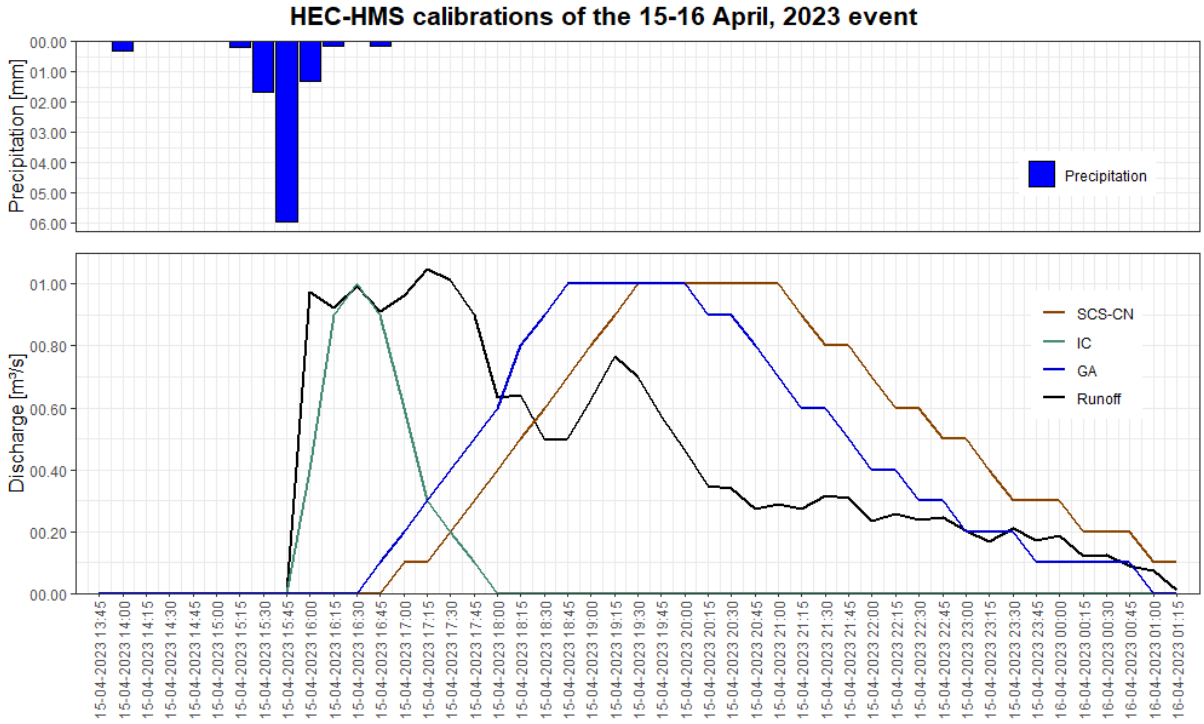

Appendix 30: HEC-HMS calibrations of the loss method parameters for the April 16-17, 2023 event.

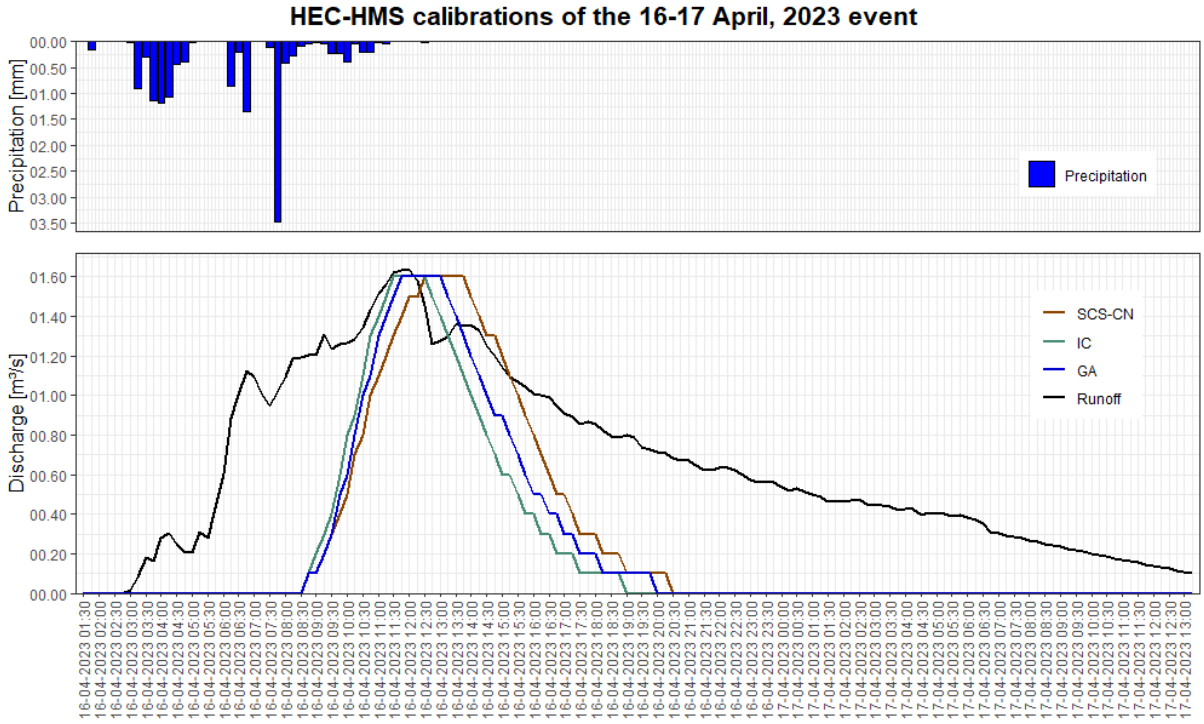

Appendix 31: HEC-HMS calibrations of the loss method parameters for the April 18-20, 2023 event.

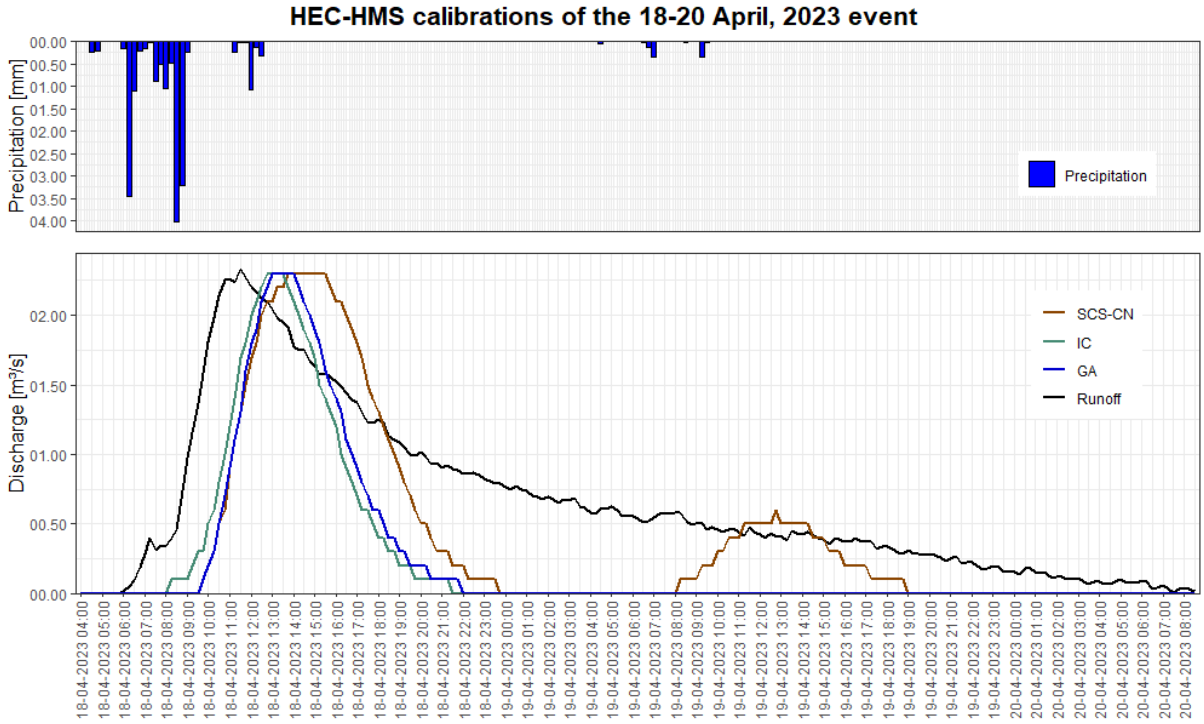

Appendix 32: HEC-HMS calibrations of the loss method parameters for the (1) April 23-24, 2023 event.

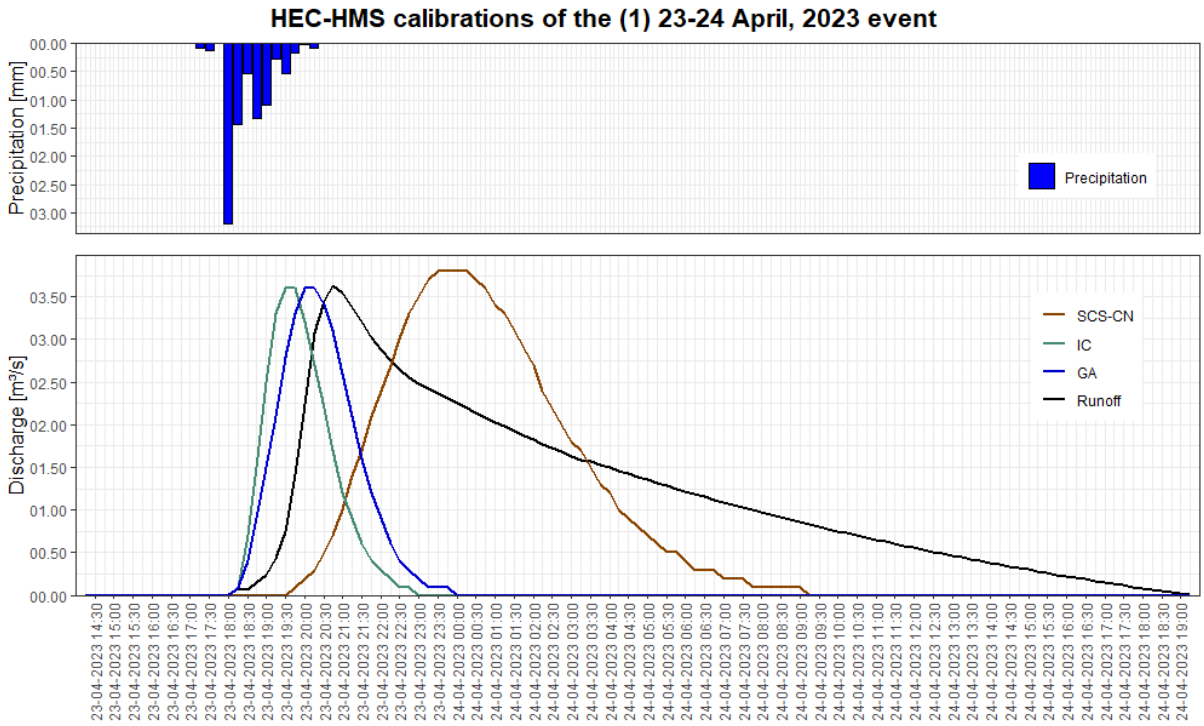

Appendix 33: HEC-HMS calibrations of the loss method parameters for the (2) April 23-24, 2023 event.

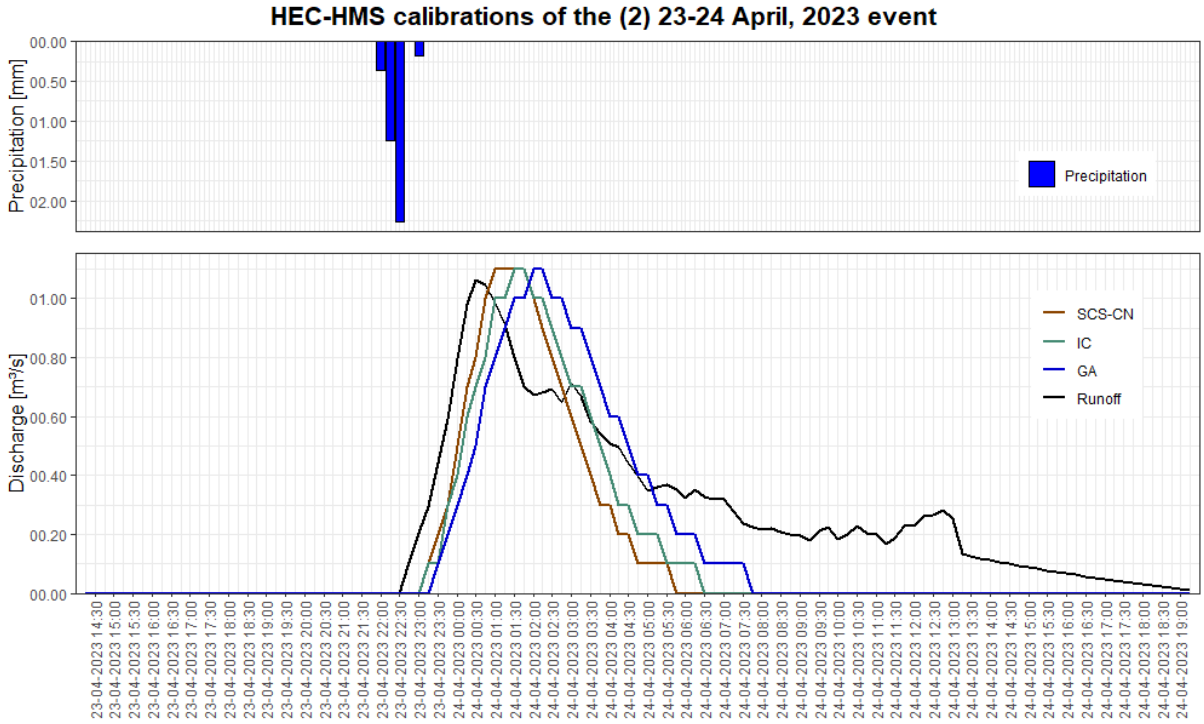

Appendix 34: HEC-HMS calibrations of the loss method parameters for the (1) April 28-29, 2023 event.

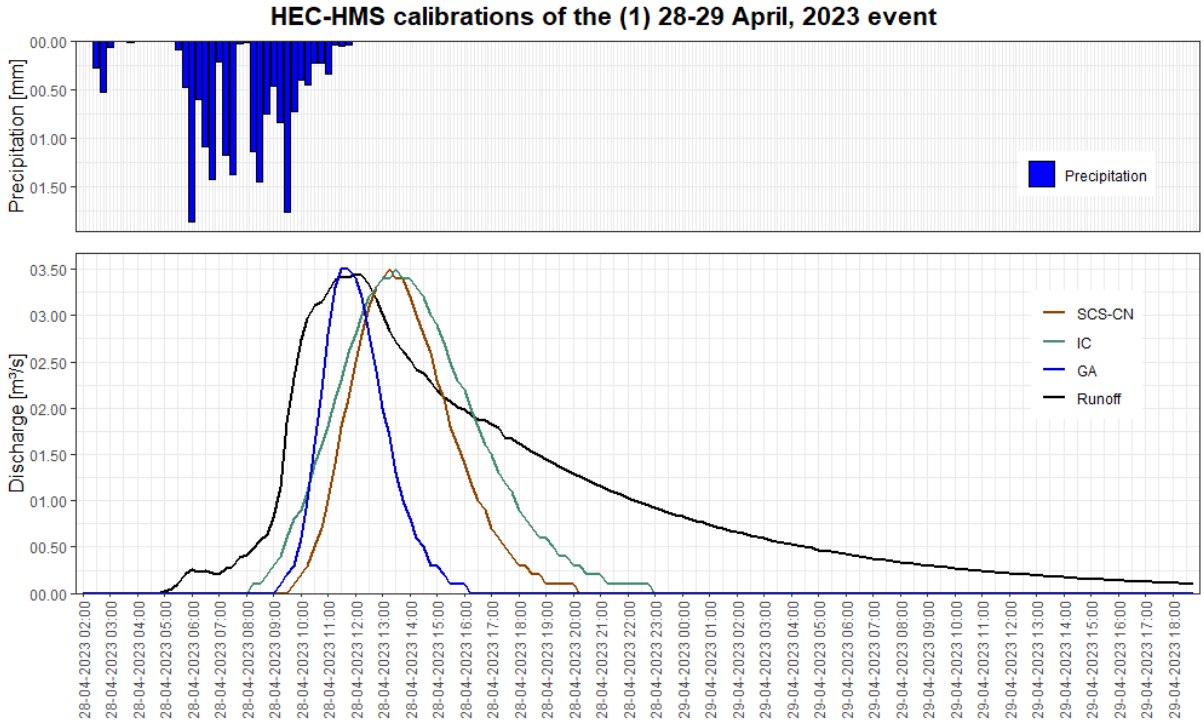

Appendix 35: HEC-HMS calibrations of the loss method parameters for the (2) April 28-29, 2023 event.

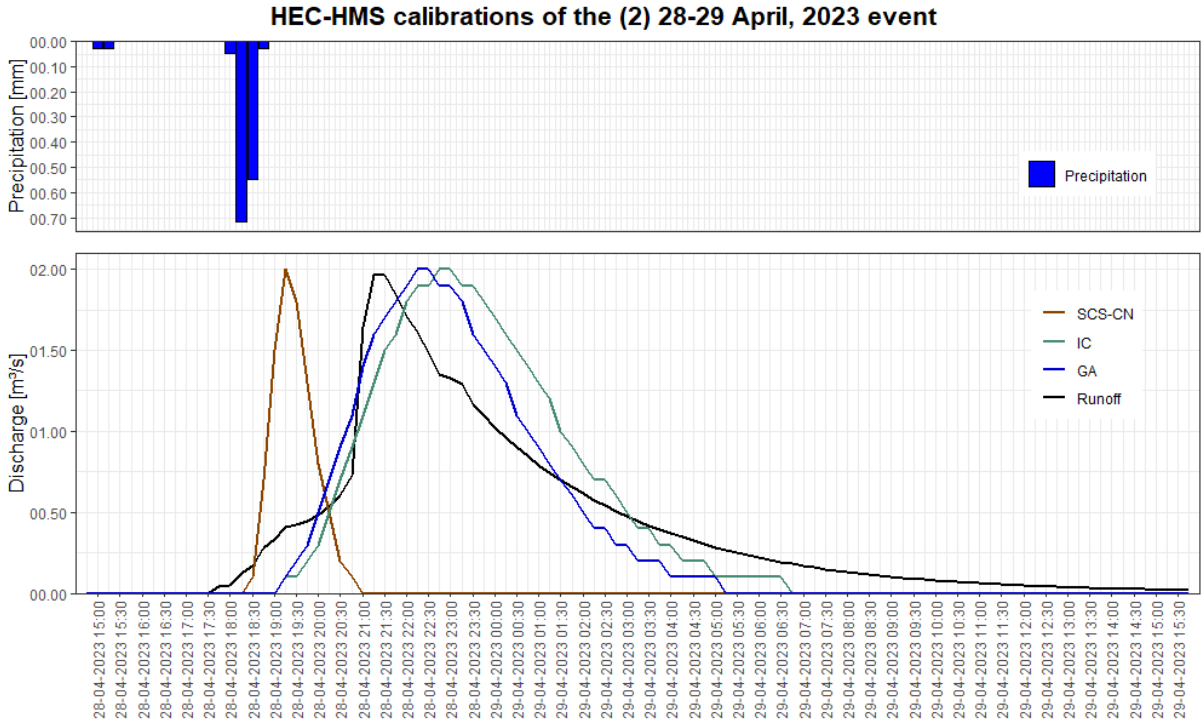

Appendix 36: HEC-HMS calibrations of the loss method parameters for the April 29-30, 2023 event.

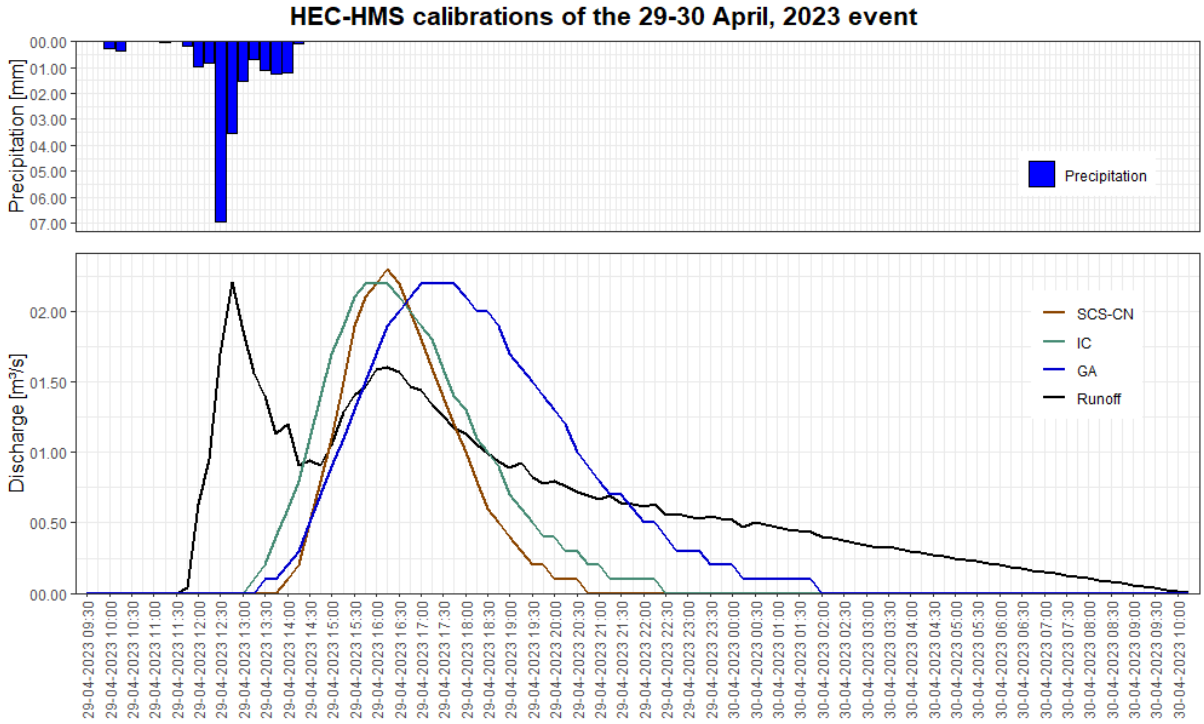

Appendix 37: HEC-HMS calibrations of the loss method parameters for the April 30 – May 02, 2023 event.

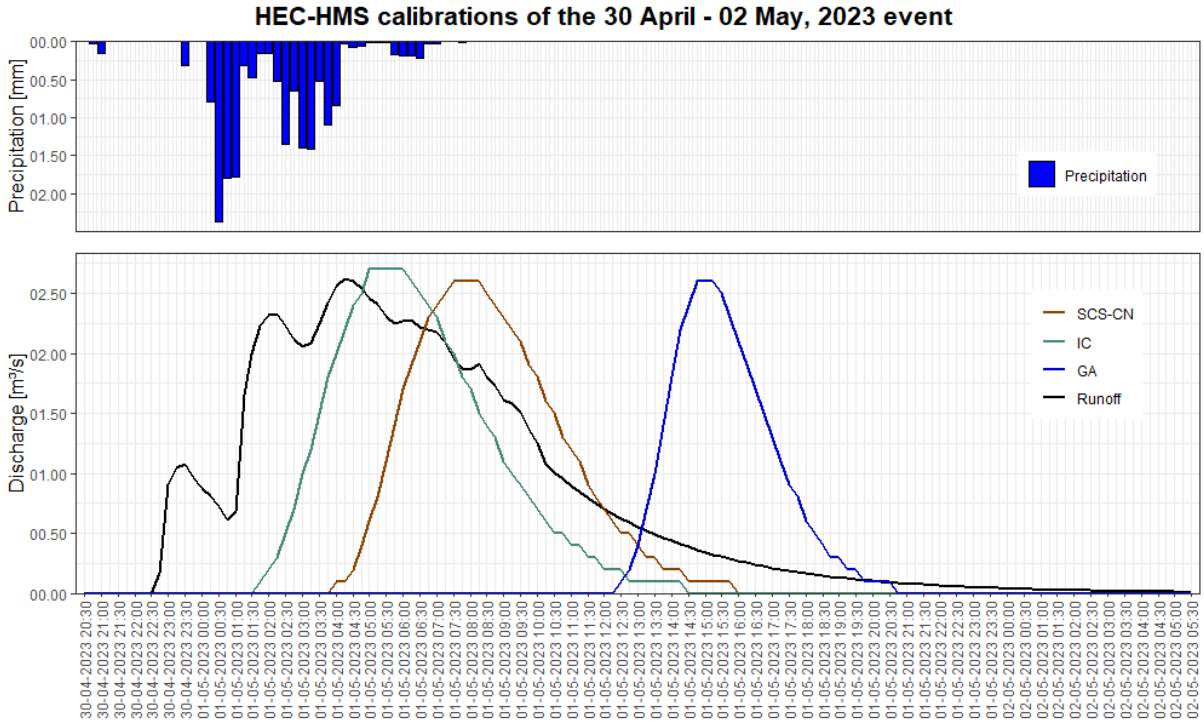

Appendix 38: HEC-HMS calibrations of the loss method parameters for the May 01-03, 2023 event.

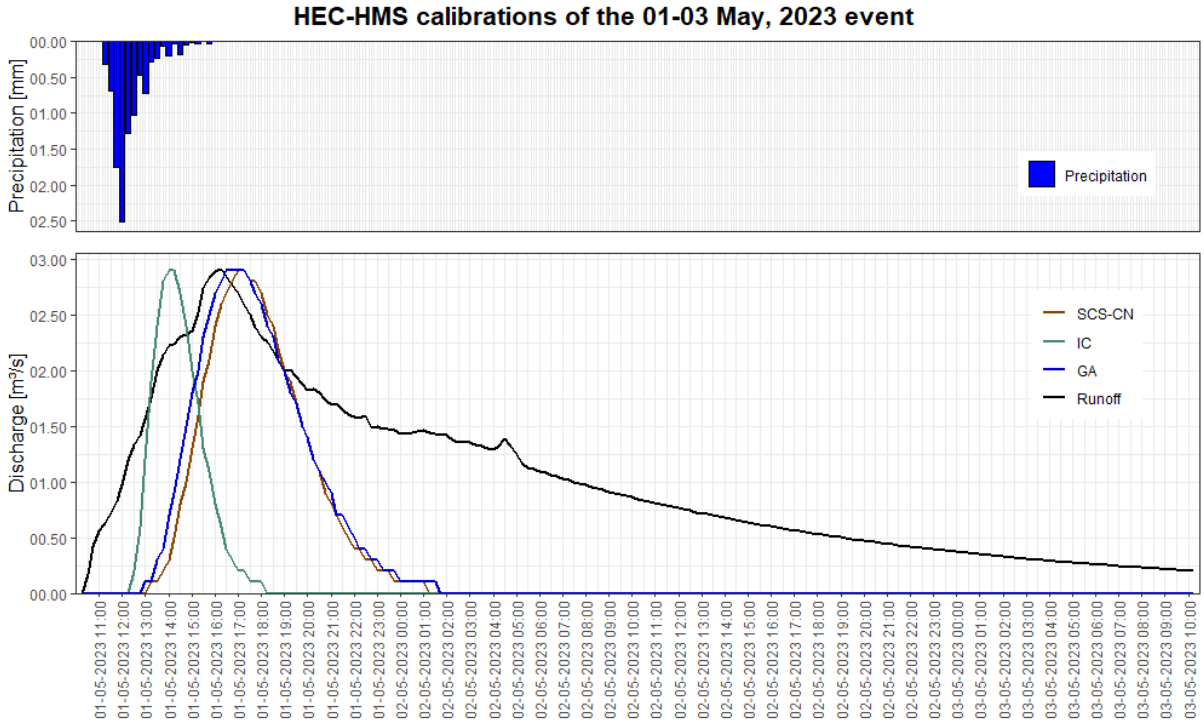

Appendix 39: HEC-HMS simulations of the March 31, 2023 event with the optimized parameters.

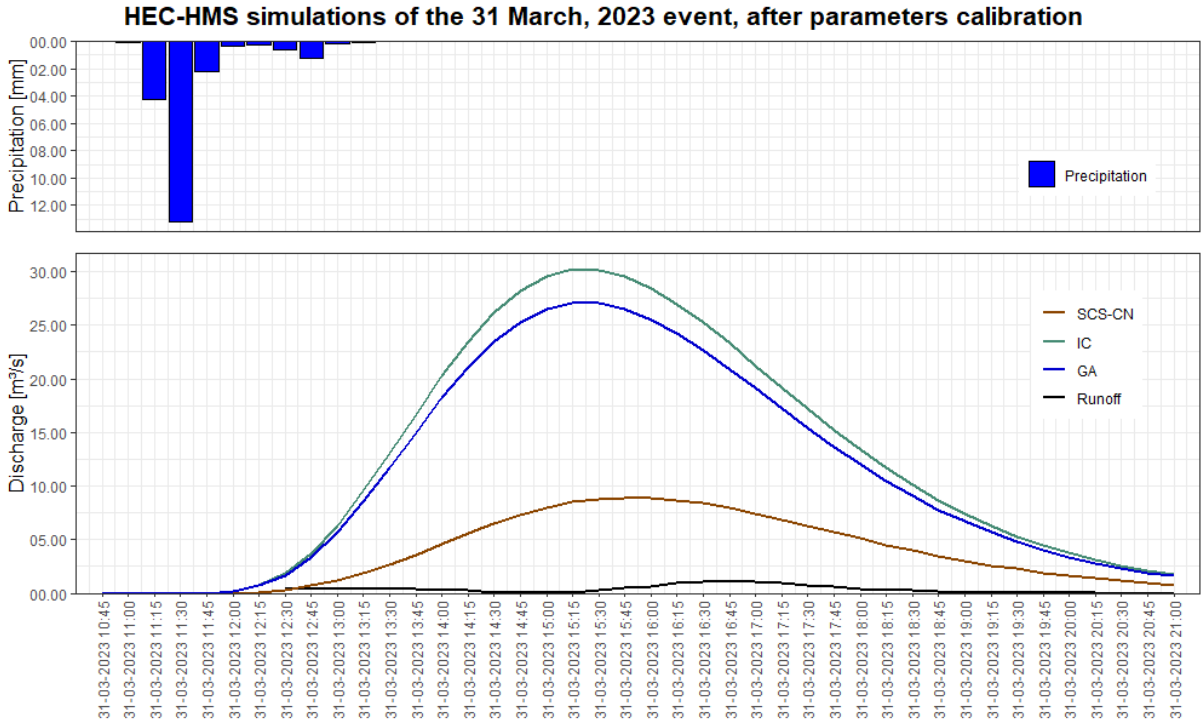

Appendix 40: HEC-HMS simulations of the April 02-03, 2023 event with the optimized parameters.

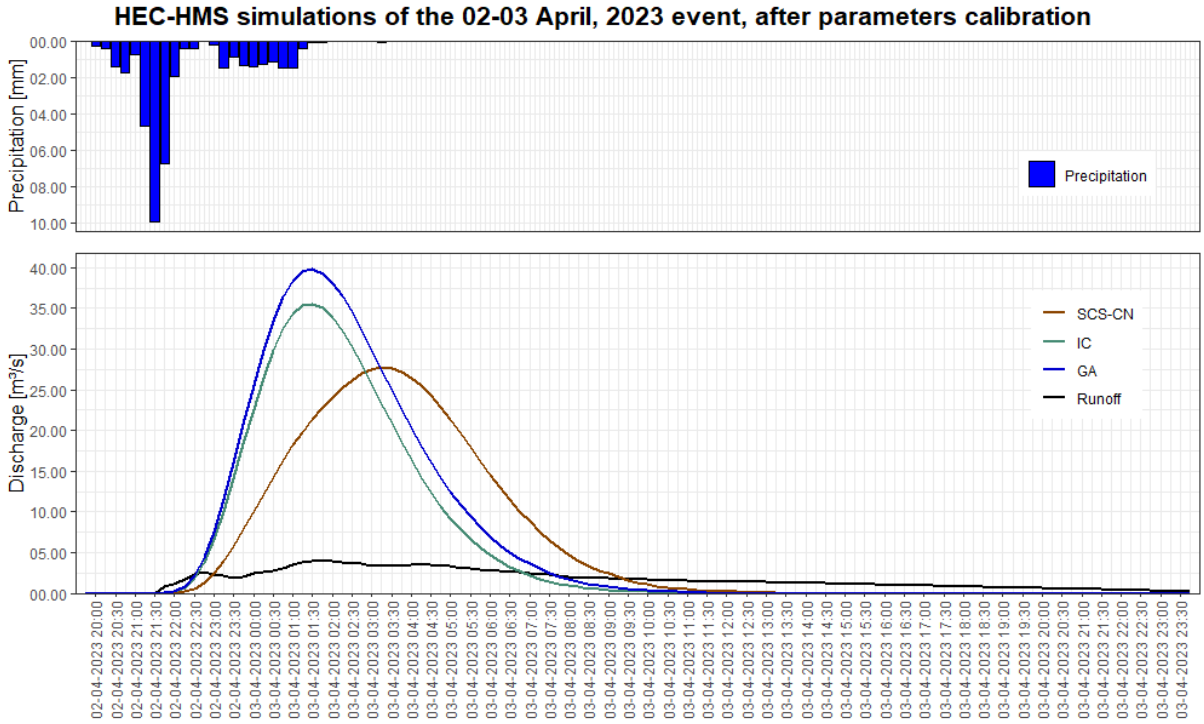

Appendix 41: HEC-HMS simulations of the April 15-16, 2023 event with the optimized parameters.

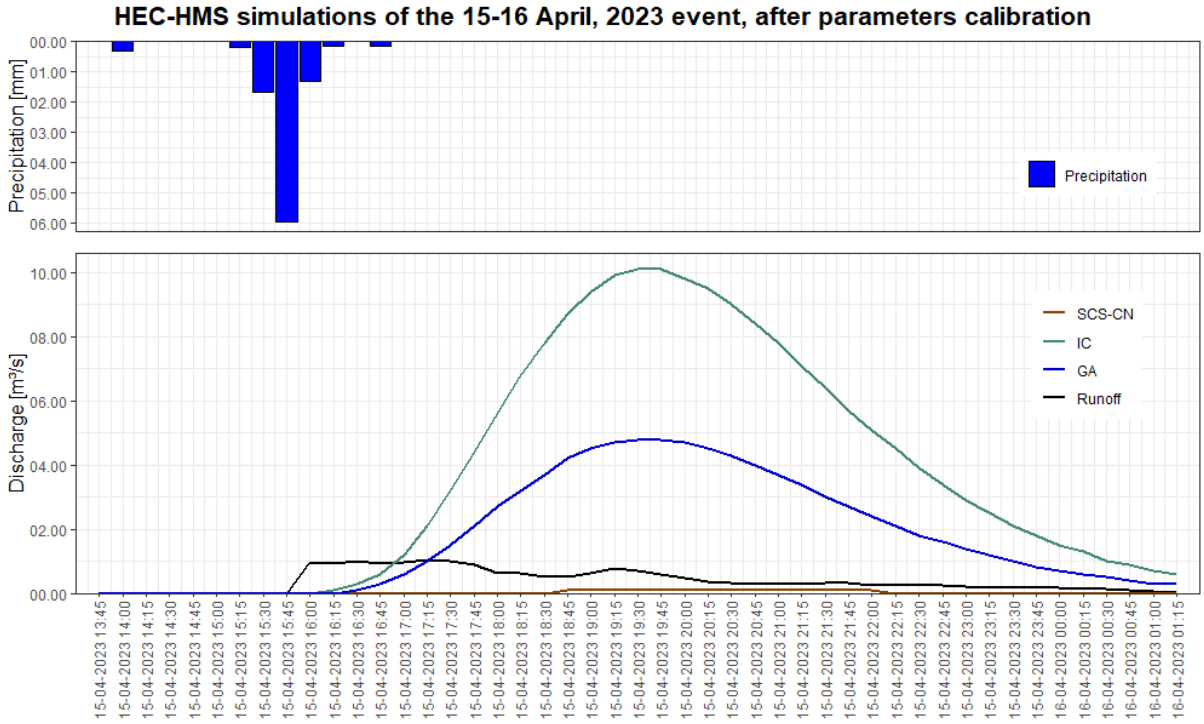

Appendix 42: HEC-HMS simulations of the April 16-17, 2023 event with the optimized parameters.

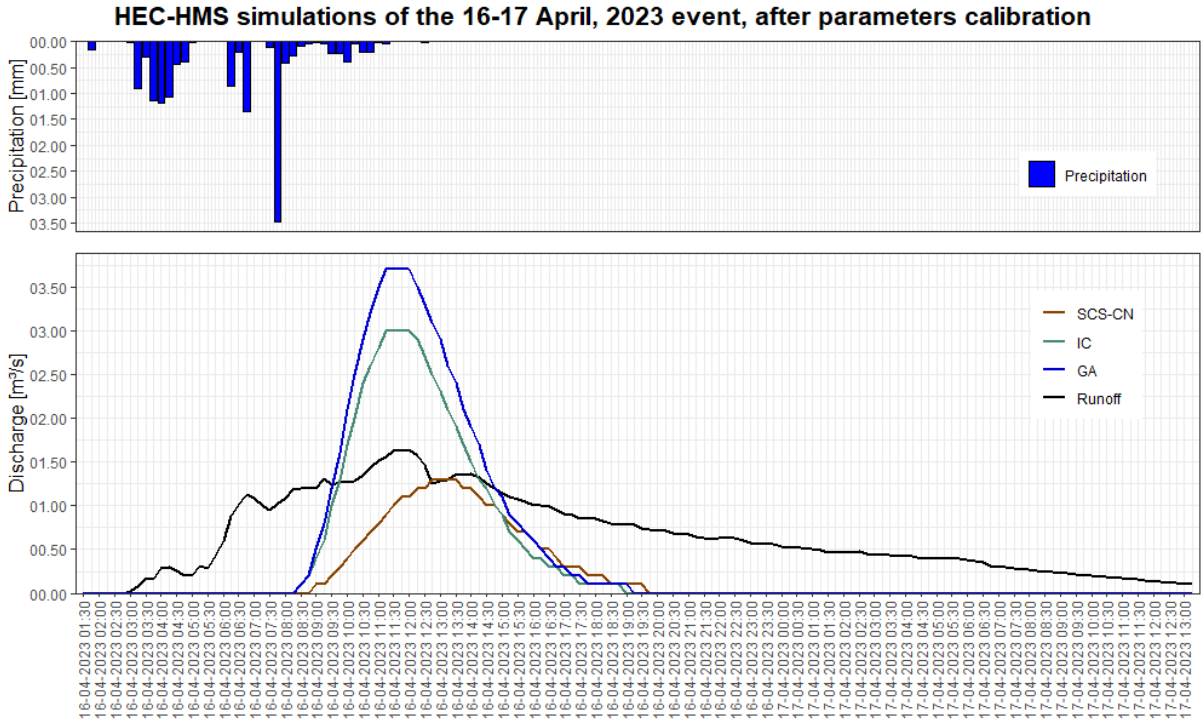

Appendix 43: HEC-HMS simulations of the April 18-20, 2023 event with the optimized parameters.

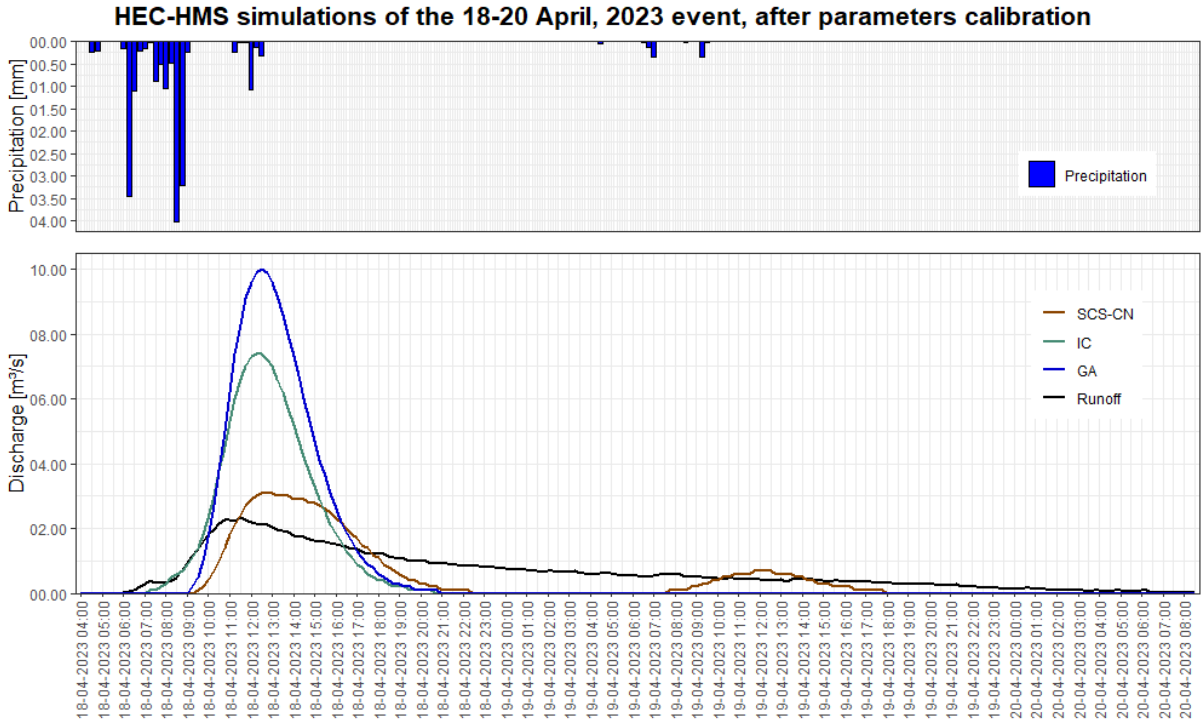

Appendix 44: HEC-HMS simulations of the April (1) 23-24, 2023 event with the optimized parameters.

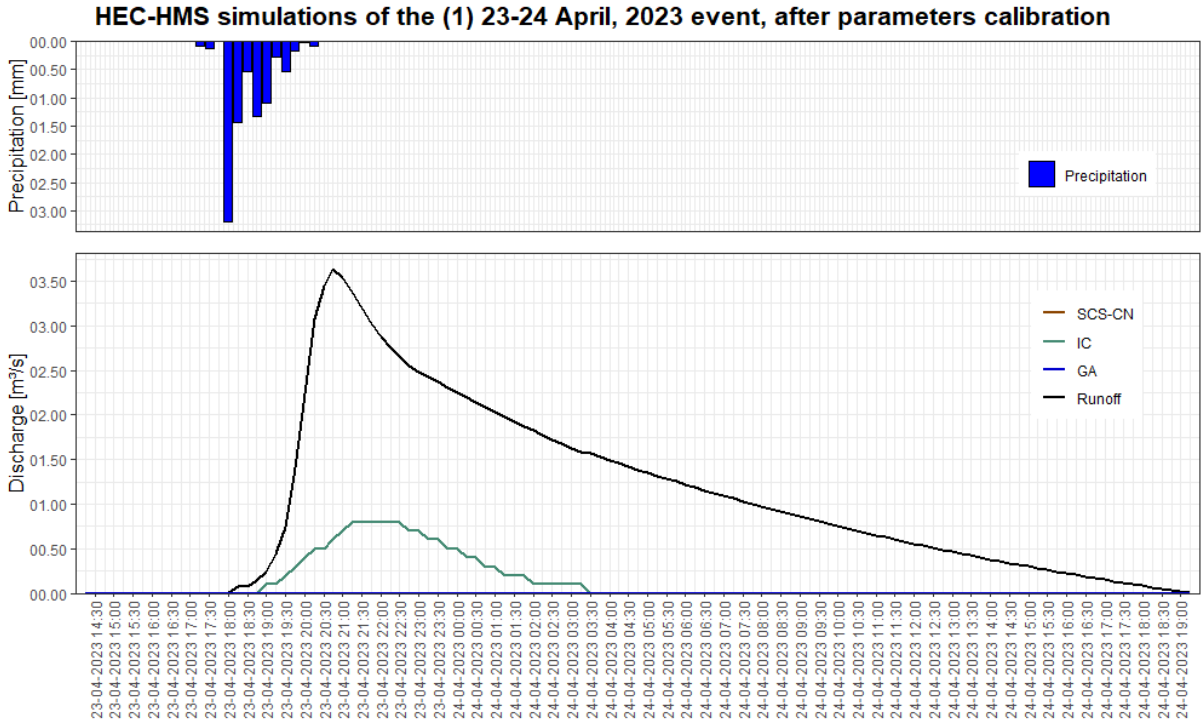

Appendix 45: HEC-HMS simulations of the April (2) 23-24, 2023 event with the optimized parameters.

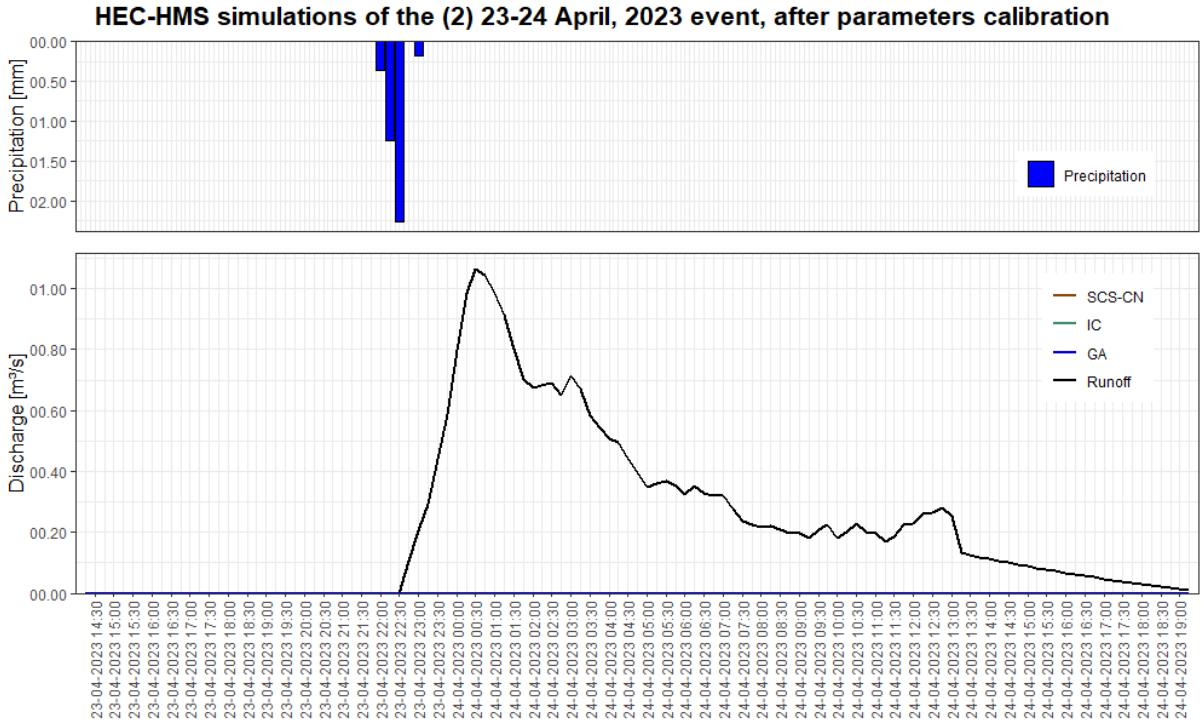

Appendix 46: HEC-HMS simulations of the April (1) 28-29, 2023 event with the optimized parameters.

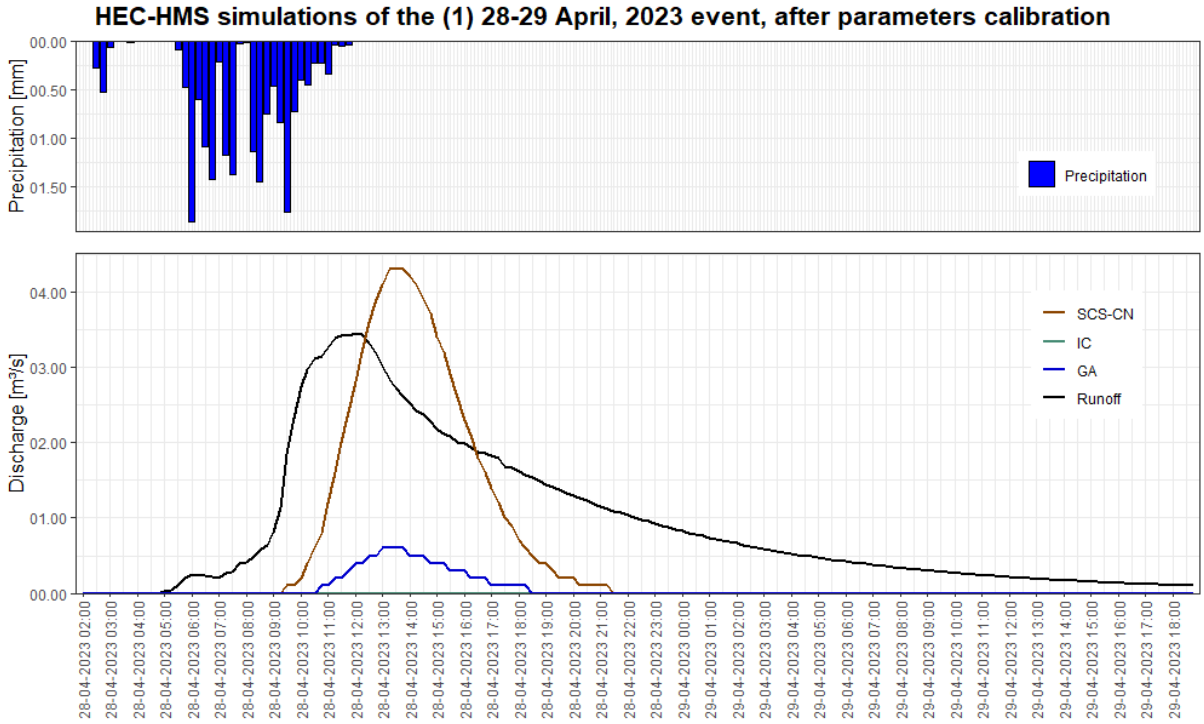

Appendix 47: HEC-HMS simulations of the April (2) 28-29, 2023 event with the optimized parameters.

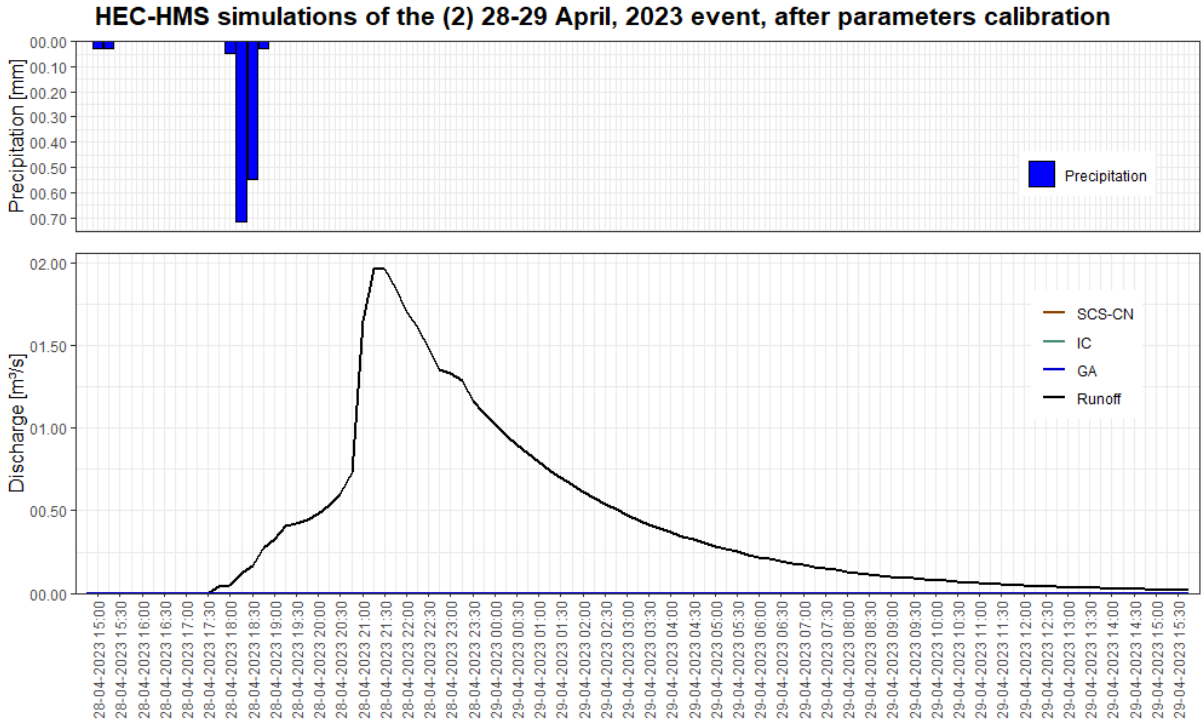

Appendix 48: HEC-HMS simulations of the April 29-30, 2023 event with the optimized parameters.

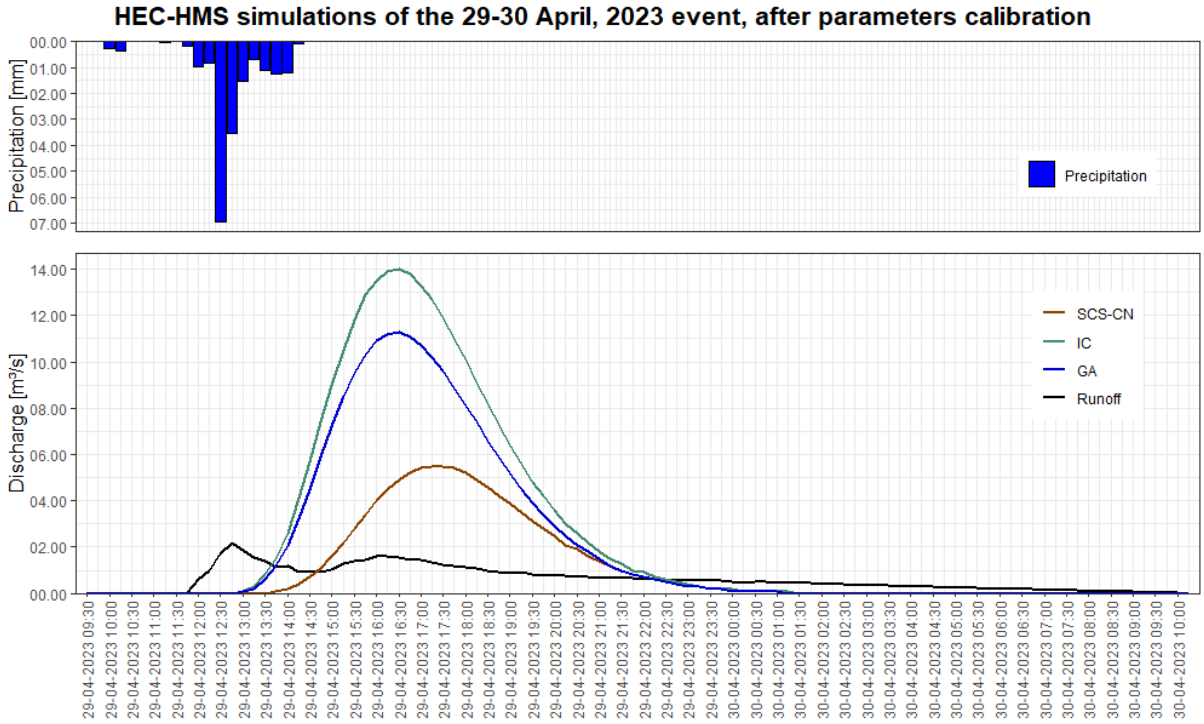

Appendix 49: HEC-HMS simulations of the April 30 – May 02, 2023 event with the optimized parameters.

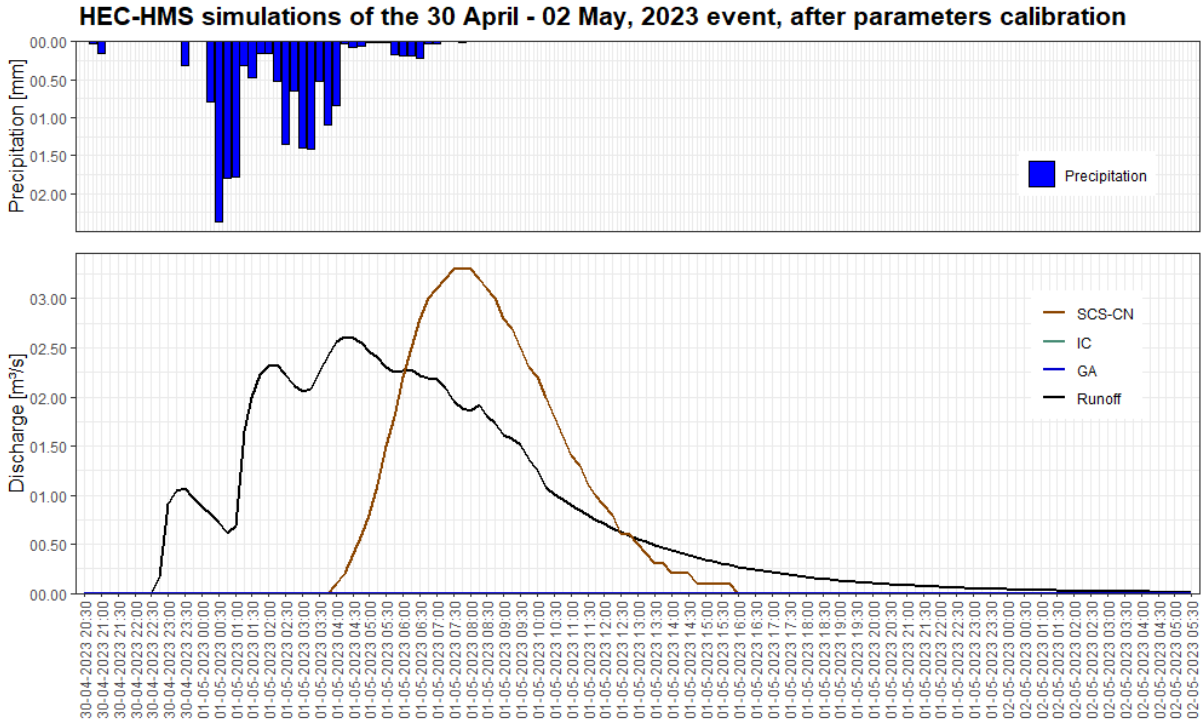

Appendix 50: HEC-HMS simulations of the May 01-03, 2023 event with the optimized parameters.

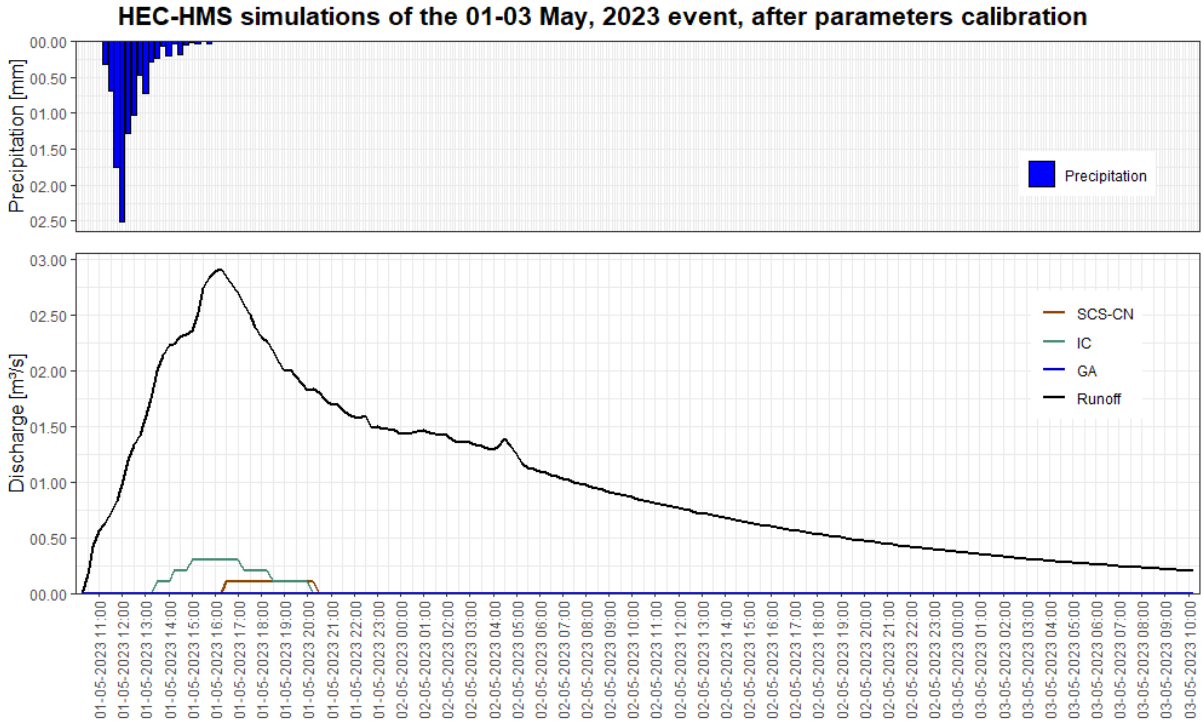

Appendix 51: HEC-HMS simulations of the May 02-03, 2023 event with the optimized parameters.

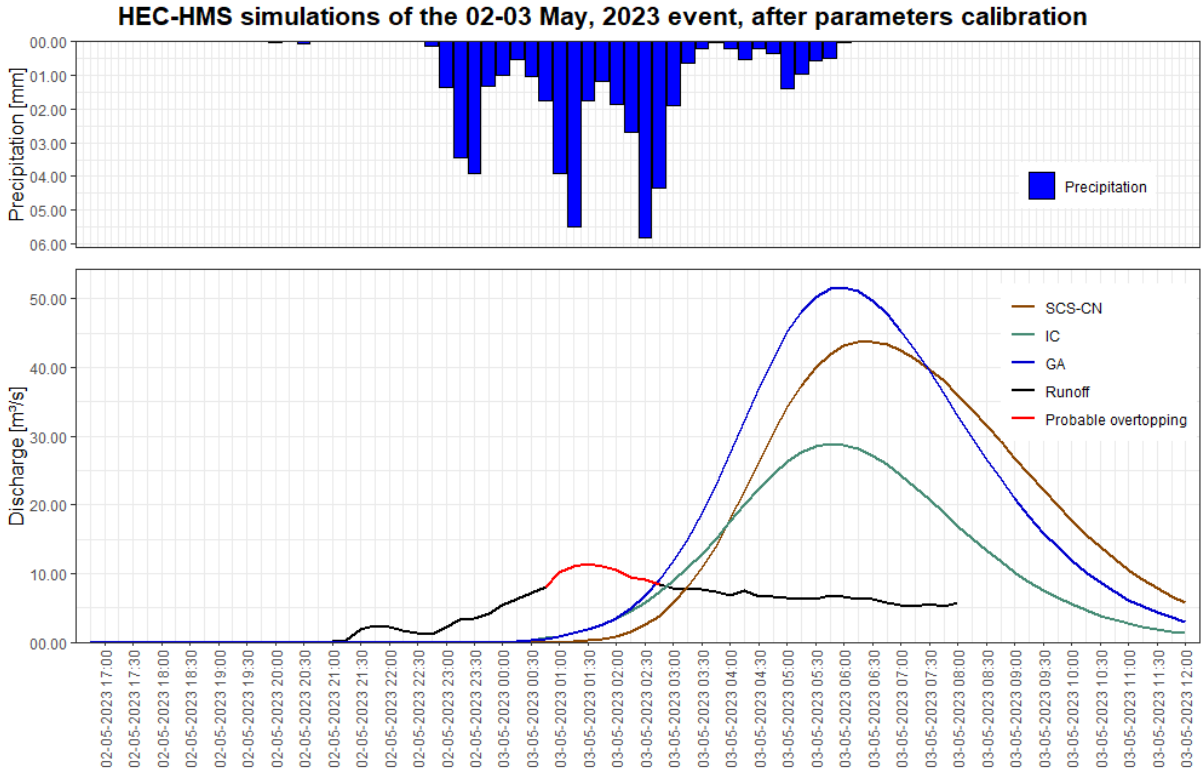

Appendix 52: Precipitation observations on March 31, 2023.

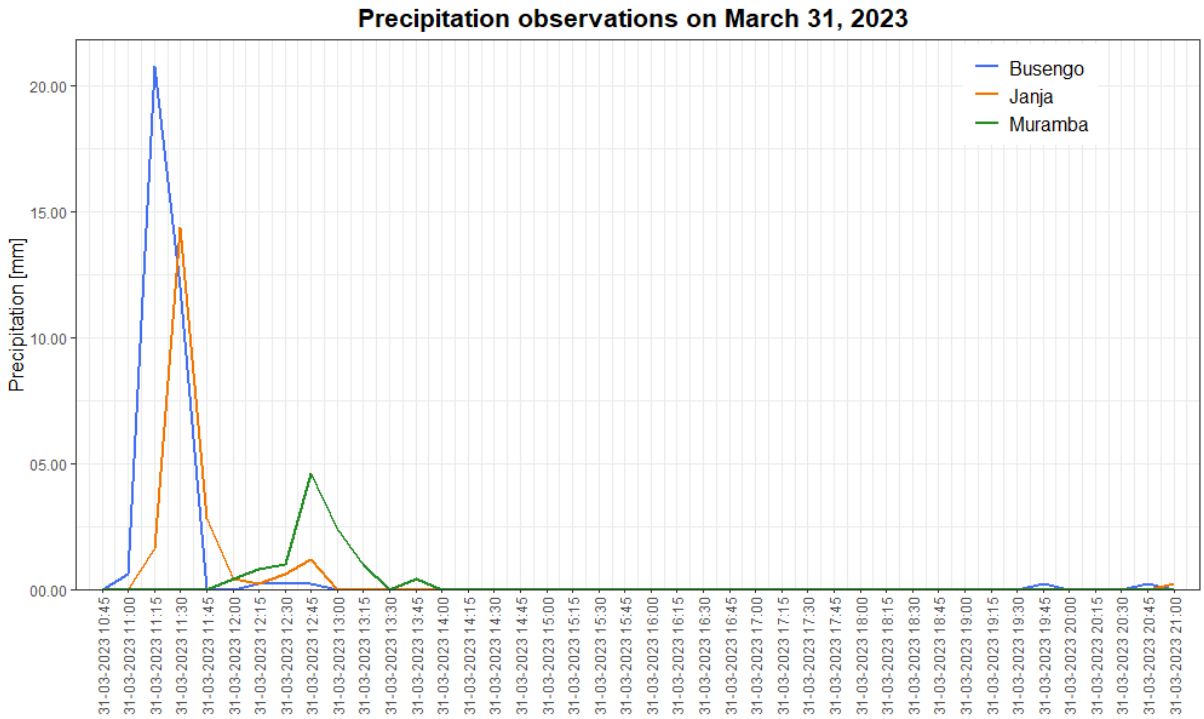

Appendix 53: Precipitation observations on April 15-16, 2023.

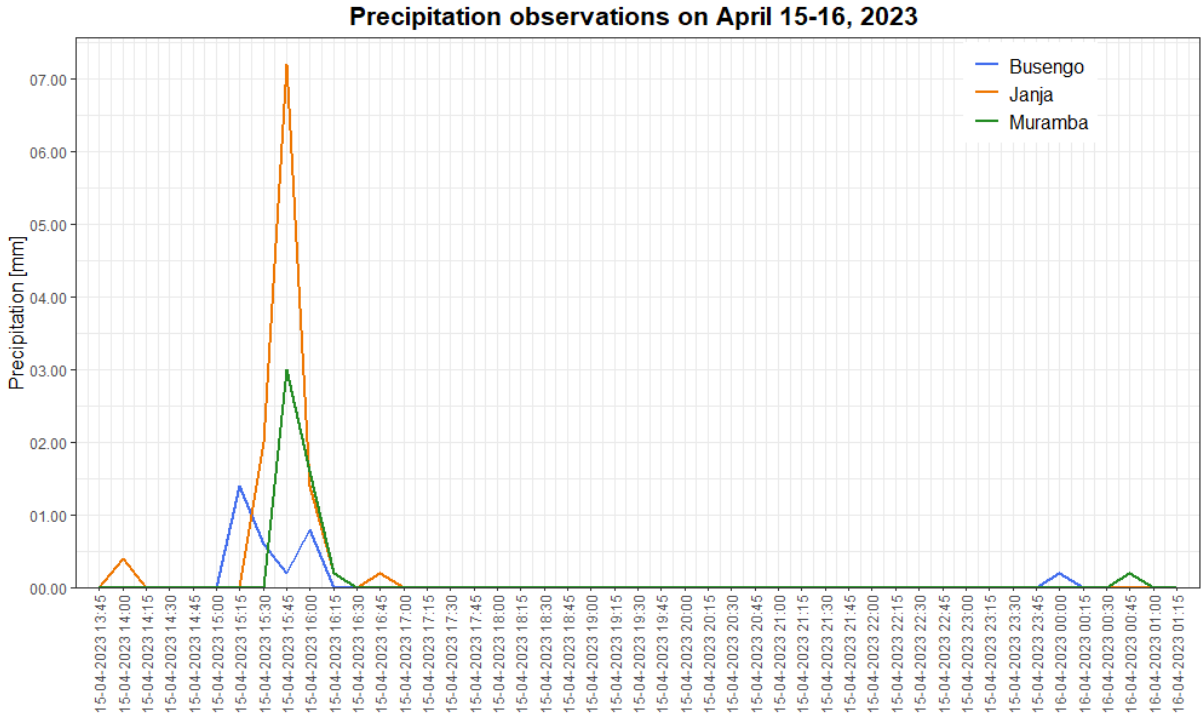

Appendix 54: Precipitation observations on April 16-17, 2023.

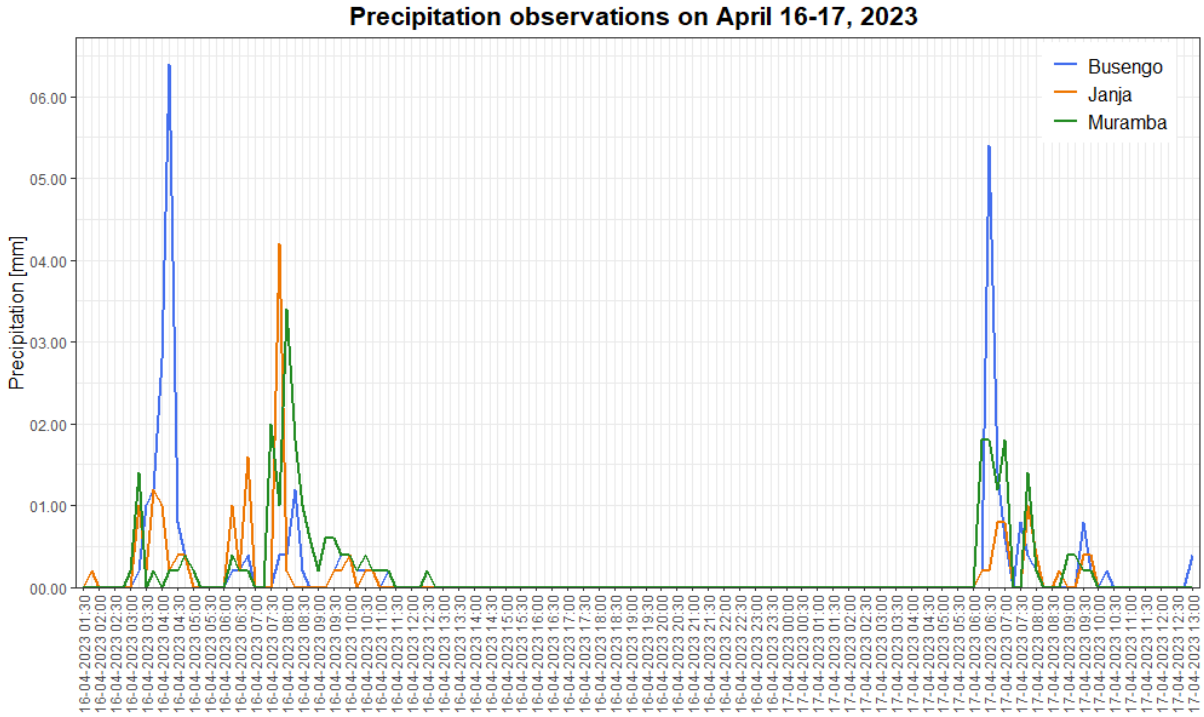

Appendix 55: Precipitation observations on April 18-19, 2023.

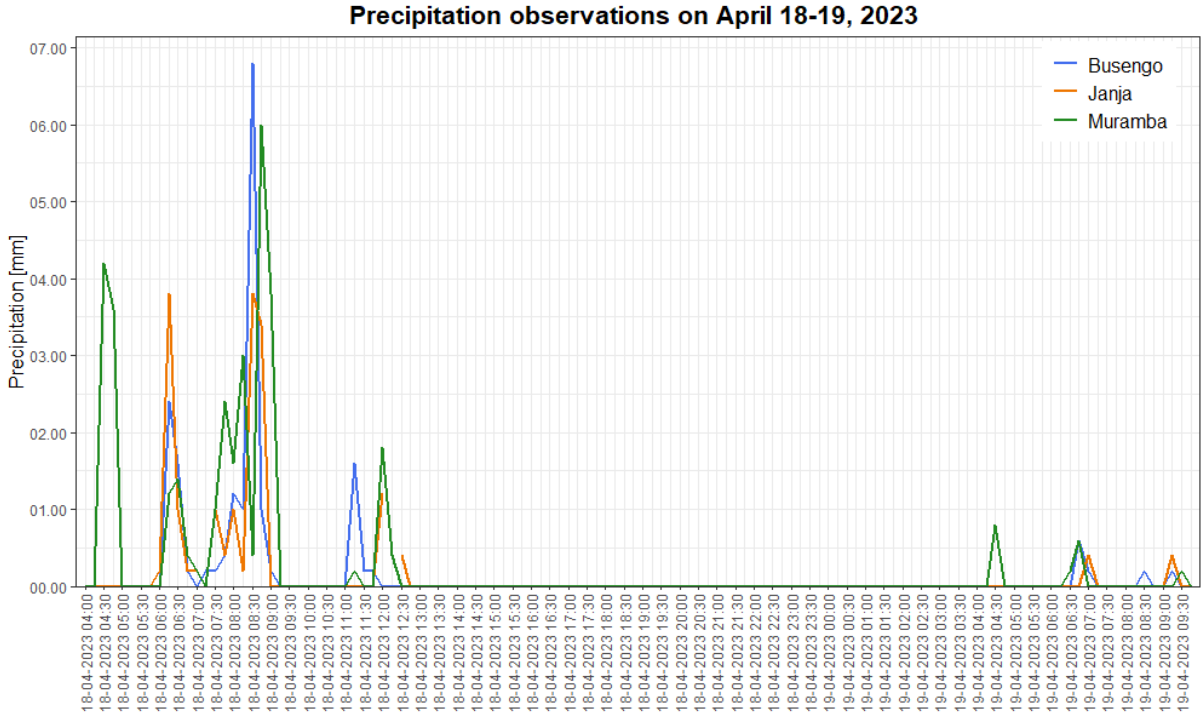

Appendix 56: Precipitation observations on May 01, 2023.

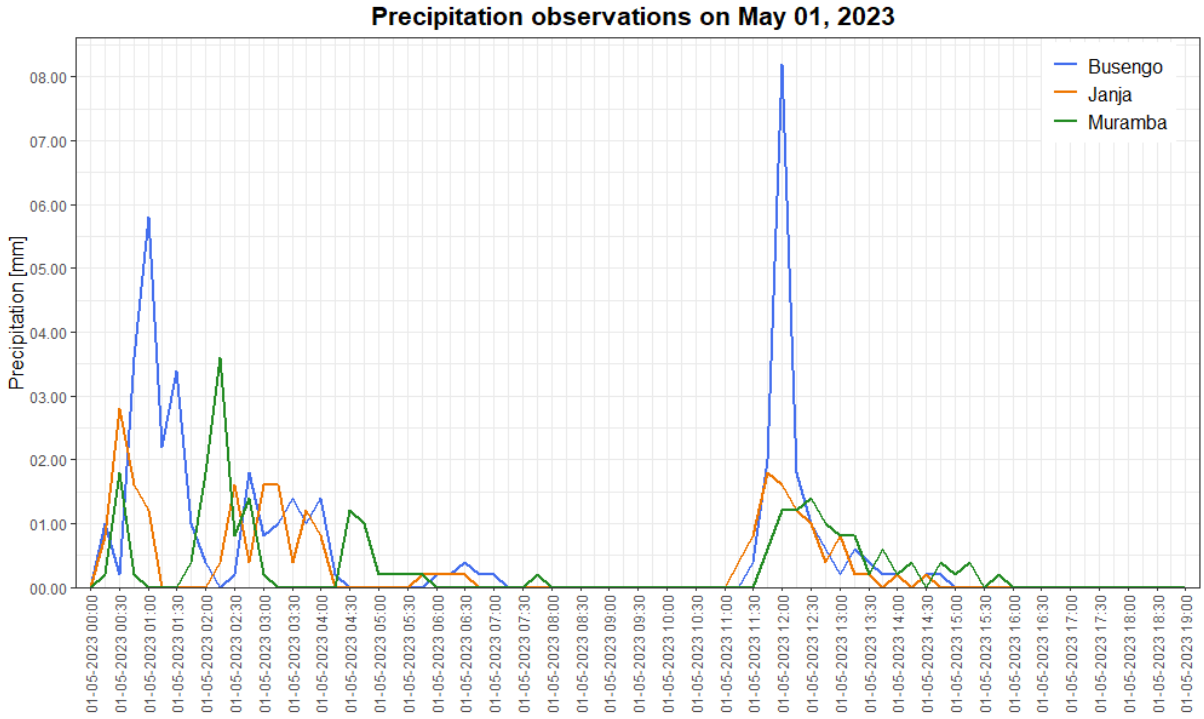

Appendix 57: Precipitation observations on May 02-03, 2023.